UNIVERSITÁ DI CATANIA

Corso di dottorato: Scienze dei Materiali e Nanotecnologie

Ciclo XXXIV

Andrea Maria Gerardo Valenti

"Surface self-assembly of functional architectures for nanotechnology applications"

Tesi di dottorato

Tutor:

Prof. Giovanni Marletta

Co-Tutor:

Prof. Antonino Licciardello

Coordinatore:

Prof. Giuseppe Compagnini

Anno Accademico 2020-2021

Index

1 INTRODUCTION 5

2 SURFACE ENGINEERING AND SELF-ASSEMBLING NANOTECHNOLOGIES 7

3 MOLECULAR ELECTRONICS. 15

4 POLYPYRIDINE-BASED METAL COMPLEXES 18

5 ELECTROCHEMILUMINESCENCE METHODS. 21

6 TOF-SIMS. 29

6.1 ToF-SIMS Imaging 33
6.2 ToF-SIMS 3D Imaging 34

7 FE-TERPYRIDINE-BASED SUPRAMOLECULAR ARCHITECTURES ON OXIDE SURFACES. 39

7.1 Materials ad methods 39
7.2 UV-Vis spectroscopy 42
7.3 ToF-SIMS characterization of Fe-DT and Fe-wDT -based molecular wires. 51
7.4 Discussion and conclusions 56

8 ASSEMBLY AND CHARACHTERIZATION OF MIXED FE (II) / RU (II) POLYTERPYRIDINE –BASED MOLECULAR WIRES. 58

8.1 Preparation of the molecular wires 58
8.2 Physico-chemical characterization of molecular wires 62
8.3 Conclusions 74
8.4 Physico-Chemical properties of molecular wires based on ruthenium and iron assembled on nanostructured gold surfaces 76
8.5 Conclusion 83

9 TOF-SIMS IMAGING AND UV-VIS CHARACTERIZATION OF NANO-ENGINEERED SURFACES 84

9.1 Spatially resolved functionalization of surfaces with metalorganic three-dimensional architectures 84
9.2 Patterning via UV-O_3 88
9.3 Assembly of the supramolecular wire 89
9.4 UV-Vis analysis 89
9.5 ToF-SIMS analysis 92
9.6 Profilometer analysis 102
9.7 Conclusions 104

10 PHOTOCONDUCTIVE PROPERTIES OF MOLECULAR WIRES BASED ON RU(II) AND FE(II) BISTERPYRIDINC COMPLEX STUDIED VIA PATTERNING APPROACH. 105

10.1 Characterization: ToF-SIMS imaging and profilometer 107
10.2 Conclusion. 111

10.3 PHOTOCURRENT MEASUREMENT 113
10.4 CONCLUSION 117

11 TOF-SIMS DEPTH PROFILING CHARACTERIZATION OF NANO-HYBRID SYSTEMS 118

11.1 TOF-SIMS DEPTH PROFILING OF SUPRAMOLECULAR STRUCTURE BASED ON TERPYRIDINE-IRON AND TERPYRIDINE-RUTHENIUM METALLORGANIC COMPLEXES. 118
11.2 CONCLUSIONS 128

12 TOF-SIMS DEPTH PROFILING OF NANOSTRUCTURED TIO2 FILMS FUNCTIONALIZED WITH RUTHENIUM METALLORGANIC COMPLEX FOR ECL APPLICATIONS. 129

12.1 FABRICATION OF PARTIALLY FUNCTIONALIZED MESOPOROUS TiO_2 ELECTRODES FOR ECL 129

13 ECL ELECTRODS PROTOTYPE MEASUREMENT TEST. 141

14 REFERENCES 144

1 INTRODUCTION

The continuous miniaturization and the increasing performances required to produce electronic devices is leading the scientific community to explore innovative solutions on nanometric scales. In this dimensional range, solutions based on organic or hybrid (organic-inorganic) systems show considerable interest. There are already several studies that testify the possibility to design, with geometric and functional control, nanometric supramolecular architectures able to exhibit different typologies of properties and / or to manifest / modify the latters under the influence of specific external perturbations of a physical or chemical nature[1] [2].

Many of these molecular or supramolecular systems require solvents to perform their specific functions: unfortunately, this represents a strong restriction for almost all the current applications based on solid-state technologies.[3] To overcome this issue, current research in this field focuses on developing methodologies able to integrate different functions that can be exercised at the molecular or supramolecular level on solid substrates. In this context, systems based on molecular structures anchored on surfaces - in a more or less ordered way - play an important role. Such systems are often realized via self-assembly methodologies.

An interesting application of molecular functionalities integration on solid substrates concerns molecular wires. Such systems consist in supra-molecular structures capable of conducting and/or photoconducting electrons and they can be realized by starting from specific "molecular bricks" (molecular bricks or molecular building blocks), with a stepwise procedure that allows a controlled assembly of the "wires" on the surface of different materials. In this case, the conductive and photoconductive properties induced on the surfaces are potentially indicated to molecular photodiodes. Thanks to the self-assembling strategy, such hybrid structures allow a control at molecular level able to overcome the current limits of the top-down approach in the realization of systems operating at nanometric scales[4].

To this aim, it is essential to tune the chemical properties on the surface of solids, since very often they do not allow an "easy" molecular engineering. One of the methods used to implement this tuning is the preliminary preparation of Self-Assembled Monolayers (SAMs), i.e. two-dimensional (monomolecular) films of molecules that self-assembly on a substrate in an ordered way. These ultra-thin layers allow to obtain surfaces with well-ordered structures, molecular composition, and thickness. The further functionalization of these SAMs can introduce specific macroscopic properties that can be exploited in devices design[5].

The present doctoral project, in its various tasks, has been developed through the following steps. Firstly, an identification step in which molecular systems with selected functional properties, to be implemented in surface engineering of different types of solid substrates, to design innovative solutions in the field of nanoscience and nanotechnologies were identified. Subsequentially a stage where suitable strategies for anchoring/assembling, depending on the specific properties of the selected building blocks and substrates were developed. A characterization step in which the systems were studied from a compositional, morphological, and structural point of view. The last logical step was the test of the assembled prototype.

The main goal of the PhD project, in accordance with the steps described above, was the study of surface anchoring methodologies, three-dimensional growth, photo conductive properties of wire-like supramolecular systems assembled using different preformed units of ruthenium-based and iron-based polyterpyridine building blocks.

In particular, all the steps have been investigated having as end point the development of strategies useful to monitor and to assemble an experimental set up to investigate the photoconduction properties of self-assembled molecular wire constituted by ruthenium- and iron- based bis terpyridine complexes. These systems are very interesting in view of applications to fabrication technologies that adopt nanometric films as stressed element in optoelectronic devices.

Due to these potential photochemical characteristics, during the development of the PhD project, a parallel study was conducted on the fabrication, functionalization with ruthenium-based metal organic complexes and characterization of nanostructured titanium oxide films for the development of electrodes for electrochemiluminescence (ECL).

The present manuscript, therefore, is organized as follows: in the first part an overview is given on the fundamental issues involved in the development of the doctoral project. Since, throughout the all-experimental work time-of-flight mass spectrometry (ToF-SIMS) has been widely used for the characterization of the engineered structures, the final section of the first part gives an overview, although partial, of some key features of this key technique. The second part of the thesis reports and discusses the experimental results obtained. In particular, it is subdivided according with the different aspects that involved, respectively, the assessment of the assembly performance of different building blocks on solid substrates, the two-dimensional characterization of patterned surfaces and, finally the preparation and characterizations of nanostructured three-dimensional structures for ECL assay application.

2 Surface engineering and self-assembling nanotechnologies

Nowadays scientific research on nanoscience, relying on theoretical rationalization and on the acquisition of experimental skills in nanoscale manipulation, is able to deliver benefits in various fields of technology[6] [7]. Indeed, the products of such scientific advancement turned out to be powerful tools for multidisciplinary fruition, as they involve aspects that can be spent in various scientific contexts, ranging from molecular biology to medicine, to chemistry of materials[8] [9] [10].

In this context, the bottom-up approach in surface engineering, based on the concepts of supramolecular chemistry, has showed how it is possible to design methodologies to assembly nanometric supramolecular architectures that can be integrated into devices of technological interest[11].

To this end, the most exploited phenomenon is the surface adsorption. This is classified into two categories, based on the type of interaction that is established between the [supra]molecular system and the surface. We refer to physical adsorption or physisorption when any changes are measured in the electronic structure of the molecular adsorbed system, on the other hand we refer to chemical adsorption or chemisorption when the electronic structure is "altered" due to the strong electronic interactions established between the surface and the molecular system. The latter typology guarantees a stable and homogeneous functionalization because, if the appropriate molecular compounds are used, they will make use of the "strongest" interactions (e.g. covalent bond) to bind to the surface and, once anchored to the solid surface, they will exploit the weaker ones (intermolecular forces) to organize themselves further in the space. Furthermore, the existence of such weak intermolecular interactions, thermodynamically reversible, allows the organic supramolecular structure to be able to "self-correct" [12] .

This bottom-up functionalization strategy, which simultaneously relies on interactions of covalent nature (irreversible) and interactions of non-covalent nature (reversible), is widely used to functionalize a surface by exploiting the two-dimensional ordered self-assembly of the employed molecular systems, known as self-assembled-monolayers (SAM). Surface functionalization by SAMs turned out to be an interesting and highly successful technique because it exploits extremely simple experimental methodologies and it allows the realization of thermodynamically stable systems.

This hybrid functionalization (covalent-non-covalent) methods exploited in the formation of self-assembled monolayers can be used also, with appropriate

adjustments, for the controlled formation of three-dimensional architectures, for example usable to produce system for molecular electronics.

The experimental methodology to produced SAMs simply requires the immersion of the solid substrate of interest in a solution of millimolar concentrations of the molecular bricks, as schematized in Figure1.

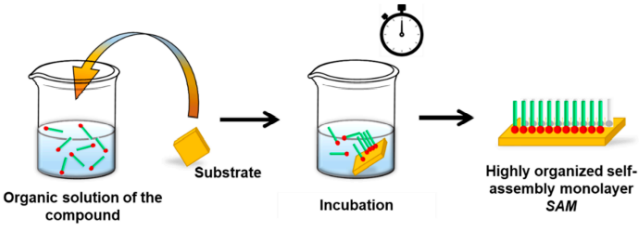

Figure 1 *Schematic of the self-assembly process of specific organic compounds also called surface agents or building blocks. The substrate is first immersed in a solution where the surface agents are solubilized. Following the incubation period and removal by washing with pure solvent, the surface is then functionalized.*

Such molecular bricks or building blocks, also called surface active agents, typically are consisting of i) a functional group called head group, suitable to bind at the surface ii) a body often referred as "the spacer and iii) a tail group separated from the head group by the spacer. The covalent interaction with the surface and the collective intermolecular interactions of the anchored molecules can lead to formation of a compact and two-dimensional ordered molecular monolayer. The possibility of achieve ordered SAMs with high surface density depends both on the chemical functionality expressed by the head group, responsible for its interaction with the surface, and on the ability of the surface-adsorbed molecules to establish weak and periodic interactions with the other molecules[13]. These interactions are those involved between spacers i.e. the portion of the surface agents that link the head group to the terminal group. The latter is the portion of the molecule that exposes to ambience the functional groups responsible of different physics-chemical properties of the new surface, such as wettability[14], reactivity[15], the optical or electrical properties[15 16]. The presence of a reactive tail group can give the ability to bond with further molecules, paving the way for a variety of possible functional molecular architectures usable in a wide range of applications, such as smart surface for sensing, self-cleaning surface, or molecular heterojunction preparations.

In the field of self-assembled monolayers systems, historically, the more studied ones are those that exploit the high chemical affinity between sulfur and a noble metal (mainly gold, but also silver, copper, palladium). In fact, for anchoring on these substrates a molecular system, le latter is usually equipped with a thiol functionality acting as head group [17] [18] [19]. The classic case are SAMs of linear alkan-1-thiols on gold surface with chain length typically ranging from 8 to 20 carbon atoms.

However, the use of thiols, while offering excellent performance in terms of uniformity and order of the monomolecular coverage of gold substrates, suffers several limitations, including the non-general applicability to substrates other than noble metals, and also a certain instability at temperatures slightly above ambient temperature or in the presence of aggressive chemical environments[17].

In reference to above mentioned thermal stability limitations, Delamarche et al reported on the effect of annealing of dodecanethiol SAMs. Indeed, during the annealing process vacancy islands in alkanethiol SAMs are typically observed or domain boundaries are formed. If the annealing process is continued, thiol molecules start to desorb from the Au surface. It seems that a good compromise between SAM reorganization and disruption is at about 373 K, because the speed of reorganization of the SAM is faster than desorption and chemical reaction of the sulfur headgroups [20]. This temperature-triggered behavior indicates that there is an energy barrier for disulfide formation which has been assigned to the formation of gauche defects at the S–C bonds. The key factor involved in the thermal stability of thiol-Au SAMs is attributable to the van der Waals mutual interactions which mainly determine the energy of desorption.[21]

Although thiol SAMs on gold have been and continue to be of great interest in the field of materials science, both purely theoretical and applicative, the limitations have prompted researchers to explore new combinations of surface agents - substrate. Consequently, many studies have been directed to search for surfactant molecules with head groups suitable for anchoring on different types of surfaces.

As an example, 1-alkenes and 1-alkynes have been used for the formation of SAMs on silicon, due to their capability to bind to H-terminated silicon surfaces through the formation of a Si-C bond[22,23]. Sudholter et al showed that well-ordered monolayers of 1-alkenes on hydrogen-terminated silicon surfaces can be prepared from dilute solutions of the 1-alkene in various aromatic solvents. They underlined that crucial parameterr to obtain well-ordered monolayers are both the choice of solvent nature and concentration.[24] It is also possible to obtain highly stable organic monolayers on silicon surfaces by irradiating a hydrogen-terminated silicon

substrate with visible light at room temperature in the presence of a 1-alkenes or 1-alkynes.[25]

Oxides are another interesting class of substrate materials on top of which it is desirable to anchor organic structures. They are generally indicated as MOx, where M can be a metal (e.g. Fe, Al, Cr), a semiconductor (e.g. Si), or even a material that has an oxygen-free bulk but forms surface bound hydroxy (-OH) groups exposed to air or after activation reactions (e.g. SiC or CrN). A wide spectrum of properties can be individuated in this class of material, such as: chemical stability, conductivity, mechanical stability, visible light transparency. On many of them, the presence OH-groups at surface represent the reactive key feature to obtain densely packed monolayers via different experimental method and several class of molecular compounds. Among these, the most common are: silanes which probably are the compounds with highest reproducibility and rapidity to form silane SAMs [26], carboxylate compounds which are widely used in DSSC electrode surface functionalization despite their highly instability in aqueous media [27] [28], catechol, that can be used to obtain biomimetic surfaces [29] , alkene/alkyne based SAMs that can resist to 4 h of heating in 2M HCl solution at 90°C, and phosphonic acid compounds where the presence of three oxygen atoms allows mono-, bi-, and tri-dentate binding modes in combination with possible electrostatic and hydrogen-bonding interactions with oxide's hydroxylic groups [30] [31] . Moreover, several chemical activation procedures of oxides surfaces exploit the chemical affinity of phosphates/phosphonates or carboxylic acids with to some transition metal ions, and in particular Zr^{IV} .

To improve monolayer stability of carboxylic acid, Bernasek and co-workers developed a method for SAMs preparation on native oxides of metals. As sketched in Figure 2 Two steps are involved in this procedure: i) tetra-tert-butoxyzirconium ($(t\text{-}BuO)_4Zr$) reacts with a hydroxylated metal oxide surface leading to a strong binding of Zr; still holding two equivalents of t-BuOH, ii) in the second step the surface is exposed to carboxylic acids that are able to replace the remaining two alcohol moieties[32].

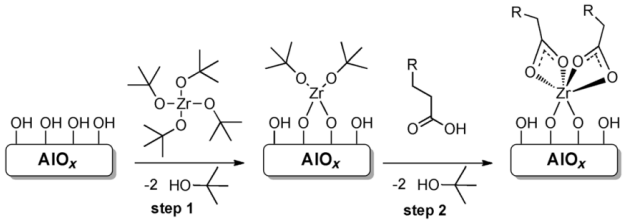

Figure 2 Highly improved binding of n-octanoic acid to zirconium alkoxide- treated hydroxylated Al surfaces by formation of a zirconium η^2 -carboxylate.

Mallouk et all were the pioneers in investigating the role of Zr^{IV} in binding processes of phosphonic acids on solid surfaces. They report the synthesis of multilayers via multistep formation of zirconium 1,10-decanebisphosphonate $Zr(O_3PC_{10}H_{20}PO_3)$ ("ZDBP"). The formation of the ZDBP multilayer is achieved after the initial formation of a monolayer by means of a phosphonate-terminated molecule bringing a silanol head group, followed by a second step where the surface is exposed to an aqueous $ZrOCl_2$ and, after proper rinsing procedure, a third step of exposure to aqueous solution of 1,10-decanebisphosphonic acid[33]; steps 2-3 can be iterated in order to obtain the multilayer of ZDBP (see Figure 3).

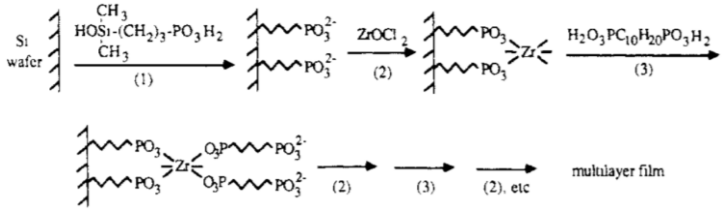

Figure 3 Schematic representation of formation steps of the ZDBP multilayer procedure

Studying the coordination chemistry, the resistance to chemical attack and the directionality of multilayer layers connected through coordination to Zr^{4+}, Bakiamoh and Blanchard proposed an experimental strategy to bind 10hydroxydecanoic acid (HDA) or 3hydroxy1propanesulfonic acid (PSA) on silicon substrates exploiting a phosphorylation reaction and a Zr^{4+} coordination reaction (Figure 4). Precisely, Si(100) surface is exposed at $POCl_3$/2,4,6collidine in anhydrous acetonitrile solution under argon and subsequently at solution of $ZrOCl_2$ in 60% EtOH(aq). Compared to

the previously mentioned ones, the advantage of this reported surface priming procedure is the capability to lead to the formation of a very stable thin film Si –O-P-$(O)_3$-Zr^{4+}-$(OH)_2$ directly on surface without any other involved molecular system.[34]

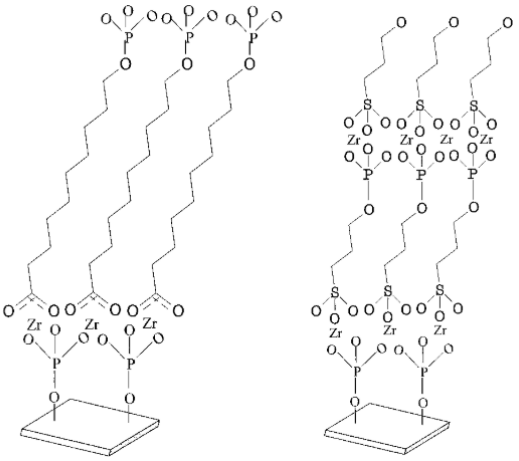

Figure 4 (Left) An oriented multilayer formed using HDA and reacted with $POCl_3$/collidine and then H_2O. (Right) An oriented multilayer formed using PSA and reacted with $POCl_3$/collidine and then H_2O. These schematics are not intended to indicate the precise stoichiometry of the layered interfaces

A huge experimental simplification to this oxide's priming approach was developed by studies conducted by Morotti et al[35] and by Spampinato [36]et al, that by tuning exposition time of several oxides (surface SiO_2, quartz, ITO and FTO) at pure $POCl_3$ for the phosphorylation and of the subsequent treatment with $ZrOCl_2$ aqueous solution were able to bind a phosphonic acid- terpyridine ligand e 4(2,2':6',2''terpyridine4yl)benzenephosphonic acid (PPTP) to the zirconium phosphate monolayer formed on top of a variety of oxide substrates.

Alkylphosphonic acids, thanks to the ability and rapidity to generate highly ordered monolayers onto different oxide surfaces, are also employed in designing patterned functional surfaces by using several techniques[37] [38]. Among them, electron beam lithography approach was proven to give good results like, for example, those reported by Alexander who, by using a e-beam lithography approach on a monolayer of ODPA (octadecylphosphonic acids) assembled on aluminum substrate, demonstrated the possibility of obtaining features with about 40 nm lateral resolution[39].

It is well known that laterally resolved features can be obtained also by means of photopatterning techniques. Self-assembled monolayers of alkylphosphonic acids on oxide substrates can be patterned by exposing the functionalized substrate at light with a wavelength 250 nm through a mask or by laser writing, producing a photodegradation of the SAM in the irradiated areas. In this patterning procedure the nature of the substrate as well as the chain length of the surface agent play a key role. By comparing photoinduced degradation rate of the same surface agents (ODPA) on different metal substrates it turns out that is faster when the SAMs is assembled on titanium oxide surface than on aluminum oxide surface. This effect is typically attributed to the photocatalytic properties of titanium oxide surface. It is also demonstrated that as the chain length of the alkylphosphonic acids increases, the increasing dispersion force arising from interactions between multiple CH_2 portions promote the adoption of an ordered configuration that leads to low chain mobility. Thus, adsorbates with short alkyl chains form liquid-like structures, longer adsorbates form highly ordered crystalline structures. This enhancement of dispersion forces between longer adsorbates hampers the progress of oxygen-containing molecules to the oxide surface and slows-down the rate of oxidation[40 41].

The photo-patterning procedure allows to modify not only the properties of the molecular assembled compounds but also the characteristic of the oxide surface, indeed if the exposition at UV light of alkyl phosphonic titanium oxide substrate is followed by chemical etching, an inversion of the expected contrast is observed: the phosphonic acid monolayer behaves as a negative tone resist rather than a positive tone resist[40].

The mix of substrate surface properties, photochemical characteristic of SAM and light source, as well as post etching steps allow to design experimental procedure sequences capable to produce many different patterned functionalized oxide surfaces.

The studies reported by Killian et al represent a smart example of managing the photochemical properties of different oxide surfaces and surface agents to obtain patterned structures. As schematically represented in Figure5, substrate composed by patterned portions of zirconium oxide and titanium oxide were first functionalized with a phosphonic acid SAM (OPA), which can bind with both of oxides surfaces. In the successive step the pattern is exposed to UV light in aqueous environment where the decomposition of the OPA SAM is triggered by the hydroxyl radicals formation by the photoactivity locally promoted onto titanium oxide surface portions, on the other hand the OPA SAM assembled on zirconium oxide portion remain intact. The partial photodegradation of OPA monolayer removes the alkyl portion of OPA monolayer leaving the phosphate group onto TiO_2 areas. This, upon

treatment with a $ZrOCl_2$ solution, coordinates zirconium ions obtaining a spatially resolved chemical platform that can be used to bind, e.g., a siloxane but also all surface agents with complementary affinity with -PO_4H-ZrO [42].

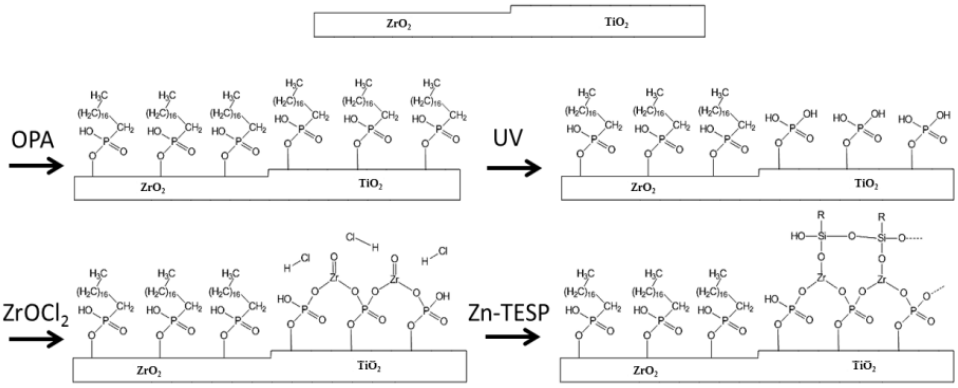

Figure 5 Schematic representation of photochemical approach to obtain patterned surfaces, based on spatially resolved different properties of surface oxides.

An example of patterned binding of functional metalorganic complexes on primed oxide surfaces is reported by S.Vitale et al[43]. In this study the surface of FTO (fluorine-doped thin oxide) was modified by a stepwise priming procedure leading to the formation of zirconium-phosphate monolayer (ZP), patterned by meand of a focused ion beam (FIB) approach. In this case it was demonstrated that the strong interaction between Zr(IV) and terpyridinic moieties of Ru(II)-bis[4',4''''-(1,4-phenylene) bis(2,2':6' ,2''-terpyridine) ($RuDT_2$) lead a formation of a SAM preferentially in the portion of FTO surface where the FIB leaves unaltered the ZP monolayer. Complementarily, successful adsorption of phosphonic derivative of rhodamine B (4-(2,2':6'-2''-tepryridine-4-yl) benzenephosphonic acid) is observed in the portion of substrate where the FIB exposure has removed the zirconium-phosphate monolayer.

3 Molecular electronics

The origin of molecular electronics is historically attributed to Aviram and Ratner that, in the paper ‘‘Molecular Rectifiers’’ published in 1974[44], reported about a model where a single molecule could exhibit preferential electronic conduction in one direction along its molecular axis. From this theoretical intuition it was possible to experimentally investigate fields of materials sciences in which single or more molecules perform functions in electronic technologies. One of the first goals that the scientific community set itself was to understand the behavior of molecular components of different nature in electronic circuits and any integration possibility of these in conventional microelectronic technologies based on semiconductors[45]. Today the biggest goals in molecular electronic research field are still summarized briefly by: ‘‘Make a robust molecular junction with reproducible electronic behavior; determine the relationship between molecular structure and current–voltage characteristics; exploit new functions enabled by molecular components by integrating with commercially viable microelectronics [45]. To fully understand these scientific and technological goals, it is important to describe what a molecular junction precisely is. We can define the molecular junctions as system that incorporate one or more molecules in electrical contact with two conductors, such that electrons are moved through the molecule(s).

The conductors to which the molecules involved are bound are called “contacts”. They are characterized by a distribution of electronic energy levels and associated densities of electronic states (DOS).

When an appropriated voltage is applied across the junction a rearrangement of electrons take place in the contacts and the negative electrode having a larger fraction of filled orbitals.

If the equilibration of the energy levels induced by the application of voltage generates a large energy gap, the molecule and conductor are isolated and do not interact electronically. On the other hand, an “ohmic contact” is reported when the electrons may move freely between molecule and conductor and means that a good electronic coupling between the molecule and contact is generated[46].

Many electrons transfer (ET) mechanisms have been theorized, these often depend on molecular size and structure, temperature, and the entity of the free energy gap between donor and acceptor. The coherent tunneling model, based on a quantum mechanics approach, is based on the probability of an electron to move through a barrier of some thickness and height, maintaining the phase of the electron[47].(figure 6)

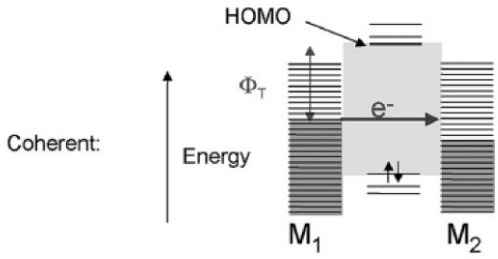

Figure 6 Energy level diagrams for coherent tunneling. Φ_T is the barrier for coherent tunneling, M_1 and M_2 are the metallic contacts.

The rate of coherent tunneling decreases exponentially with the thickness of the barrier and is described by the Simmons relation that, in a simplified form can be written as:

(Equation 1)

$$J = Be^{-\beta d}$$

where J represent the current density, B is a constant, β has units of inverse nanometers and d is the distance between conductors. The beta value is crucial in understanding the phenomena underlying the conduction mechanism. In the case of metal electrodes separated by vacuum and characterized by a work function equal to 5 eV, the Simmons model gives rise to a beta value of 2.3 $Å^{-1}$; in the case of molecular junctions, the experimental value obtained for beta value is usually close to 1 $Å^{-1}$ [48]. In the latter case the energy gap obtainable from the Simmons model would be approximately equal to 0.96 eV which would describe a HOMO-LUMO gap much lower than that of a typical molecular junction (5-10 eV). The explanation that is suggested refers to the phenomenon called "superexchange" which indicates that the interaction between the occupied and non-occupied orbitals of the molecular systems with electrons is responsible for this boost in tunneling rate[49]. In summary, the electronic transmission through tunneling mediated by the interaction with the orbitals of specific molecular systems interposed between the electrodes is more efficient than when there is only space between the electrodes. Coherent tunneling is a conduction mechanism that is not activated directly by temperature, it depends exclusively on the size of the molecular system interposed between the contacts and is never recorded for systems longer than 25 Ångstroms. Another model has been proposed, called incoherent tunneling, where the transmission of the electron occurs over distances around 40 Ångstroms and along this random walk path the phase of the electron can be modified.[50]

When we have molecular systems conducting longer than a few nanometers the conduction process via tunneling cannot take place and the mechanism that in this case best describes the charge conduction is the hopping mechanisms [51]. In case of ET phenomena due to tunneling, a finite probability of finding the electron on the other side of the barrier without requiring nuclear motion is possible, unlike in case of hopping mechanism, where the molecule must rearrange for ET to occur. The rearrangement of the molecular system could be rationalized like a thermally activated phenomenon in which ET follows Arrhenius-like relation (equation 2).

(*Equation 2)*

$$k_{ET} = k_{ET}^{\circ}\, e^{\left(\frac{-Ea}{kT}\right)}$$

Where k_{ET} is the electron transfer rate, E_a is an activation energy barrier, and k is the Boltzman constant.

The hopping electron transfer process could be described as series of transfers steps between relatively stable sites, where the charge can be temporarily trapped in a potential energy well. The mechanism exhibit linear distance dependence as $\sim d^{-1}$ and follows a dependence on driving force predicted by Marcus theory[52] [53] [54]. The time that an electron spends in each of the potential wells, compared with the time required for molecular reorganization, is a fundamental information in evaluating the role of nuclear motion in the electron transport mechanism. If the molecular wire is composed by many subunits, the transport process can be viewed as a tunneling between a series of potential wells or, alternatively, as a series of successive electron transfer hops between radical ion stations.[55]

4 Polypyridine-based metal complexes

Polypyridines represent an extended class of multidentate ligands in which nitrogen is part of more or less extensive aromatic systems. The extended conjugation together with the particular chemistry in metal complexation makes polypyridines widely used organic systems. Figure 7 reports some of the most used polypiridines.

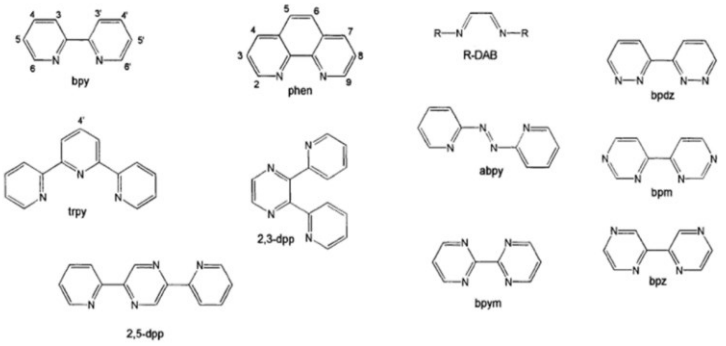

Figure 7 polypyridines most used in the of metalorganic and supramolecular synthetic field

The complexes in which polypyridines act as ligands are particularly interesting for various reasons, including the high constant of association with metal ions as well as a series of peculiar physico-chemical properties. Among these, thermal stability, low tendency to photodegradation and high resistance to electrical stress.

The metal-polypyridine complexes reconcile the chemical stability of the binders with the chemical, optical, magnetic, and electrical properties of metal. They also offer broad application flexibility, due to the possibility of modulating the spectroscopic characteristics of the complex, using ligands with different substituents and/or changing the metal ion.

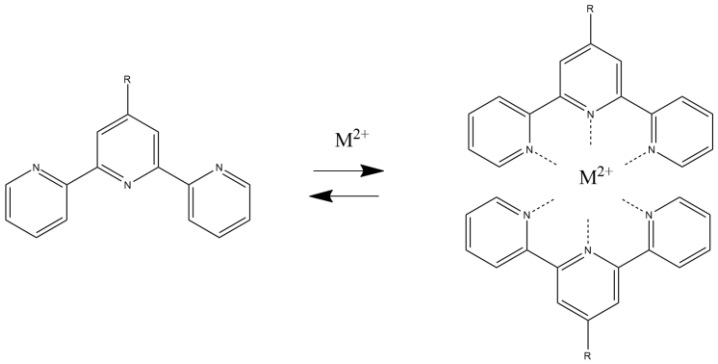

Figure 8 representation of a generic complexation reaction of a divalent metal with a terpyridine with the formation of "M (tpy) 2"

In the field of supramolecular chemistry, many metal-complexes are excellent building blocks for assembly, as they make it possible to create very ordered molecular architectures. The advantages they offer in the aspects related, for example, to self-assembly, can be attributed to the various geometries that can be obtained using different ligands and exploiting the specific coordination numbers of each metal ion[56].

Among the variety of polypiridinic ligands, terpyridine derivatives are widely used as molecular units also in supramolecular and macromolecular chemistry. In particular, the 2,2 ': 6', 2 " - (tpy) terpyridine derivatives are tridentate ligands that can complex, with a high association constant, different transition metal ions according to the scheme in figure 8. The use of the metals of block d, allowing the establishment of MLCT (Metal-to-ligand charge-transfer) and LMCT (ligand-to-metal charge-transfer) charge transfers makes these systems very suitable for the assembly of supramolecular structures capable of expressing interesting functions such as charge transport and / or photoconduction[57].

Some studies, such as those conducted by Krebs et al., show promising results in the field of hybrid photovoltaics, proposing cells assembled from “classic” inorganic substrates functionalized with single molecular structures or polymers based on Ru (Tpy) 2 complexes[58].

In the supramolecular field, the research group of Higuci et al. succeeded in assembling bimetal-supramolecular terpyridine polymers. More precisely, these systems have been realized by exploiting the coordination of metal ions such as Fe (II) and Ru (II) by bifunctional units (bis-terpyridyl benzene), thus succeeding in

assembling one-dimensional supramolecular structures with interesting electrochemical properties[59].

In the field of surface engineering, a work by Tuccitto et al. has successfully shown the possibility of using metal-polyterpyridine complexes also for the realization of sensing devices [60]. More precisely, the surface of different conducting oxides has been functionalized with a SAM which exposes as a tail group a terpyridine capable of hooking, by exploiting the iron ion, oligonucleotides in turn bearing, at one end of the chain, a terpyridine functionality. A molecular platform was thus built that is able to recognize, by hybridization with the complementary sequence, different forms of DNA. The same group, using a similar logical set-up, but making the necessary changes to the molecular systems and substrates, carried out studies for the selective recognition of model protein systems. This was possible by engineering gold surfaces with SAMs mixed with 4A(4-Mercaptophenyl)-2,2A:6A2B-terpyridine (MPTP) and mercapto-benzene (MB) [61 62].

Within the area of research aimed at the production of organic structures for molecular electronics, systems consisting of active redox centers produced using the complexation of the ruthenium (II) ion by (poly) terpyridines are of great interest. These coordination compounds are thermodynamically stable and kinetically inert (a necessary condition so that there is no exchange of ligands). They are usually achiral, if they do not have asymmetrical ligands, and they arrange themselves in space with a pseudo-octahedral coordination geometry. This affects the electronic structure of the whole complex, which is characterized by the presence of non-binding border orbitals with t2g symmetry responsible for the oxido-reductive activities[63]. The set of features mentioned above makes Ru-Tpy complexes suitable for the construction of linear supramolecular structures (wire-like). The assembly of polynuclear molecular architectures consisting of several active Tpy-Ru-Tpy redox centers, separated by highly conjugated molecular portions (henceforth called separators), increases the photochemical and photophysical properties compared to the mononuclear Ru (tpy) 2 [64]. All of this suggests that Ru- (tpy) 2 complexes are widely expendable for the construction of molecular wirewires with conductive and / or photoactive properties. Such molecular wires, if assembled on suitable solid surfaces, would be potentially very useful for the production of different technological devices, such as for example photoanodes for hybrid photovoltaic cells or diodes or molecular photodiodes.

5 Electrochemiluminescence methods.

Electrochemiluminescence (ECL) is an electrochemical process in which specific luminescent molecules solubilized in a solvent undergo highly exergonic electron-transfer reactions at an electrode surface to produce an electronically excited state that then emits light .The entire process is promoted by the application of a voltage[65,66].

There are two dominant pathways through which ECL can be produced, known as annihilation and coreactant pathways.

In the annihilation pathway, two species are electrochemically generated; for instance, oxidized and reduced forms of the luminophore are produced within the depletion zone by a potential step or sweep. These species then interact to produce both a ground state and an electronically excited state, which then relaxes by emission. An advantage of the annihilation pathway is that it requires only the electrochemiluminescent species, solvent, and supporting electrolyte to generate light. However, the potential window of water is often not sufficiently wide to allow the luminophore to be both oxidized and reduced, making it necessary to use organic solvents such as acetonitrile and N,N-dimethylformamide. An example of annihilation ECL pathway is given by dipicolinic acid (DPA). The reactions steps involved in the annihilation pathway mechanism of DPA is schematically represented as follows:

$$DPA \rightarrow DPA^{+} + e^{-} \quad \text{(electrochemical step occurring at } E^{\circ}_{1})$$

$$DPA + e^{-} \rightarrow DPA^{-} \quad \text{(electrochemical step occurring at } E^{\circ}_{2})$$

$$DPA^{-} + DPA^{+} \rightarrow DPA + {}^{*}DPA$$

$${}^{*}DPA \rightarrow DPA + \text{light emission at 425 nm}$$

On the other hand, in the coreactant pathway mechanism, a species present in the solution, such as tripropylamine (TPrA), is either oxidized or reduced in the same potential step as the ECL species. Through electron transfers or chemical reactions that follow electron transfer, the coreactant generates a product that reacts with the ECL luminophore to generate an excited state. A coreactant can be defined as a chemical species that, upon electrochemical oxidation or reduction, produces very reactive intermediates capable to react with the oxidized or reduced luminophore to

generate the desired excited state. In the case of ruthenium-bpy-based ECL, amines—especially tertiary amines such as TPrA—are the dominant coreactants[67,68].

A key advantage that this method offers is the possibility of individuate ECL generation conditions in aqueous solution. This aspect has made possible the use of this electrochemical process, with high selectivity, for the detection of diagnostic biological targets and of several molecular compounds, both in very low concentration.[69]

A lot of technology has been developed in the recent years in order to obtain highly sensitive photon detection systems, which are evolving to be even more sensitive and smaller as possible. This has led to the incorporation of light emission reactions into highly sensitive analytical methods and tools. A fundamental advantage provided by ECL approach is the very high signal/noise ratio. This because, at variance of standard fluorescence techniques, in ECL methodologies no external light stimulation is needed. This means that light scattering, and the related background signal is suppressed, so that the virtually background-free detection of ECL can reach higher signal- to noise ratios and lower limits of detection. Besides, ECL is a highly localized and time-triggered detection method, since ECL signal generating reactions will only take place at the electrode for the range of time in which a specific voltage is applied.

The photochemical characteristic of luminophore play obviously a key role in the entire ECL process. Since the beginning of ECL applications, metal organic complexes have attracted a lot of interest due to the large spectrum of opportunities that such systems can offer in the tuning of several chemical important characteristic. Indeed, the hydrophobicity, excited-state location within the complex, luminescence lifetime, wavelength of maximum emission, and both ground- and excited state redox potentials can be optimized in each specific applications by changing ligands and metals [70] [71]. For example, longer excited-state lifetimes may lead to a brighter ECL response, making the assay more sensitive, and reducing the redox potentials.

Historically, the most common metalorganic complex luminophore, that is still a reference in luminophore ranking, is tris(2,2′-bipyridine)ruthenium(II) $[Ru(bpy)_3]^{2+}$. It is widely employed in analytical ECL applications due to its higher light-producing efficiency, good stability and best performance in aqueous solutions.[37,38] Moreover, due to its long shelf life and low cost, $Ru(bpy)_3^{2+}$ and its derivates. has attracted increasing attention in immunoassay as ECL label, in comparison with other luminophores such as luminol or acridinium ester, because it can be uninterruptedly recycled for reuse[72]. $Ru(bpy)_3^{2+}$ ECL, usually in combination with

coreactants, has been widely applied to determine substances such as drugs, food additives, natural products, and environmental pollutants[73] [74] [75].

In order to enhance the light emission performance of luminophores a typical strategy is based on linking, via different molecular bridges, several metalorganic metal centers into the same metalorganic structure, thus forming systems like dimers and dendrimers. But, even systems in which several metallic units are arranged in the same molecular structure the typically yield increase in ECL intensity is not more than ~30% compared to the mononuclear luminophore[76]. This nonlinear enhancement effect of ECL intensity can be ascribable to the rate of diffusion or to heterogeneous electron transfer that, more than the quantum yield of the luminophore, set the upper limit of ECL intensity.[77]

The use ECL for bioanalytical aims starts from the idea of labeling with ECL active systems, organic structures that can specifically bind to the biological target of interest. Indeed, by means suitable groups attached to the bipyridine moieties of $Ru(bpy)_3^{2+}$ the complex can be linked to biologically interesting molecules, such as antibodies or single stranded DNA, where it serves as a label for trigger the ECL light output signal that testify the interaction between target and receptor. Nowadays, $Ru(bpy)_3^{2+}$ or its derivatives as label and TPrA as a coreactant form the basis of commercial systems for ECL immunoassay recognition of DNA and other biological targets. However, the bioreactivity and the bioaffinity of biomolecules is often altered by a high degree of multilabeling at multiple functional sites[78] [79] [80].

In figure 9 and figure 10 are schematically represented two typical set-up of a ECL experiment for biological targets recognition. In figure 9 represents a single-stranded DNA anchored at the electrode surface that recognizes the complementary ssDNA target which in turn is tagged with the ECL label. In this case the electrode assembly is exposed in a solution or flow-cell containing the coreactant that will trigger the ECL of the tagged target. Similarly, figure 10 represents the approach known as sandwich-type, where the analyte is an antigen that is captured by a proper antibody immobilized at the electrode and then recognized by a labeled antibody.[76]

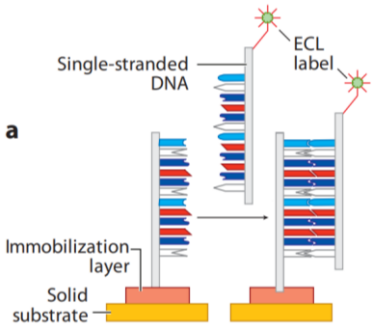

Figure 9 Schematic diagram of solid-state ECL detection of DNA hybridization

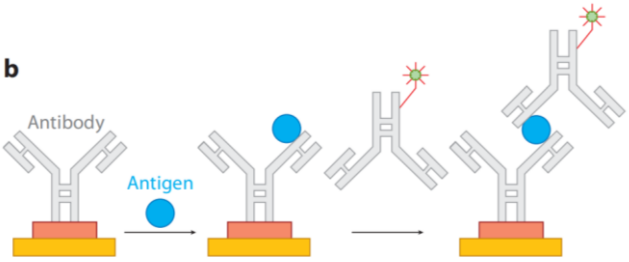

Figure 10 Schematic diagram of solid-state ECL detection of sandwich-type immunoassay

The use of fluid phase reactants flows into the electrochemical cell on one hand allows to design ECL assays in physiological fluids condition but on the other hand introduce several disadvantages such as signal reduction, bad reproducibility and high reagent consumption[81]. These issues are often related to the weak binding interaction between surface of transducer and biomolecule. To overcome these issues several strategies have been developed to produce stable chemical platforms on substrates that should be able to strongly anchor the biomolecule, to keep unaltered their functional properties and at same time not suppress the electrical properties of the electrode surface. It was demonstrated that self-assembled monolayer formation of $[Ru(bpy)_2dcb]Cl_2$ on FTO electrodes exhibit a stable, electrochemically reversible redox response also providing a wide linear range, low detection limit, and good reproducibility in detection of proline.

Another way to enhance ECL response involves the use of metallopolymer thin films as immobilization layer. Electrodes modified with thin layers of the redox polymer, $[Ru\text{-}(bpy)_2PVP_{10}]^{2+}$ have proved to be sensitive and selective for detection of oxalate in a flow injection analysis system and stable over relatively long-time scale. In the case of polymer other issues come out, such as self-quenching processes due to the higher localized concentration of luminophore and low diffusion coefficient of coreactant into polymeric matrix.

In view of the above limitations, nanomaterials of different nature have been proposed for the design of matrix in ECL devices because of their properties such as conductivity, transparency, enormous surface area-to-volume ratio, catalytic activity, durability, biocompatibility and a typically tunable surface chemistry. Hence, in order to obtain better performances in terms of sensibility and selectivity, many components of ECL biosensors are frequently planned to integrate nanomaterials. In particular, nanomaterials are involved in the construction of the electrode, which constitutes solid interface where the majority of redox reactions take place, but also as carriers for loading numerous signal elements such as enzymes, oligonucleotides and redox labels, and the luminophores that play as electroactive tracers for signal amplification. The use of nanomaterial together with the development of microfluidic made possible the downsizing of the ECL devices, and allowed the fabrication of highly sensitive analytical ECL assays at microscale.

One of the first studies that attracted the attention on the use of nanostructured systems was related to the background signal reduction effect when ECL signal is generated near a very thin gold film. This phenomenon is known as surface plasmon-coupled electrochemiluminescence (SPCECL).[82]

Metallic based systems like AuNP shows a low cytotoxicity and high affinity with a wide range of enzymes and biomolecules. In addition, their size, shape, and surface properties can be easily tuned to anchor several biological receptors. Zhu obtained a bio bar-coded gold employing nanoparticles (Au NPs) and DNAzyme, an ECL aptasensor ultrasensitive and selective for detection of thrombin in real samples[83].

Carbon based nanomaterials are often used for electrode modification due to their high conductivity, large surface area and electrocatalytic role in many electrochemical reactions[69]. Among them, carbon-based nanotubes and carbon dots are mostly employed as materials used to improve the performance of ECL devices. The nanometric structures named as carbon nanotubes can be divided in two big categories: single-walled carbon nanotubes (SWNT) that are constructed of a single sheet of graphite (diameter 0.4–2 nm) and multi-walled carbon nanotubes (MWNT) that is multiple concentric graphite cylinders with diameters from-to (2–100 nm)[84].

In addition to their metallic and semi-conductive electronic properties the carbon-based nanotubes are characterized by high tensile strength, ultra-light weight, chemical and thermal stability[85]. Instead, carbon dots are typical one-dimensional (carbon nanoparticles like) or two-dimensional (graphene like) systems with interesting properties such as fluorescence properties, biocompatibility, high stability also in water environment, easy functionalization through carboxyl moieties produced at surface, not expensive and easily to be synthetized by means of a plenty of procedures[86] [87] [88]. It is notable the capability showed by single-walled carbon nanotube (SWCNT) forest electrode developed by Rusling, that allows the attachment of antibodies and exhibit very low detection limits for immunoglobulin G, such as 1.1 ± 0.1 pM IgG recorded under optimal assay conditions.[89]

Valenti et al. have demonstrated that carbon-based nanotube electrodes are excellent materials for ECL applications thanks to the overpotential of the oxidation of amine derivatives, which are generally employed as co-reactants in commercial devices. In this work, CNTs played a critical role in the enhancement of ECL intensity[90].

It's also known that MWNTs can act as quenchers of ECL signal, and this effect is typically ascribed to the oxygen groups at the surface of MWNTs and to their peculiar electron properties.[91]

Recently, much attention has been focused on fluorescent carbon quantum dots (CQDs), which have been evaluated as good candidate for luminophore systems in ECL setups. The photo-electrochemical properties of CQDs are usually tuned by adding dopant elements such as (B, N, P, S) but also by modifying the amount of oxidized chemical group at the surface, that can be nominally positively or negatively charged. [92] [93] [94] In particular, Kang and Niu compared the ECL properties of pristine CDs, oxidized CDs (oCDs), and partially reduced CDs (rCDs). In radiative annihilation ECL mechanism CDs, oCDs, and rCDs produce stable positively charged luminophore ($R^{+\bullet}$) and unstable negatively charged luminophore ($R^{-\bullet}$) at the surface of GCE (glassy carbon electrode) and showed a 365 nm emission peak and emission range from 550 to 850 nm, which was unusual for ECL of CDs. The weaker ECL emission of rCDs and the negligible ECL emission of F-rCDs (fully reduced-CDs) further confirmed the indispensable contribution of oxygen containing groups to ECL of CDs. The multiemission ECL property might provide potential and novel application in light emitting electrochemical cells (LECs) [93]. They also used computational models to investigate and simulate the ECL properties of CDs, further confirming the contribution of oxygen containing groups to ECL of CDs and deducing the functional groups on the periphery of CDs.[93]

Another big class of material used in the design of ECL electrodes is represented by metal oxides nanostructured system [93-95]. The most commonly used metal oxide is the titanium oxide. Nano TiO_2, with different shapes from nanosphere to one dimensional and even three-dimensional structures, are commonly recognized as promising nanomaterial for ECL due to their better electron transition, the possibility to tune the conductivity by metal doping procedures, their inexpensiveness, and the remarkable non-toxic and biocompatibility properties.[96,97,98]

Kobayashi et al explored the role played by TiO_2 NPs when added into a Ru(II)-complex-based electrolyte. They demonstrated that rutile-TiO_2 NPs markedly improve the ECL properties of an AC-driven ECL device (emission luminescence, 165 cd m^{-2} half-life time, 1000 s) compared to same set-up but without TiO_2 NPs addition. Focusing the attention on emission luminescence and long-term stability and electrochemical properties of the $Ru(bpy)_3^{2+}$-based ECL they propose that TiO_2 NPs suppress the non-radiative quenching of the excited states of the $Ru(bpy)_3^{2+}$ complex. In particular, it seems that the electron transfer occurs from the reduced species of $Ru(bpy)_3^{2+}$ to the TiO_2 NPs and, subsequently, from the TiO_2 NPs to the oxidized species of $Ru(bpy)_3^{2+}$. This suggested electron transfer phenomena improves the balance between the redox reactions in the ECL device, leading to long-term stability.[99]

The TiO_2 shaped as nanotubes (TiO_2 - NTs) can be used to obtain nanostructured substrates that are able to amplify the ECL detected signals. TiO_2 NTs-based ECL sensors have been widely studied by Xu et al, reporting positive results in terms of sensitivity for the determination of amines in water with a limit of detection of 1.0×10^{-9} M by immobilizing $Ru(bpy)_3^{2+}$ into TiO_2 NTs substrates. In this nanoscopic tubular configuration the enhancement of ECL signal response is ascribed to short diffusion path for active molecules from the solution to the active surface.[100]

Nanostructured ZnO based systems represent another promising material useful to enhance the performance of ECL signals. The main advantages that were reported on ZnO based nanorod arrays are attributed to large surface-to-volume ratio and high electron mobility. These properties lead to fast and inexpensive biosensors device characterized by optical signal amplification or electronic signal amplification.[101]

An ECL biosensor based on a highly oriented CdS-coated ZnO nanorod array has been successfully fabricated and applied to the immunoassay of HepG2 cells for the first time. The CdS-coated ZnO nanorod array is of high surface area and thus gives rise to enhanced ECL properties compared with the pure CdS nanoparticle film. All of these desirable properties spur further development of novel ECL immunosensors

for HepG2 cells. A broad detection range from 300 to 10 000 cells per mL has been achieved, with good selectivity and reproducibility.[70]

6 ToF-SIMS.

Many methods used for the study of solid surfaces are based on the detection of particles (photons, electrons, atoms and their aggregates in different state of charge) emitted by a suitably stimulated surface (typically with photons, electrons, energetic ions). This type of investigation includes techniques such as photoelectron spectroscopy (XPS)[102] Auger spectroscopy (AES) [103], X-ray fluorescence techniques such as EDX (electron induced X-ray fluorescence)[104] and PIXE (proton induced X-ray fluorescence)[105], secondary ion mass spectrometry (SIMS) and several other techniques. Among the most commonly used methods, secondary ion mass spectrometry (SIMS) plays an important role. Moreover, it has been widely used in this thesis, so that a short outlive of its main features is given in the following.

SIMS has been used for over fifty years, mostly to support the semiconductor industry, where it has been and continues to be used for process development and process monitoring, such implantation of element in doping process of silicon and silicon carbide substrates[105] [106]. Nowadays, the boost provided by the industry allowed the development and spread of SIMS instrumentation and methodology in many areas of science and technology, including biology, medicine , astrochemistry and material science.[107] [108] [109] [110]

Secondary ion mass spectrometry is based on the bombardment of a surface by ions of some keV energy, which leads to the emission of elemental species, clusters, fragments and even intact involatile molecules which are characteristic of the chemical structure in the uppermost monolayer of the surface. The ionized fraction of such species is then analysed by a mass spectrometer. The emission process is a consequence of the interaction processes between the bombarding energetic particle (primary ion) and the solid. Actually, the primary ion penetrates solid and transfers part of its kinetic energy to the atoms of the solid in a succession of individual collisions. Through subsequent collisions some of this energy can find its way back to the surface where it may cause surface particles to be emitted (figure 11). The entire process that leads to the removal of material from a solid surface is typically named as sputtering.[111] Most of the processes initiated by a primary ion (changes to the target and emission processes) are typically out-of-equilibrium processes, completed within less than 10^{-12} s, although some phenomena triggered by the initial interaction may last rather longer. As to the emitted materials, they have a non-Boltzmann energy distribution, typically peaked at about 10 eV.

The impact energy of the primary ion is transformed into movement of target atoms, the so-called collision cascade. A part of the energy is thus transported back to the

surface where its amount is just sufficient for the respective atomic and molecular compounds to overcome the surface binding. The major fraction of secondary particles produced is emitted as neutrals while only a fraction, ranging from about 10^{-6} to 10^{-1} of the total emitted material, are positively or negatively charged.

.

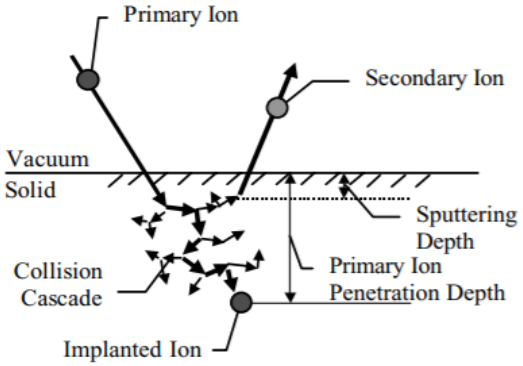

Figure 11 The collision cascade in SIMS. The primary ion finally comes to rest after a series of collisions during which displacements of the sample atoms occur. Some secondary species are ionized, and these are the secondary ions used in SIMS. Typically, the range of the primary particle is 1–20 nm in a SIMS experiment, depending on the primary beam energy used

It was J.J. Thomson, already in 1910, who suggested that some fraction of the atomic and molecular charged species leaving the surface can, therefore, be dragged by electric and/or magnetic fields and transmitted to a mass spectrometer for mass analysis [112].

The information depth in SIMS experiment is assumed to be basically limited to the top two or three atomic layers so that monolayer depth resolution is, in principle, possible in SIMS. In practice the ions are mostly being emitted from a region that has been 'mixed-up' by earlier collision cascades (in the so-called altered layer) so that sub-surface atoms will have been moved to the surface and will form part of the secondary ion signal. This is not true if the primary ion dose is less than $\sim 10^{12}$ - 10^{13} primary ions/cm^2 and in this regime, where each primary ion impact is on virgin surface, true mono-layer sensitivity is achievable (the Static SIMS regime)[113].The typical output of Static SIMS experiments are mass spectra and "chemical images" (see infra).

While static SIMS concentrates on outer surface (ideally the top monolayer), providing mostly molecular characterization, in dynamic SIMS mode, bulk composition and in-depth distribution of trace elements are investigated. In dynamic SIMS regime rather high ion fluences are used, in experiments where the solid under study is eroded by sputtering in order to expose increasingly deeper layers to surface. In this way, from the trend of the intensity of the detected ions as a function of the sputtering time it is possible to obtain depth profiles, that is (once the appropriate calibrations are done, and with certain limitations) the concentration of analyte species as a function of depth. Also, in dynamic mode it is possible to obtain mass spectra and chemical maps. It must however be taken into account that the information obtained can be distorted by various processes of mixing, diffusion, damage induced by the accumulating effects produced by the ion beam.

For a quantitative description of sputtering and secondary ion emission we consider a surface constituent M (either a molecular surface constituent or an atomic species) which is present in the uppermost monolayer with a relative coverage O(M) which is the ratio of the number N of such particles present in the uppermost monolayer to the maximum number N, that the surface can accommodate in a complete monolayer.

Equation 3

$$\mathrm{O(M)} = \frac{N}{N_0}$$

The sputtering of a surface particle M can in principle produce its conversion into any of a series of neutral or diversely charged secondary particles X_1^q, X_2^q, . . . X_i^q; . "q" is the charge state of the emitted secondary particle. In the case of a molecular surface constituent the series of species X_i^q will also include fragments of M.

The sputtering cross section σ identifies the equivalent area of a monolayer that corresponds to the average number of particles of species M disappearing as a result of the impact of a single primary ion.

The decrease of the relative coverage with time O(M,t) caused by primary ions arriving at a constant current density (ions s-1 cm-2) is described by equation 4.

Equation 4

$$O(M,t) = O(M,\mathrm{O})^{-v\sigma t}$$

With these simplifying assumptions one can also define the following quantities:

- The sputtering yield $Y_s(M)$, which indicates the average number of surface particles M that would disappear from a closed monolayer of particles of species M, (O(M) = 1) as a result of the impact of one primary ion.
- The secondary particle yield $Y(X_i^q)$ which specifies the average number of secondary particles of a given type X_i^q generated from a closed monolayer of particles M by the impact of one primary ion.
- The transformation probability $P(M \rightarrow X_i^q)$, which is the probability that the disappearance of a surface particle M as a result of primary ion bombardment will lead to the emission of a given type of secondary particle X_i^q.

These quantities are related in accord to equation 3 and showed in equation 5.

Equation 5

$$P\left(M \rightarrow X_i^q\right) = \frac{Y\left(X_i^q\right)}{Y_S(M)}$$

It is also possible define the useful yield Y_u that take in account via term T the overall transmission of the spectrometer involved in the discrimination of secondary ions.

Equation 6

$$Y_u\left(M \rightarrow X_i^q\right) = P\left(M \rightarrow X_i^q\right) T$$

All the parameters described above are very dependent on the nature of the samples and on the experimental conditions determined by the equipment used. The ways in which sputtering is induced together with mass analyzer technologies greatly affect the production-detection of all charged species produced.

In secondary ion analysis with a time-of-flight spectrometer (ToF-SIMS) it is essential that the ions to be analyzed enter the flight path simultaneously or at least within the shortest possible time interval, in order to discriminate the charged sputtered material only by time of flight (neglecting the relatively small initial energy of the secondary ions). To achieve this the area of the surface to be analyzed is bombarded with pulses of primary ions whose duration Δt_p, is kept as short as possible. In ToF-SIMS spectrometer the secondary ions produced by sputtering are collected into a path long L and accelerated by applying electrostatic potential U, by comparing the electrostatic energy contribution to the kinetic contribution it is possible to define the main equation of a ToF-SIMS experiment equation 7.

Equation 7

$$\frac{m}{z} = \frac{2UT^2}{L^2}$$

In the equation 8 The mass resolution Δm/m of a linear time-of-flight spectrometer is reported. As described above it is constrained by the primary pulse duration Δt_p. the time resolution Δt_D of the detection system, the initial energy ΔE of the emitted secondary ions, and the total flight time t.

Equation 8

$$\frac{\Delta m}{m} = \frac{\Delta E}{E} + \frac{2\left(\Delta t_p + \Delta t_D\right)}{t}$$

Thanks to very high surface-specific sensitivity, wide range of applications of time-of-flight secondary ion mass spectrometry are reported in all science field. Its universal applicability to practically all types of materials and sample forms compatible with ultra-vacuum condition, and its ability to give direct molecular information through the emission of molecular ions. As anticipated above the most common operation modes of TOF-SIMS are large-area or micro surface analysis imaging and depth profiling analysis.

6.1 ToF-SIMS Imaging

By reducing the diameter of the primary ion beam and scanning it over the surface region to be investigated one can measure the lateral distribution of the secondary ion emission, and consequently that of the surface constituents responsible for the emission. The lateral resolution is determined by the beam diameter. The primary ion beam is positioned at a particular point on the sample surface for a short interval, and the spectrum is recorded and stored with the relevant lateral coordinates. Typical beam diameters vary from a few μm down to some 10 nm. If, for instance the surface area analyzed is partitioned into 256 x 256 elements (pixels), this mode of operation needs that 65 536 complete spectra must be recorded. From these data one can then in principle construct an image for each secondary ion species or group of species displaying the distribution along the surface. The recording time needed for such images can vary from a few seconds to several hours. By adding together all the spectra, or only those from a selected region of the imaged surface, one obtains a total spectrum. As another option, one can add together all the positive or negative secondary ions for each image point and thus obtain a total ion image.

Making the beam diameter smaller reduces the amount of substance available per image point in the uppermost monolayer, and thus also the total number of secondary ions that can be generated from the corresponding surface region. This in turn reduces the sensitivity and dynamic range for each individual image point. By subsequently adding together spectra from a sufficiently large surface region the sensitivity and dynamic range can be partially restored.

Today the use of two-dimensional imaging via ToF-SIMS is widely spread in the most disparate fields of science, among these certainly the recent trend is the imaging of biological systems, lipid mimetic systems of cell membranes, development of treatments of surface to produce biocompatible surgical prosthetic device, characterization of contact lenses and also the study of the intracellular pharmacodynamics of some drugs[114 115 116 117].

In the recent years an enormous contribution to the study of two-dimensional imaging was given using software designed ad hoc in the management of large amounts of data, in fact, paying attention to the nature of an images, in the specific of a ToF-SIMS image, immediately realizes how an investigation on surfaces of a few square microns can produce files of such dimensions that becomes increasingly difficult to manipulate with standard computer devices. In order to reduce the amount of data to handle, numerous studies have been conducted using multivariate analysis approaches, such as PCA-based algorithms or using machine learning approach also when ToF-SIMS images are recorded on millimeter square dimensional scale.[118 119 120]

6.2 ToF-SIMS 3D Imaging

Three-dimensional SIMS, in some respect, can be considered an extension of the concept of depth profiling, obtained by retaining the lateral compositional information during the sputter erosion of the sample, at variance of standard depth profiling experiments where an average compositional information is collected at each depth. 3D-SIMS imaging can be described, in the most intuitive way, as a stacking of two-dimensional (x-y) images along a sampling depth (z). By combining these 2D images, it is possible to create a 3D one, where each elementary volume ("voxel") in the sampling volume represents the distribution of secondary ions emitted by a specific point of the sample characterized by the three coordinates. Experimentally this is possible using two approaches, one based on a single beam that provides both an erosion action of the sample and a production of secondary ions, the other method, indicated as dual beam, involves the use of two different ion beams samples that insist on the same portion of the sample. One of these beams is

entrusted with the task of sputtering, the other with the role of analyzing the surface produced after the sputtering action. By cycling the sputter beam and analysis beam it is therefore possible to record a depth profile. This last experimental set-up is that used in time-of-flight instrumentation, and it is well suited for optimal management of the experimental conditions, since it allows to decouple sputter erosion from analysis, which experimental parameters (energy and beam current, as well as pulse width and timing parameters) are set independently. A limitation the dual beam approach arises from the fact that the material removed from the sample by the sputter beam, which is by far the largest fraction of the total sampled volume, is not used for analysis, that is given instead by the relatively few ions (compared with those produced by the sputter beam) produced by the low-current analysis beam. Recent developments in the technique combine, in the same SIMS instrument, a ToF analyser (which is the most suitable for obtaining the low-intensity, high-lateral resolution images produced by the low current analysis beam) with an Orbitrap mass spectrometer, used for analyzing the ions produced by the sputter beam during the erosion cycle, with limited lateral resolution but extremely high mass resolution[121].

Common objective in a dynamic SIMS experiment (either one-dimensional depth profile or 3D imaging) is to follow the distribution of minor and trace level elements as a function of depth. The ion beam is scanned over the surface, usually in a square digital pattern, ensuring that beam overlap exceeds 50%. Under these conditions the primary beam flux is constant over an extended area and a flat-bottomed erosion pit or crater should be ensured. Care is taken to ensure that the secondary ions being counted are emitted from the flat central part of the crater, to avoid crater edge effects that degrade depth resolution. During a SIMS experiment, and in particular in 3D ToF -SIMS depth profile measurement, problems related to the electrostatic charging of the sample may arise, especially when insulating layers are involved. To overcome charging problems, usually a flow of low energy electrons produced by a "electron flood gun" is used to balance the electrostatic charging phenomena of the bombarded surface.

As mentioned, a side effect induced by the sputter beam in dynamic conditions is the damage of the sample over a thickness of the same order of magnitude of the penetration depth of the primary ion. Damage includes mixing of target atoms, diffusion phenomena and other processes, such as ion induced chemical reactions, that are originated by the energy deposition from the primary ion to the target, as well as the implantation of the primary ion species. If the damage of the pristine characteristics of the material accumulates during the measurement, the experimental results can suffer of large artifacts, as the information (secondary ions) representative of the nature of the sample can be distorted or even totally lost. Rather

obviously, such effects are more noticeable in the case of organic or polymer systems, organic-inorganic hybrid systems or metalorganic-based multilayers rather than in inorganic materials.

In order overcome the phenomena induced by damage, various types of beams have been proposed, from ultra-low energy Cesium ion beams, to fullerene beams, to large cluster beams (GCIB, giant cluster ion beams), i.e. clusters ions (with a few charges) containing hundreds or thousands of noble gas atoms (argon) or small molecules (O_2, water, CO_2). By using these experimental approaches, depth profiling of damage-sensitive samples becomes in many cases feasible. However, it is still far from a satisfactory solution the problem of depth profiling and 3D SIMS imaging of hybrid systems, in which regions with very different sputtering behavior (in terms of sputtering rate and degree of beam induced damage) do coexist in the same sample.

In any case, for those situations in which a depth profile or 3D image can be obtained, many studies in the literature remain aimed at obtaining the best SIMS output in terms of signal intensity, sputtering yield and lateral resolution[122].

The ToF-SIMS signal intensity of a generic species A, called I^A (ions/s), is given by Equation 9:

Equation 9

$$I^A = I^P \times \mathrm{C}_A \times \mathrm{Y}_{\mathrm{TOT}} \times \alpha_A \pm \times T_{\mathrm{A}} D_A$$

Where:

I^P is the primary ion current flux (ions/s):

By increase this parameter it's common to increase the damage/contamination produced by primary ion beam flow.

C_A is the A species concentration

$\mathrm{Y}_{\mathrm{TOT}}$ is the total sputtering yield

$\alpha_A \pm$ is ionization probability

It is dependent strictly by the chemical nature of A and by the chemical environment where A is placed. It is named as matrix effect.

$T_{\mathrm{A}} D_A$ are instrumental factors related to transmission and efficiency of detection.

The sputtering yield it is a fundamental parameter that is important to take in account looking at ToF-SIMS depth profile because, depending strictly by experimental

condition and by chemical nature of the sample it can be easily altered by accumulation of sputter induced damage but also by when interface with native different chemical structures are sampled during the 3D ToF-SIMS experiment.

The sputtering yield is defined by the equation

Equation 10

$$Y = \frac{d\ A\ \rho \frac{N_A}{M}}{I \frac{t}{e}}$$

d is the thickness of eroded layer of the sample

A is the investigated area

ρ is the material density

M the atomic mass

N_A the atomic number

I is the used ionic current

e is the unitary charge

t is time necessary to sputter the measured thickness.

In order to increase the signal intensity, the data can be recorded by increasing the time dedicated to the analysis cycles. This approach, increasing the dose, match goes perfectly in opposite direction than the aspects related to the damage accumulation that occurs mainly in organic based compounds. Therefore, in most of the cases, the amount of signal that can be integrated is limited. Kollmer [122] introduced the concept of Useful Lateral Resolution (L), which defined the resolution that could be reached by a signal-noise ratio for molecules with a given disappearance cross-section. the Useful Lateral Resolution L for a signal-to-noise ratio s it is represented by equation 11.

Equation 11

$$L(d) = s\sqrt{\frac{A}{\sum_0^d I}}$$

Where:

I is the signal intensity which may vary with depth from an area A and d is the thickness of the sputtered material. Therefore, if I is constant as material is sputtered then L increases as $\sqrt{d}$.

7 Fe-TERPYRIDINE-BASED SUPRAMOLECULAR ARCHITECTURES ON OXIDE SURFACES.

The first part of the PhD project is focused on the study of molecular systems having functional properties suitable for surface engineering of different types of solid substrates that can be exploited for designing innovative devices in the field of nanoscience and nanotechnologies, such as photoactive molecular wires or modified electrodes for spatially resolved ECL.

7.1 Materials and methods

The first step of the surface modification with functional molecules is the phisyco-chemical characterization of the molecular building blocks that will be involved in the experimental procedures, based on iterative coordination reaction, aiming to build up a self-assembled monolayer of polynuclear metal-terpyridine complexes.

Prior to the analysis of self-assembled monolayers grown on different substrates, the polynuclear metal-terpyridine complexes have been synthetized and analyzed in solution.

Two molecular systems have been chosen as building blocks:

1) 4′,4 ′′′′- (1,4-Phenylene) bis (2,2 ′: 6 ′, 2′′- terpyridine), shown in figure 12, that will be referred as DT.

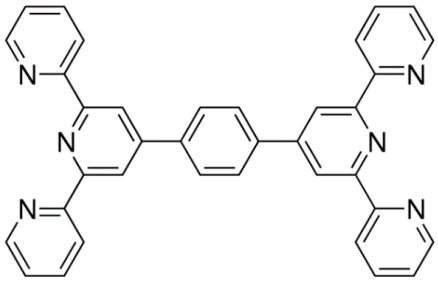

Figure 12 (4', 4'''' - (1,4-Phenylene) bis (2,2 ': 6 ', 2''- terpyridine) named as DT

2) 4 ′, 4 ′′′′ - (5-Methyl-1,3-Phenylene) bis (2,2′: 6′, 2′′ - terpyridine), shown in figure 13, that will be referred to as wDT.

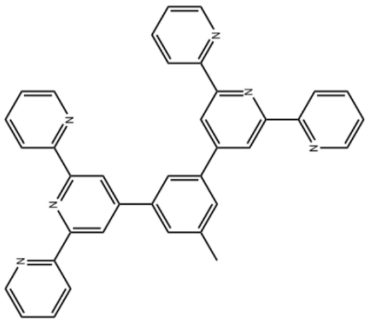

Figure 13 4 ', 4 '''' - (5-Methyl-1,3-Phenylene) bis (2,2 ': 6 ', 2 '' - terpyridine) named as wDT

Sample preparation involved the use of the following solvents, substrates and compounds:

• DT (4 ′, 4 ′′′′ - (1,4-Phenylene) bis (2,2′: 6′, 2′′- terpyridine)

• wDT (4 ′, 4′′′′ - (5-Methyl-1,3-Phenylene) bis (2,2 ′: 6 ′, 2 ′′- terpyridine)

• Deionized water (MilliQ^{TM} quality)

• Iodine mix (H_2SO4, KIO_3, KI)

• $POCl_3$

• $ZrOCl_2 \cdot H_2O$

• Zn (II) trifluoromethanosulfonate

• DMF N, N-Dimethylformalmide

• HCl

• Ethanol CH3CH2OH

• $FeSO_4 \cdot 7H_2O$

• PPTP, 4- (2.2 ': 6', 2 " - terpiridin-4yl) benzenphosphonic acid

• Quartz

• Silicon 100

• ITO on glass (Agilent)

All chemicals and materials listed above have been purchased from Merck | Italy - Sigma-Aldrich and used as received, with the exception of wDT and PPTP, synthesized ad hoc.

The assembly of the different molecular systems on substrate's surfaces consists of two fundamental phases:

i) a priming procedure, in which the solid substrate undergoes a treatment suitable for preparing its surface for the anchoring of the molecular system involved in the functionalization procedure. In this work we adopted the procedure called ZP priming[35, 36], already described in paragraph 1.1, that results in the formation of a Zr(IV) phosphate monolayer at the surface;

ii) the formation of a platform SAM by exposure of the surface to PPTP, which links to Zr via the phosphonic acid headgroup and exposes the terpyridine moiety towards the surface.

iii) the stepwise growth of the supramolecular metalorganic systems by alternative immersion of the PPTP platform in a Fe^{++} -containing solutions and in a DT (or wDT) solution (Figure14)

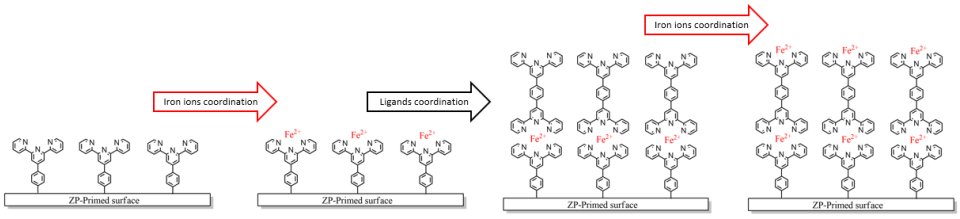

Figure 14 Scheme of molecular wire assembly strategy for oxide surfaces functionalization.

Samples grown on transparent quartz or ITO (Indium-Thin-Oxide) substrates were mainly used for UV-Vis spectroscopy measurements, while those on silicon oxide (supported on silicon wafers) for ToF-SIMS characterization.

The samples were analyzed by means of UV-Vis spectroscopy and time-of-flight secondary ion mass spectrometry (ToF-SIMS). The first was used for the study of the growth of the photoactive metal complexes, while ToF-SIMS (ToF SIMS IV, IONTOF GmbH) allowed us to obtain information on surface composition and, from the study of fragmentation patterns, additional information on the nature of the

adsorbed layer, e.g. if it is the result of a real supramolecular architecture grown at the surface or just due to species unspecifically adsorbed at the surface.

7.2 UV-Vis spectroscopy

Figure 15 shows the overlay of the spectra of DT/ chloroform solution (line red) and wDT / chloroform solution (line blue) in the UV region, recorded for comparison purposes with the spectra of the complexes where the two molecules act as ligands.

Due to the different structures, the two molecules show a quite different UV-Vis spectrum. In the case of the solution containing DT we note the presence of two peaks, while for the wDT molecule only a single broad absorption band is present in the spectrum.

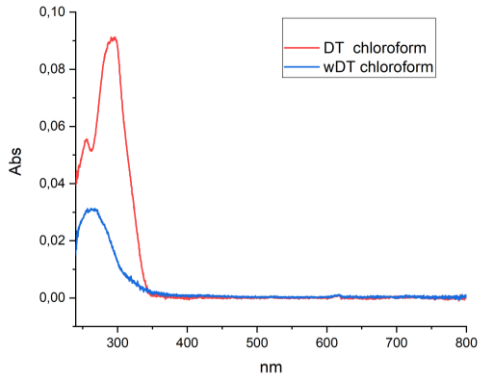

Figure 15 UV-Vis spectra overaly of DT/ chloroform solution (red line) and wDT / chloroform solution (blue line) into UV region.

The absorption spectra of the coordination complexes formed by each of the two ligands (DT and wDT) with Fe^{2+} (Fe_nDT_n and Fe_nwDT_n respectively) were measured in various solvents. Figures 16 and 17 report, in particular, the spectra of the DT-Fe and wDT-Fe systems, respectively, dissolved in a chloroform-ethanol mixture.

The spectrum of DT-Fe system shows an absorption peak at 588 nm, due to the metal-to-ligand charge transfer (MLCT) transition. The absorption in the 300 nm

region is mainly related to the electronic characteristic properties of the ligand, however influenced by the coordination with the metal centre.

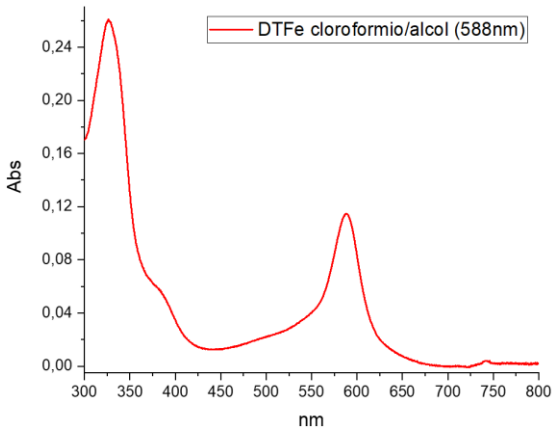

Figure 16 UV-Vis spectrum of DT-Fe based coordination oligomers

Similarly, the spectrum of wDT-Fe systems (Figure 17) a MLCT band at 568 nm related to the metal-to-ligand charge transfer (MLCT), and a strong absorption in the UV region, again related to the electronic characteristic properties of the ligand portion of the complex.

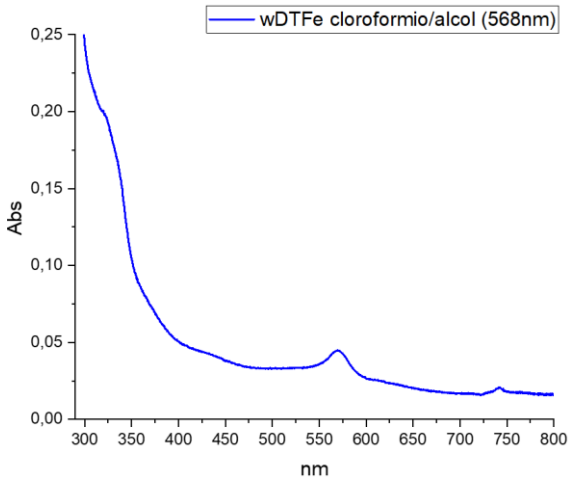

Figure 17 UV-Vis spectrum of wDT-Fe based coordination oligomers

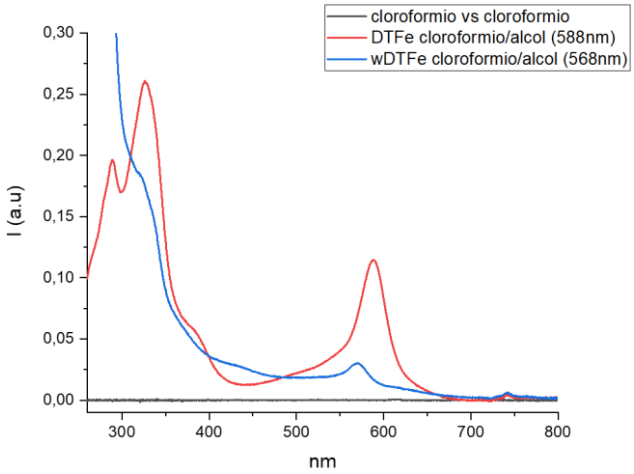

Figure 18 Overlay of UV-Vis spectra related to DT-Fe complex in solution (red line) and wDT-Fe (blu line) complex in solution.

The overlay of Figure 18 clearly shows a 20 nm shift between the MLCT transitions of the two different organometallic complexes. In terms of energy of the transition, it corresponds to a difference of about 0.075 eV.

Both complexes show an absorption band at 330 nm in the UV-Vis spectrum. Amongh the two system (Fe-DT and Fe-wDT), only metalorganic complexes made employing DT show two resolved peaks in the UV region of the spectra.

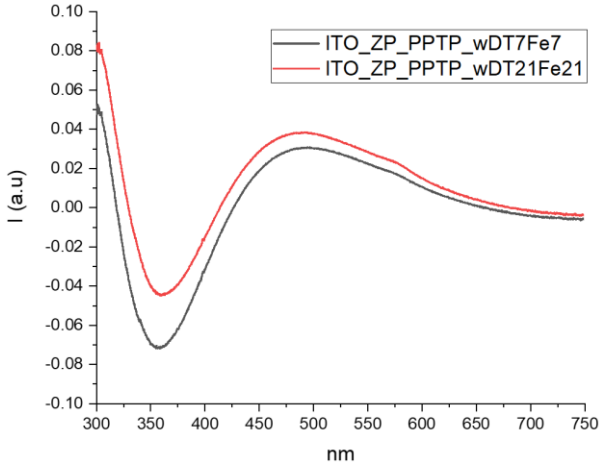

Figure 19 Overlay of UV-Vis spectra related to wDT-Fe multilayers assembled on ITO (7 nominal layers in black and 21 nominal layers in red)

Figure 19 shows the UV-Vis spectra of wDT-Fe multilayers assembled on ITO obtained after 7 (black line) and 21 (red line) iterative reaction cycles. The spectra, recorded against air as reference, mainly show the peculiar shape of absorption spectra of ITO substrate that is characterized by a absorption minimum at 360 nm and a relative absorption maximum around 491 nm.

By subtracting each other the two spectra of figure 19, we see (figure 20) that there is there is a very small increase in the absorption in the MLCT region of the adsorbed complex, indicating a poor growth of the wDT-based system on the surface.

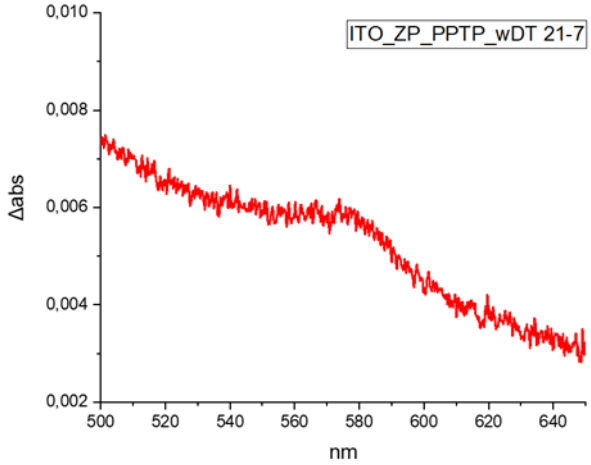

Figure 20 Difference of UV-Vis spectra of two wDT-Fe multilayers assembled on ITO with, respectively, 21 and 7 iteration cycles (nominal layers)

The results are completely different when the DT molecule is used (instead of wDT). Figure 21 shows the UV-Vis adsorption spectra, recorded in similar conditions of those of fig. 19, of FeDT multilayers on ITO, assembled with 10 (sample A - black line) and 20 (sample B - red line) iterative reaction cycles. These samples show a strong absorption peak related to the MLCT transition of the photo-active center around 590 nm.

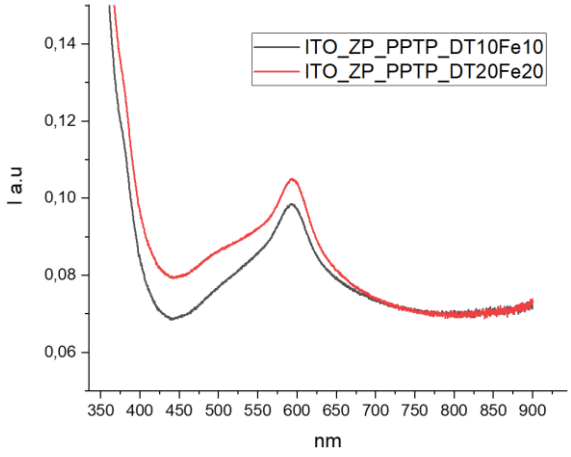

Figure 21 UV-Vis spectra of two DT-Fe multilayers assembled on ITO (10 nominal layers in black and 20 nominal layers in red).

The sample B (20 iterative cycles) show a higher MLCT signal intensity, due to the fact that an increased number of metal centers is present.

A subtraction of the two spectra, reported in Figure 22, highlights the increasing of MLCT adsorption band going from 10 to 20 iteration of assembling cycle procedure.

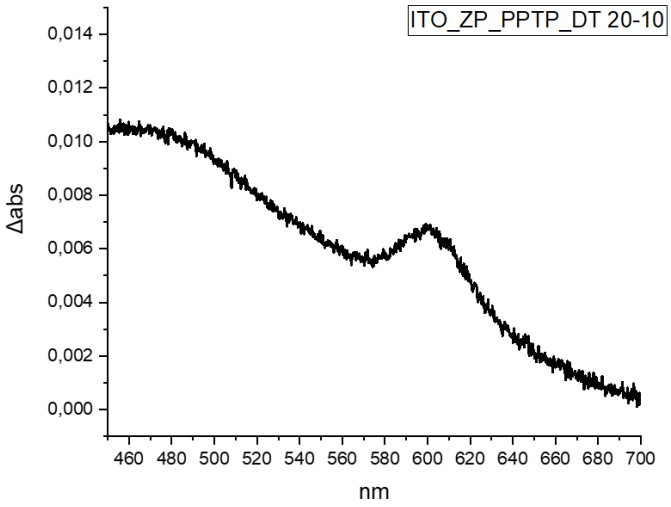

Figure 22 Difference of UV-Vis spectra of two different DT-Fe multilayers (20 nominal layers minus 10 nominal layers) assembled on ITO

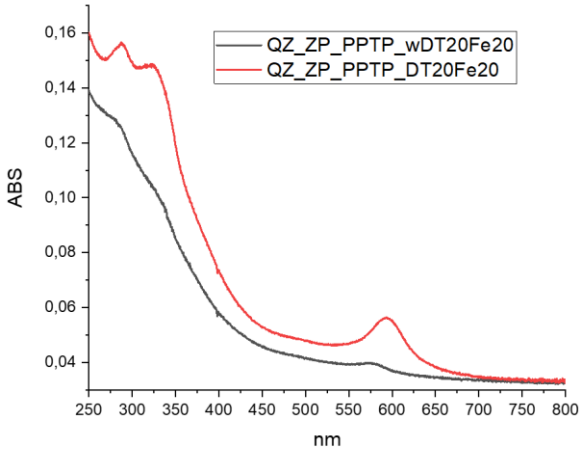

Figure 23 Overlay of UV-Vis spectra of DT-Fe (red line) and wDT-Fe (black line) architectures, both assembled on quartz with 20 iteration steps (20 nominal layers).

Figure 23 shows the overlayed UV-Vis spectra acquired on two systems built up with 20 Fe-DT (red line) and 20 Fe-wDT (black line) iterative reaction cycles, both on quartz substrates. The spectra show the presence of the MLCT band in both the samples (see also the zoom reported in Figure 24), but with a slight difference in the peak position (593.6 for the Fe-DT system and 576.2 for the Fe-wDT), similar to that observed for the complexes in solution. Although the two samples have been prepared carrying out the same number of iterative processes, the MLCT absorption intensities are different, with a quite stronger adsorption for the Fe-DT system. A different shape of the spectrum in the UV region for the two systems is confirmed, with two resolved peaks in the Fe-DT system and a much less resolved structure in wDT-Fe .

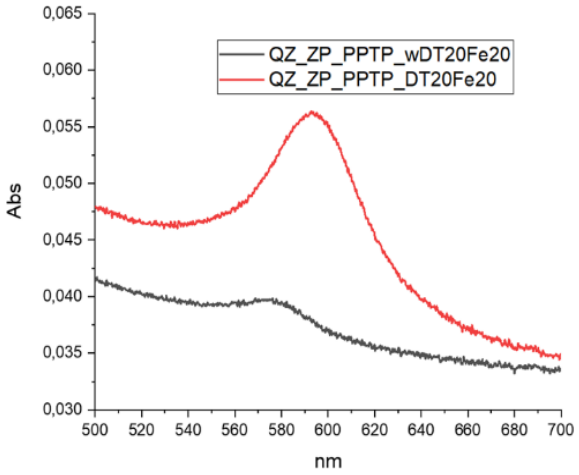

Figure 24 Overlay zoom of UV-Vis in MLCT spectra range related to DT-Fe 20 nominal layers assembled on quartz (red line) and wDT-Fe 20 nominal layers assembled on quartz (black line)

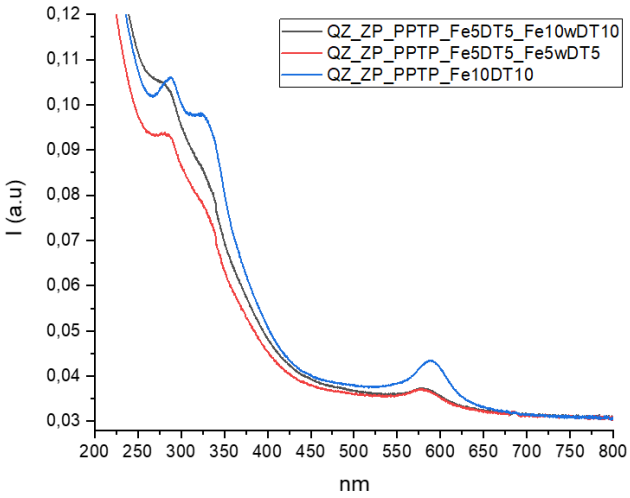

Figure 25 Overlay of UV-Vis spectra related to: DT-Fe 10 nominal layers assembled on quartz (blue line), UV-Vis spectra related to DT-Fe 5 nominal layers plus wDT-Fe 5 nominal layers assembled the same quartz substrate (red line), UV-Vis spectra related to DT-Fe 5 nominal layers plus wDT-Fe 10 nominal layers assembled the same quartz substrate (black line)

In order to get a deeper insight on the behavior of the two systems, some experiments were carried out, where the growth of the supramolecular architecture was done by alternating sequences of growth cycles with FeDT and FewDT. In figure 25 the UV-Vis absorption spectra relative to some of these "composite" systems are compared: a sample constituted by 10 FeDT layers, one composed of 5 FeDT and 5 wDT layers and another composed of 5 FeDT and 10 wDT layers. Figure 26 reports, enlarged, only the region of MLCT transition. Probably the most striking observation from these figures is that, although the MLCT band is present in the three spectra, its intensity seems not to be related to the number of metallic centers expected from the number of coordination cycles. A closer observation shows that the intensity of the band for $(DT\text{-}Fe)_5$-$(DT\text{-}Fe)_5$ system is the same of that of the $(DT\text{-}Fe)_5$-$(wDT\text{-}Fe)_{10}$ system, while in the spectrum of $(DT\text{-}Fe)_{10}$ its intensity is approximately double.

We can observe also that the band shape in the UV region for the mixed samples is a convolution of those observed in the systems prepared a single type of ligand.

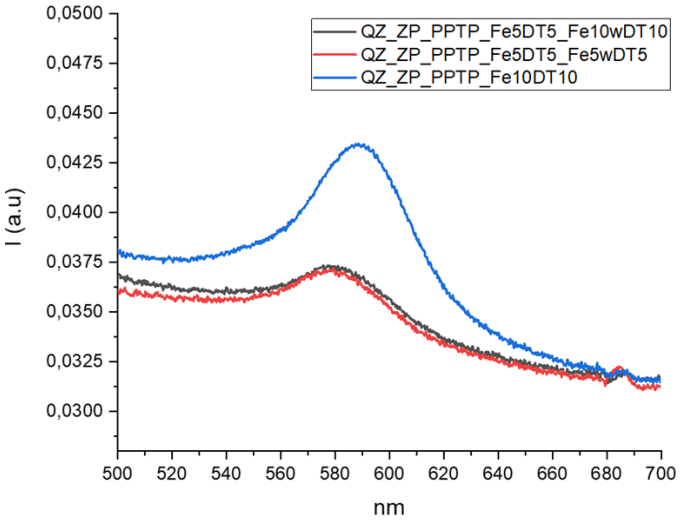

Figure 26 Overlay zoom in MLCT region of UV-Vis spectra related to: DT-Fe 10 nominal layers assembled on quartz (blu line), UV-Vis spectra related to DT-Fe 5 nominal layers plus wDT-Fe 5 nominal layers assembled the same quartz substrate (red line), UV-Vis spectra related to DT-Fe 5 nominal layers plus wDT-Fe 10 nominal layers assembled the same quartz substrate (black line).

Finally, the table 1 reports the position the MLCT peaks for a series of different systems, either in solution or assembled on a solid substrate, showing, as expected, that small shifts can be observed, in similar systems, when changing the chemical environment (solvent and aggregation state).

Sample	Absorption peak(nm)
DTFe chloroform/alcohol/water	588
wDTFe chloroform/alcohol/water	568
ITO wDT_7Fe_7	579
ITO $wDT_{21}Fe_{21}$	579
ITO $DT_{10}Fe_{10}$	593,8
ITO $DT_{20}Fe_{20}$	593,8
Quartz $DT_{20}Fe_{20}$	593,6
Quartz $wDT_{20}Fe_{20}$	576,2
Quartz $Fe_5DT_5Fe_5wDT_5$	581
Quartz $Fe_5DT_5Fe_{10}wDT_{10}$	581
Quartz $Fe_{10}DT_{10}$	588,6

Table 1 Characteristic MLCT for different complexes based on Fe-DT and bansed on Fe-wDT, in liquid solution or assembled on different solid substrates.

7.3 ToF-SIMS characterization of Fe-DT and Fe-wDT -based molecular wires.

The molecular wires were characterized by Tof-SIMS. For comparison purposes, we studied also the ToF-SIMS spectra of the two molecular building blocks DT and wDT, as well as of the Fe(II) complexes of these ligands formed in solution and precipitated on a non-reactive substrate. In the case of the two ligands, a few microliters of a diluted solution of each compound (DT, wDT) were deposited on silicon substrates, allowing the solvent to evaporate, leaving an ultrathin layer of the compound film on the silicon surface[123].

Figure 27 shows the spectrum region relative to DT molecular ion $C_{36}H_{25}N_6^+$, at m/z = 541.2 u).

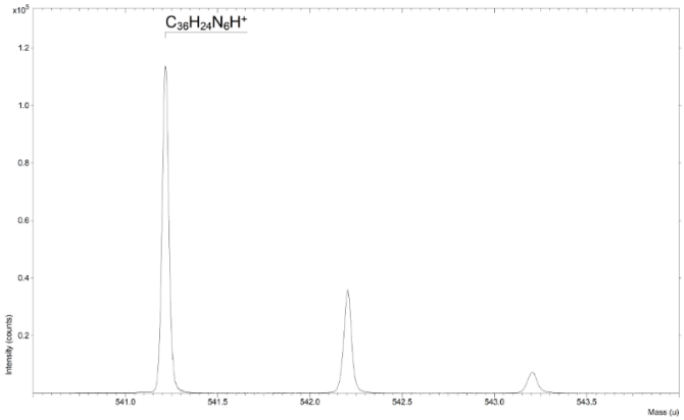

Figure 27 Isotopic distribution of DT molecular ion $C_{36}H_{25}N_6$+

Figure 28 shows the spectrum region relative to the molecular ion signal of wDT molecule $C_{37}H_{27}N_6^+$ at 555.2 u.

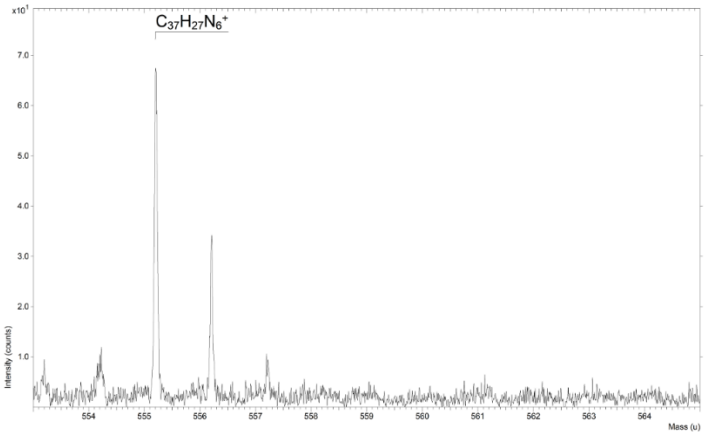

Figure 28 Isotopic distribution of wDT molecular ion $C_{37}H_{27}N_6^+$

As to the complexes of the two ligands with iron (II), not anchored on the surface but just deposited on it from a solution, we devised the following procedure: 1 ml of a $1x10^{-4}$ M freshly prepared solution of $FeSO_4$ in H_2O:EtOH (50:50) was added to 5 ml of a $5x10^{-4}$ M solution of the ligand in chloroform. This two-phase system was energically agitated and the presence of a blue-violet coloration indicated the formation of the complex in the chloroform phase. Few microliters of the coloured solution were deposited on silicon allowing the solvent to evaporate, leaving an ultrathin layer of Fe-DT and Fe-wDT complexes on the silicon surface. Figure 29 shows the region of the positive SIMS spectrum of Fe-DT with the isotopic distribution corresponding to $C_{36}H_{24}N_6Fe^+$ ion (596.2 u), i.e. the minimum unit expected from the coordination reaction.

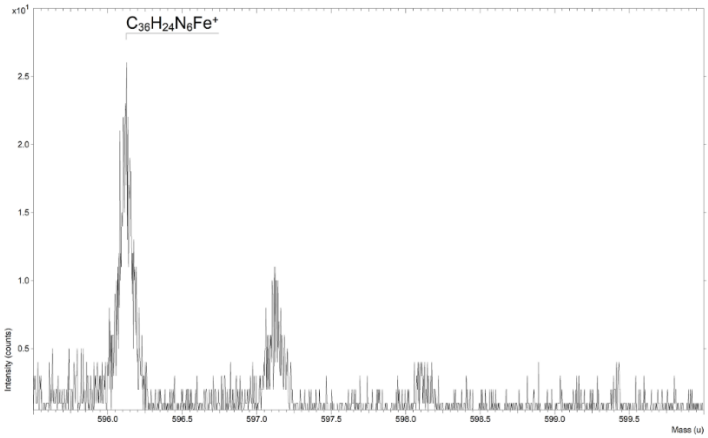

Figure 29 Isotopic distribution of Fe-DT $C_{36}H_{24}N_6Fe^+$ ion

Figures 30 and 31show two different portions of the same spectrum obtained from the Fe-wDT system. In is possible to identify respectively the isotopic distribution of the molecular ion $C_{37}H_{26}N_6Fe^+$ (around 610.2 u) and the isotopic distribution of the molecular ion $C_{37}H_{27}N_6^+$ (around 555.2 u).

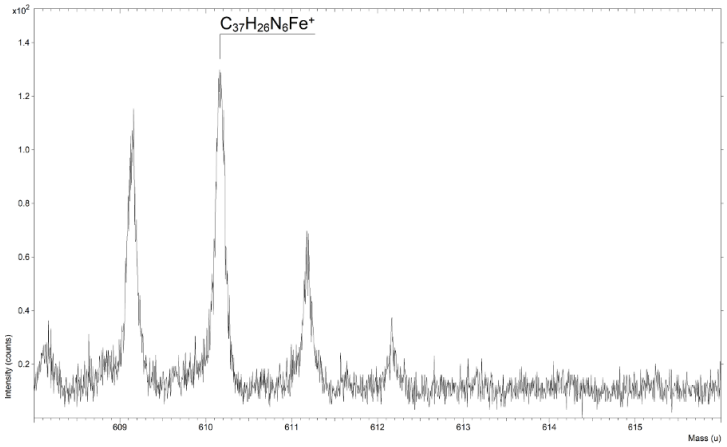

Figure 30 Isotopic distribution of Fe-wDT $C_{37}H_{26}N_6Fe^+$ ion in the spectrum of Fe-wDT system.

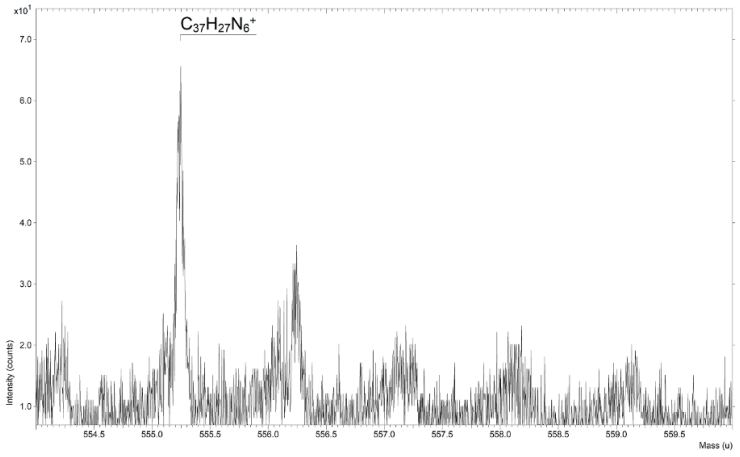

Figure 31 Isotopic distribution of wDT ligand $C_{37}H_{27}N_6^+$ in the spectrum of Fe-wDT system.

For studying the molecular wires anchored at oxide surfaces by the stepwise procedure previously described, and at the same time to avoid instrumental issues

induced by surface electrostatic charging during ToF-SIMS analysis of molecular wires anchored on insulating quartz substrates, a set of samples was prepared by assembling the molecular wires on silicon substrates that, having a thin layer of native oxide on the surface, are suitable for ZP priming, formation of the PPTP SAM platform and stepwise construction of the Fe-DT or Fe-wDT molecular wires, i.e. with the same procedure we've already used for glass, ITO or quartz substrates

Figure 32 and figure 33 show the regions of the ToF-SIMS spectrum in which it is possible to identify, from mass and isotopic distribution, the presence of $C_{36}H_{24}N_6Fe^+$ ion (596.2 u) and, at higher masses, of $C_{36}H_{24}N_6Fe_2OCl^+$ (703.1 u) ion, both attributable to the presence of FeDT complexes.

The same spectrum (figure 34) shows the presence of $C_{36}H_{24}N_6FeCl^+$ (631.1 u), the minimum complex unit including its counter-ion Cl^-.

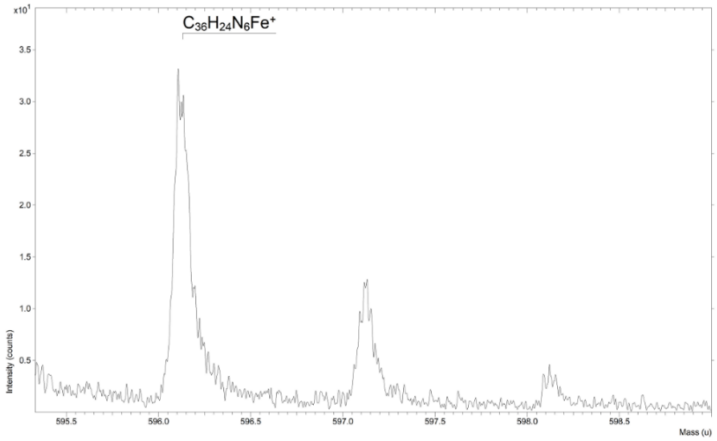

Figure 32 signals distribution of Fe-DT based assembled molecular wires associated fragment $C_{36}H_{24}N_6Fe^+$

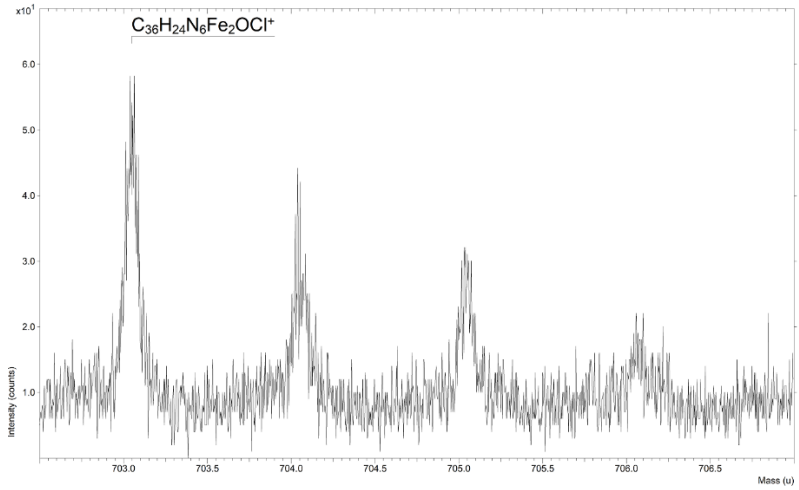

Figure 33 signals distribution of Fe-DT based assembled molecular wires associated fragment $C_{36}H_{24}N_6Fe_2OCl+$

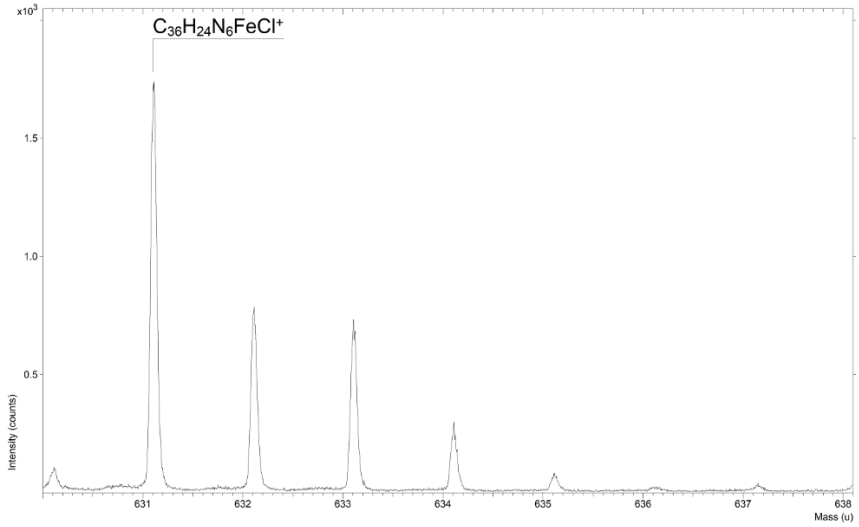

Figure 34 signals distribution of Fe-DT based assembled molecular wires associated fragment $C_{36}H_{24}N_6FeCl+$

Figure 35 shows a part of the spectrum with the fragment $C_{37}H_{25}N_6Fe^+$ (609.1 u), again identified with the help of isotopic distribution, obtained from a sample prepared on quartz, in which the assembling procedure had been iterated 20 times by using wDT.

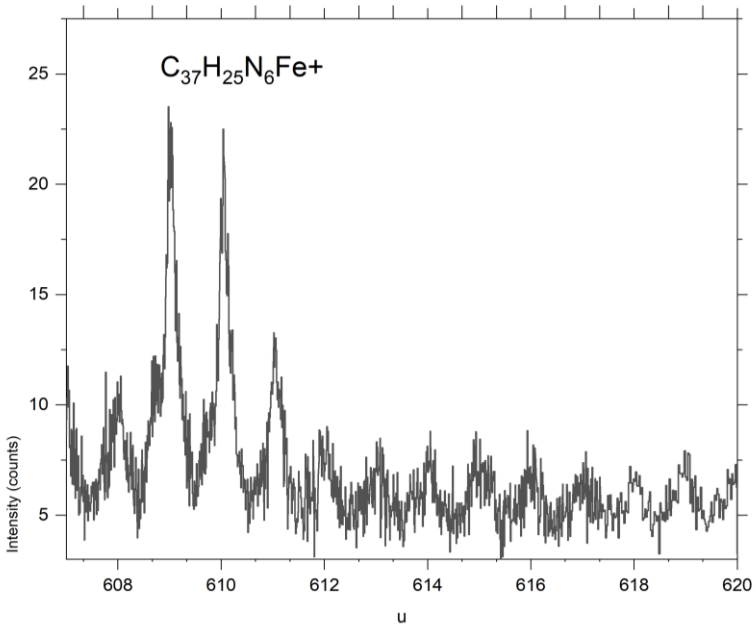

Figure 35 signals distribution of Fe-wDT based assembled molecular wires associated fragment $C_{37}H_{25}N_6FeCl^+$

7.4 Discussion and conclusions

This part of the work was focused on the study and development of molecular wire assembly strategies on the surfaces of different substrates such as quartz, silicon, and ITO.

The molecular wires were made using different molecular systems with terpyridine functionalities (DT and wDT) as building-blocks using the Fe^{2+} ion as the coordinating ion. To allow the anchoring of these distinct multilayer molecular structures, a preliminary functionalization of the substrates was carried out using priming methods together with the formation of a self-assembled monolayer of a phosphonic acid. More precisely, the surface of oxides used as substrates has been modified by creating a monolayer of zirconium phosphate according to the method indicated as ZP priming. This preliminary modification allowed first the anchoring of a self-assembled molecular film of 4-(2,2':6',2"-terpiridin-4-yl)

benzenephosphonic acid (PPTP) which, thanks to the coordinating capacities of the terpyridine functions, made possible the following assembly of the building blocks. (DT and wDT).

The characterization of the self assembled system was carried out by UV-Vis spectroscopy and Time-of-Flight Secondary Ions Mass Spectrometry.

UV-Vis spectroscopy allowed us to study the electronic transitions associated with the single building blocks, the related metal-organic complexes in the liquid phase and the molecular wire assembled on solid substrates. The formation of the supramolecular architectures is demonstrated by the presence of the metal-to-ligand charge transfer band (MLCT). A first information supplied by the UV-Visible spectra is that the length of the molecular wire does not affect significantly the electronic properties of the individual metal-centred units. Also, the measurements on the mixed-ligand wires suggest that the formation of wires with the “bent” wDT ditopic ligand is more difficult than in the case of the linear ditopic ligand DT.

Further information on the formation of the metalorganic wire structures was obtained from ToF-SIMS measurements.
In particular, secondary ion spectra of the systems assembled at the surface using DT as a building block, show the presence of peaks indicating the formation of the DT-Fe complex. Similar diagnostic peaks are present on the samples where the assembly procedure was performed by using wDT. Although UV-Vis spectra suggest that it happens in a less efficient way, the presence of these peaks suggests that coordination structures wDT-Fe are formed at the surface. This finding indicates the possibility of using this new molecular structure (Fe-wDT) in the functionalization of solid surfaces with metalorganic structures. This could be of some interest especially when it is necessary to create systems in which it is useful to introduce a certain degree of "disorder" in the structure of the organometallic film, exploiting the bent structure of wDT.

8 ASSEMBLY AND CHARACTERIZATION OF MIXED Fe (II) / Ru (II) POLYTERPYRIDINE–BASED MOLECULAR WIRES.

This chapter is focused on the development of experimental procedures aimed to the preparation of three-dimensional supramolecular architectures based on the growth of Ru and Fe metal organic terpyridine complexes anchored on oxide surfaces. The assemblies of molecular wires prepared with a layer-by-layer assembly procedure, could be seen as multilayer structures where the word "layer" is assimilated to a new assembly of metal centers and terpyridine ligand.

The potential of polymetallic molecular wire anchored on gold, in which the same unit $M(Tpy)_2$ (typically M = Fe, or Co) is repeated n times, has been explored already in the laboratory where this thesis work was conducted. Such systems show remarkable conduction properties[124]. During this work, attention was focused on the preparation and characterization of new wire types in which metal centers of Ru (II) and Fe (II) alternate with different sequences. The study of this type of systems turns out to be almost completely unexplored. Therefore, investigating the physico-chemical properties of the single new building blocks as well as the characteristics of the corresponding molecular wire on interesting substrates represents a basic study for application in the field of devices where molecular conduction and/or photoconduction is required, for example in optoelectronic devices.

As already mentioned, during the present Ph.D. work, the assembly and the physico-chemical properties of "multilayers" made from different mixed polyterpyridine complexes of Fe (II) and Ru (II) have been studied and characterized. These have been assembled to form molecular multilayers on surfaces of ITO, FTO, SiO_2 by exploiting an iterative complexation approach that employs the formation of the Fe-bis-terpyridine complex to increase the length of molecular wire by using pre-synthesized complexes containing a variable number of active Ru- centers.

8.1 Preparation of the molecular wires

In detail, a preliminary ZP priming procedure was used on the different surfaces, to allow the formation of a PPTP SAM (figure 36).

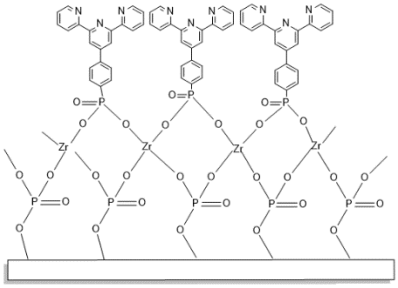

Figure 36 Schematic representation of a ZP primed substrate functionalized with a PPTP SAM exposing free terpyridine functionalities.

This first molecular layer exploits the phosphonic group to bind stably to the surface and its terpyridine functionality to allow the assembly mediated by the Fe (II) ion of different building blocks (which in our case will contain ruthenium centres). One of the advantages of this approach is to obtain, in a reproducible way, a platform always of the same type, substantially independently of the oxide used as substrate.

The ruthenium containing building blocks, which structure is reported in figure 37, synthesized by the research group of prof. G. Hanan of the University of Montreal, were the following:

Ru[4 ′, 4 ′ ′ ′ ′ - (1,4-phenylene) bis (2,2 ′: 6 ′, 2″terpyridine)]$_2^{2+}$

Ru_2[4 ′, 4 ′ ′ ′ ′ - (1,4-phenylene) bis (2,2 ′: 6 ′, 2″terpyridine)]$_3^{4+}$;

Ru_3[4 ′, 4 ′ ′ ′ ′ - (1,4-phenylene) bis (2,2 ′: 6 ′, 2″terpyridine)]$_4^{6+}$

all having PF_6^- anions as a counter-ions.

Hereinafter the above units, respectively containing 1, 2 or 3 Ru (II) centers, will be referred to as Ru1, Ru2 and Ru3,.

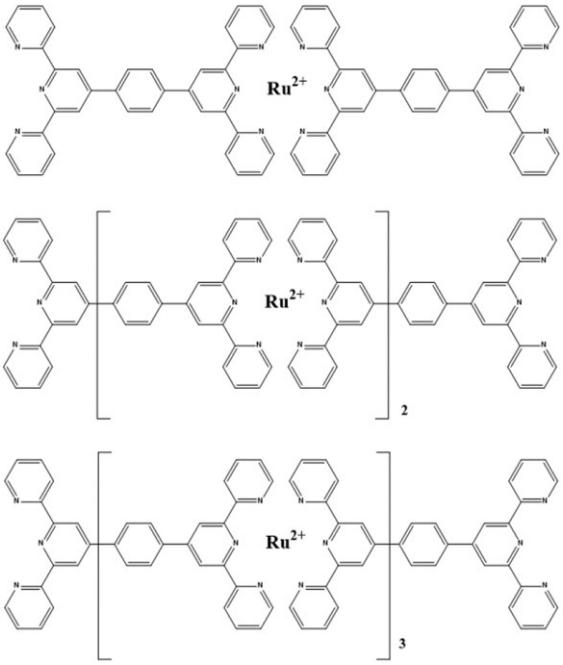

Figure 37 Molecular structures investigated as building blocks for molecular wire assembling process: from top respectively Ru1, Ru2, Ru3.

The terpyridine functionalities of PPTP SAM integrated into the surfaces of the different substrates represent the first molecular layer as well as an ideal chemical platform for the growth of molecular wire. These are obtained through a procedure, schematized in figure 38, which exploits the coordination of the Fe (II) ion and can be iterated several times since each addition of a Ru-containing building block (either Ru1, Ru2 or Ru3) leaves a free terpyridine at the new surface.

The full experimental procedure involves, after the preparation of the PPTP platform, i) 90 seconds immersion of the sample in a $FeSO_4 \cdot 7H_2O$ 10^{-4} M solution in a 1:1 water-ethanol mixture;

ii) successive rinsing first in water and then in DMF;

iii) immersion in a solution (10^{-5} M in DMF) of the molecular building blocks (Ru1, Ru2, or Ru3) for 30 minutes;

iv) repeated washing with DMF in order to remove any traces of physisorbed building blocks. Steps i-iv can be reiterated in order to increase the length of the wires.

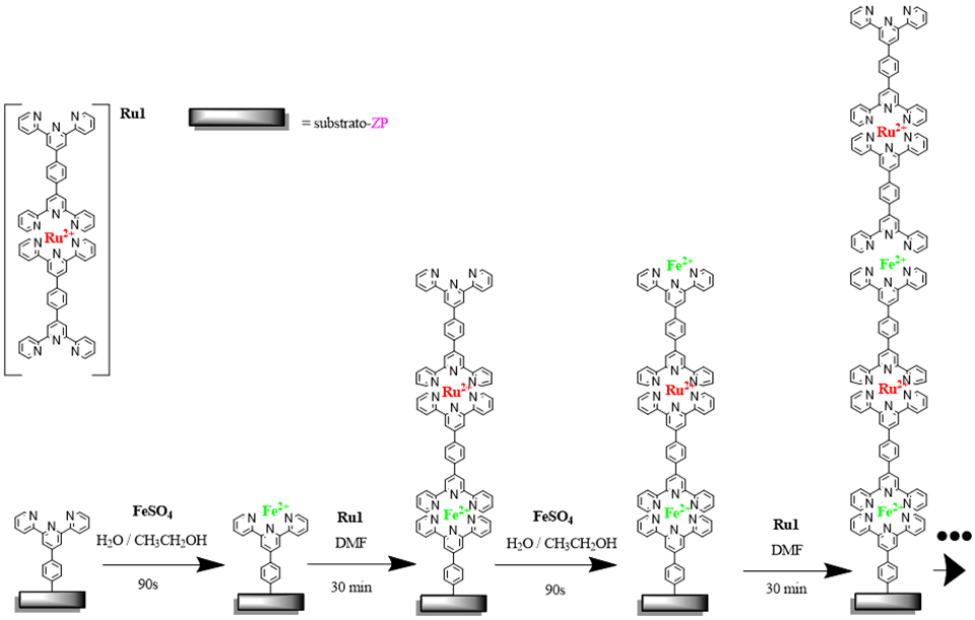

Figure 38 Scheme of the iterative procedure for obtaining a Fe/Ru1 based molecular wire.

8.2 Physico-chemical characterization of molecular wires

The self-assembled molecular wires, prepared as described in the previous section, were characterized by using UV-Vis absorption spectroscopy and time-of-flight secondary ion mass spectrometry (ToF-SIMS). These techniques were exploited to monitor the various steps of preparation such as ZP priming, of the PPTP anchoring on the oxide surface and the different stages of wire growth.

3.2.1 Characterization of building blocks and substrates: UV-Vis spectroscopy

The polynuclear complexes (Ru1, Ru2, Ru3) were characterized by UV-Vis absorption measurements. Since the growth of the molecular wire occurs through the formation of a bis (terpyridine) complex of iron II, the UV-Vis spectrum of the $[Fe(II)(Tpy)_2]^{2+}$ complex was also acquired for comparison purposes. The measurements were performed on ~ 10^{-5} M solution of the analytes in DMF.

The region of the MLCT transition of the photoactive center $[Ru(tpy)_2]^{2+}$ in the UV-Vis spectrum is shown in figure 39 for the three building blocks Ru1, Ru2 and Ru3. The shape of the band is very similar in the three spectra, and, in all three cases, the maximum absorption is at about 500 nm, indicating that within the polynuclear complexes Ru2 and Ru3 the different metal centers are not very interacting each other. Moving from mononuclear systems to the polynuclear ones, a small but significative red shift is observed (λmax (Ru1) = 499; (λmax (Ru2) = 508; (λmax (Ru3) = 510), which can be an indication of a weak "electronic communication" between contiguous metal centers.

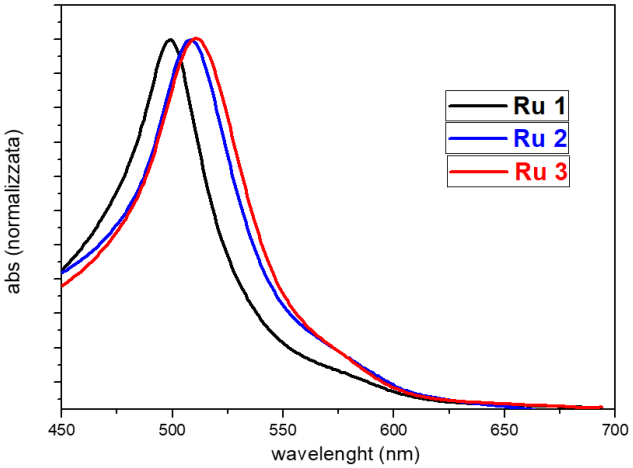

Figure 39 Overlay of MLCT regions of UV-Vis absorption spectrum of ruthenium based building blocks dissolved in DMF.

As mentioned, the absorption spectrum in solution of a system containing $[Fe(tpy)_2]^{2+}$ centers was also measured, to be used as a model for the similar Fe-tpy based centers present in the molecular wire assembled on the surfaces. For this purpose, the FeII-DT system has been prepared by reacting $FeSO_4 \cdot 7H_2O$ and 4′, 4″″-(1,4-phenylene) bis (2,2 ′: 6 ′, 2 ″ - terpyridine) in molar ratio approximately 1: 2 and measuring the spectrum without carrying out any purification. Since DT is a ditopic ligand and considering that the bis-terpyridine complex of Fe-$(Tpy)_2$ is largely favored over the mono-terpyridine (Fe-Tpy), it is expected that linear oligomers of various sizes, such as $FeDT_2$, $Fe_2(DT)_3$, $Fe_n(DT)_{n+1}$ are present in solution. In the absorption spectrum, shown in figure 40, the typical band is observed with a maximum at 572 nm, in agreement with what is reported in the literature for the MLCT transition of the $[Fe^{2+}(tpy)_2]^{2+}$ complex.

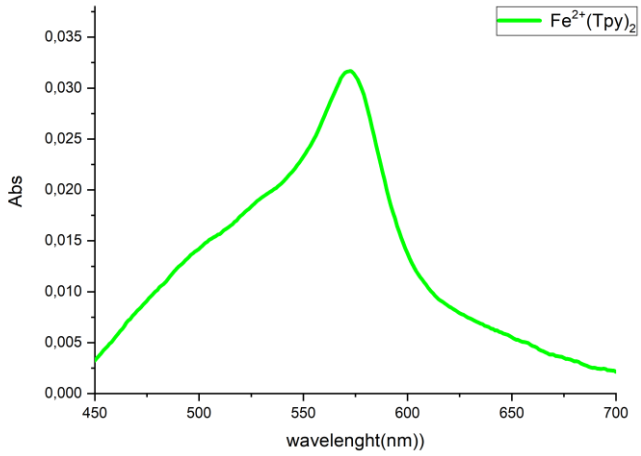

Figure 40 MLCT region of UV-Vis absorption spectrum acquired in hydroalcoholic solution of Iron bis terpyridine based metal organic complex

3.2.2 Characterization of building blocks and substrates: ToF-SIMS

The ToF-SIMS spectra of the non-anchored building blocks were studied. For this purpose, a fraction of monolayer of each of the compounds (Ru1, Ru2 and Ru3) was deposited on silicon surfaces, by evaporation of a few microliters of a dilute solution of the compound of interest, according to the proven procedure of "microsyringe deposition" [123].

Figure 41 shows some high mass regions of the positive ions ToF-SIMS spectrum. In particular we identify (figure 41a) the isotopic distribution of the ion $C_{36}H_{24}N_6Ru^{2+}$ (Ru - DT) around m/z 640, and those of higher mass species (fig.41b) assigned to $(C_{36}H_{24}N_6)_2Ru^+$ (m/z ~ 1180, $Ru(DT)_2$) and to its oxidized form $(C_{36}H_{24}N_6)_2RuO^+$ ($RuO(DT)_2$, m/z 1196).

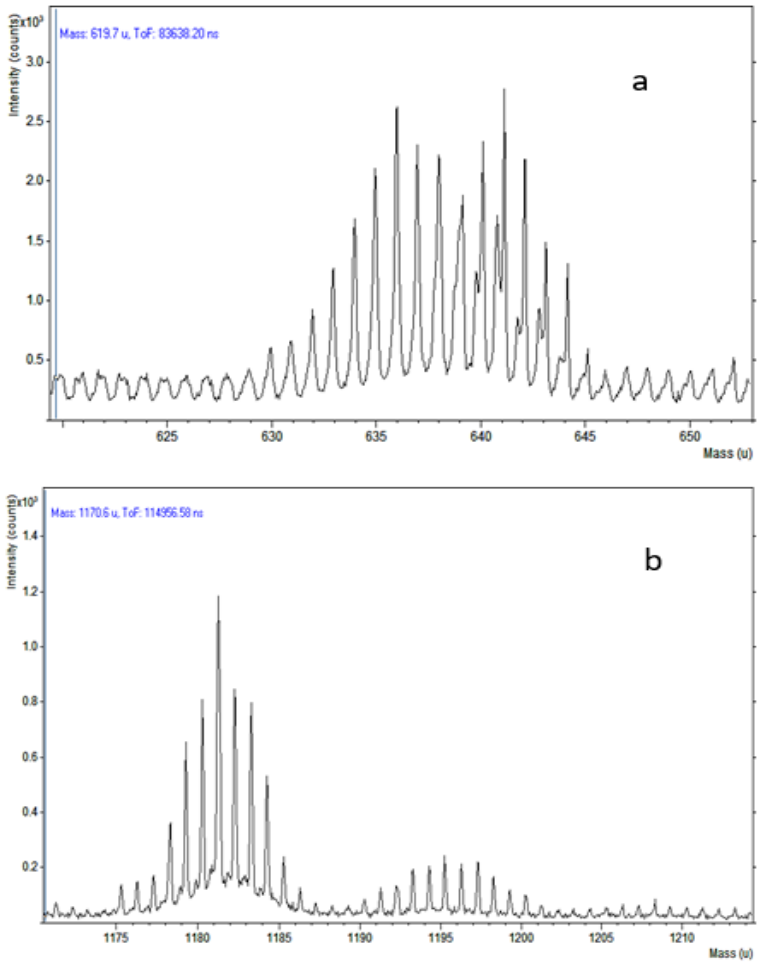

Figure 41(a-b) Isotopic distribution of the ion $C_{36}H_{24}N_6Ru_2$ + (Ru-DT) around m/z 640, (fig.41b) isotopic distribution assigned to $(C_{36}H_{24}N_6)_2Ru$+ (m/z ~ 1180, $Ru(DT)_2$) and to its oxidized form $(C_{36}H_{24}N_6)_2RuO$+ ($RuO(DT)_2$, m/z 1196).

The same species described above are also observed in the Tof-SIMS spectra of the bi- and tri-nuclear building blocks (Ru2 and Ru3). Furthermore, in the case of such compounds, some weak - but significant - signals are observed at higher masses, assigned to species containing more than one DT ligand and/or more Ru centers.

In particular, in the case of the Ru2 system, a peak around m/z 1825 assigned to the molecular ion $[(C_{36}H_{24}N_6)_3Ru_2]^+$ is detectable, although with very low intensity (Figure 42).

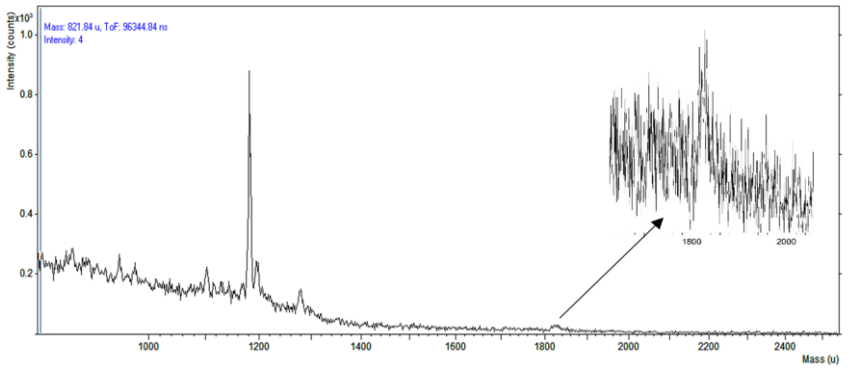

Figure 42 High mass range of ToF SIMS spectra of Ru2 building block deposited on silicon.

In the spectrum of Ru3 the molecular ion (m/z 2463) is not observed, presumably because the low detection efficiency, which tends to decrease at high masses.

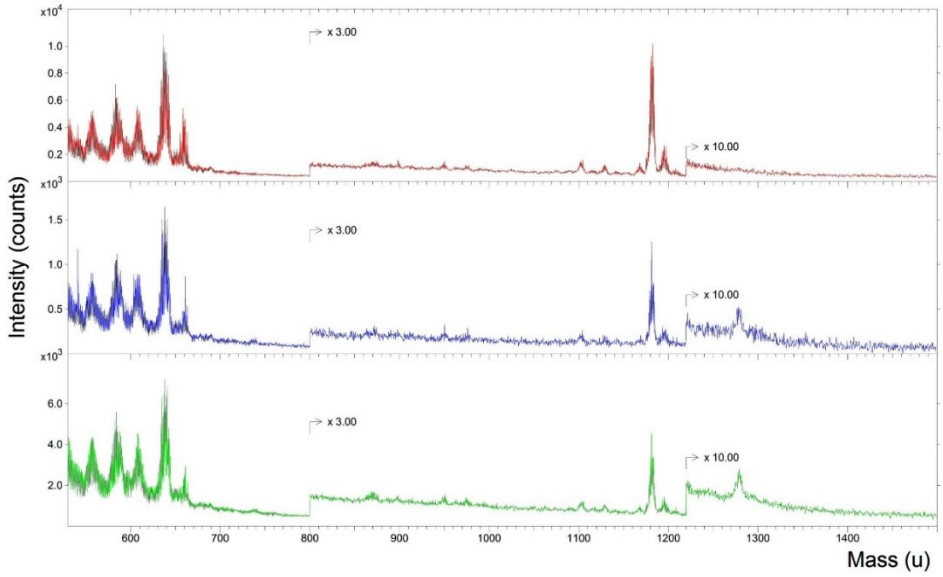

Figure 43 Comparison of the ToF-SIMS spectra of Ru1 (red line), Ru2 (blue line) and Ru3 (green line), all of them deposited on silicon as (sub)monolayers.

Furthermore, by comparing, for the three compounds, the region between 1000 and 2000 mass units (Figure 43), we observed that the species $[(C_{36}H_{24}N_6)_2Ru_2]^+$ at m/z ~ 1280 is present, albeit with different intensities, only in the spectra of the Ru2 and Ru3 systems. This in not unexpected, since such signal can come from the

fragmentation of bi- or tri-nuclear systems but not, obviously, from the mononuclear one.

3.2.3 Monitoring of the growth of molecular wires:UV-Vis spectroscopy

Figure 44 shows the absorption spectra of molecular wires of different length (from 1 to 5 Ru 1 centers) grown on FTO, along with the spectrum of the starting PPTP on ZP primed FTO on which the wires were grown.

Two MLCT bands at ~ 500 nm and ~ 580 nm, assigned to Ru $(DT)_2$ and Fe $(DT)_2$ units respectively, can be observed . The intensities of these bands increase as the number of growth steps increases, as can be seen from Figure 45. Furthermore, a linear correlation is observed between the increase in intensity for the MLCT bands and the number of deposited layers of Ru1 linked through Fe^{++}. As expected from 1:1 stoichiometry, the intensities of the two bands grow approximately parallel, thus demonstrating that one Ru1 unit is incorporated for each incorporated Fe ion.

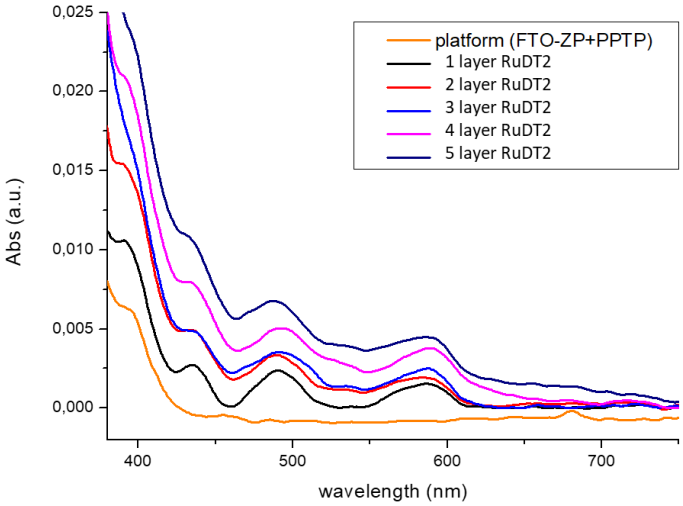

Figure 44 UV-Vis absorption spectra of molecular wires of different length (from 1 to 5 Ru1 centers) grown on FTO

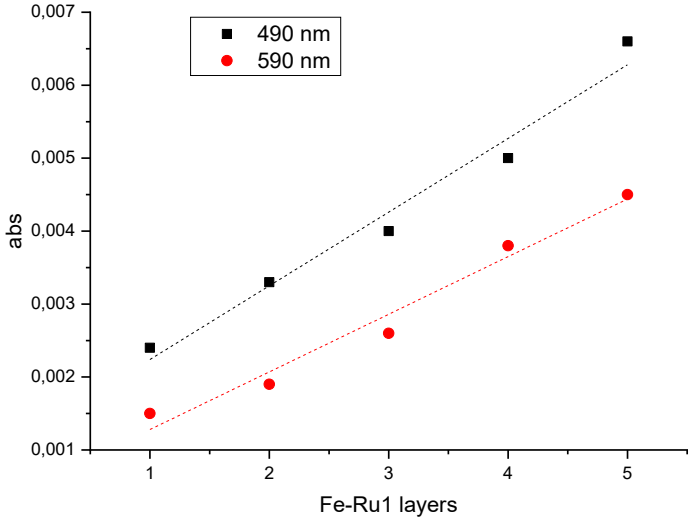

Figure 45 Linear correlation observed between intensity of the MLCT bands and the number of deposited layers of Ru1 linked via Fe^{2+} on FTO substrate.

Figure 46 shows the absorption spectra of 4 different-lenght samples in which the Ru2 system was grown on ITO (again using the ZP-priming procedure). The absorption spectra of the PPTP "platform" already coordinated with an Fe ion (ITO_ZP_PPTP (Fe)) are shown, as well as the spectra of wires obtained after the addition of 1, 4 and 6 layers of Ru2 building block.

Once again, the linear increase in intensity of the two MLCT bands of the two photoactive centers M $(tpy)_2$ indicates that the strands have grown. If the intensity of these bands is plotted as a function of the number of added layers, (Figure 47) it can be seen that the MLCT band associated with $[Ru(Tpy)_2]^{2+}$ (510 nm) grows with a greater slope than in that relating to the center $[Fe(Tpy)_2]^{2+}$ (580 nm), as expected from the fact that the growth of each layer ideally involves the addition of two Ru units and a single Fe unit.

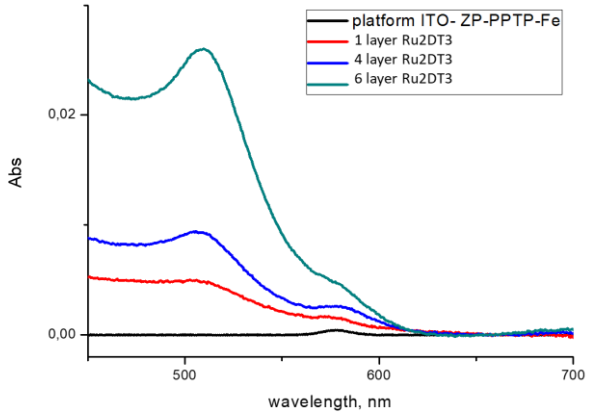

Figure 46 UV-Vis absorption spectra of molecular wires of different length (1layer, 4 layer,6 layer of Ru2 assembled units) grown on ITO substrate

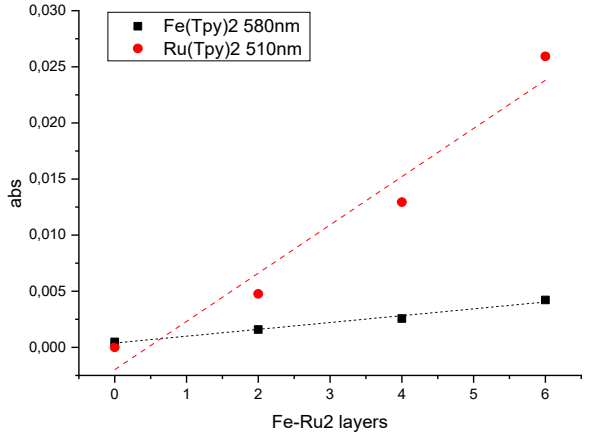

Figure 47 linear correlation observed between intensity of the MLCT bands and the number of deposited layers of Ru2 linked via Fe^{2+} on ITO substrate

The growth of the Ru2-based system has been studied not only on FTO and ITO, but also on silicon dioxide (quartz). Figure 48 shows the absorption spectra of 4 different lengths of Ru2-based wires. Also in this case there is a linear increase with different

slopes for the characteristic bands of the two types of metal center present in the system (Figure 49).

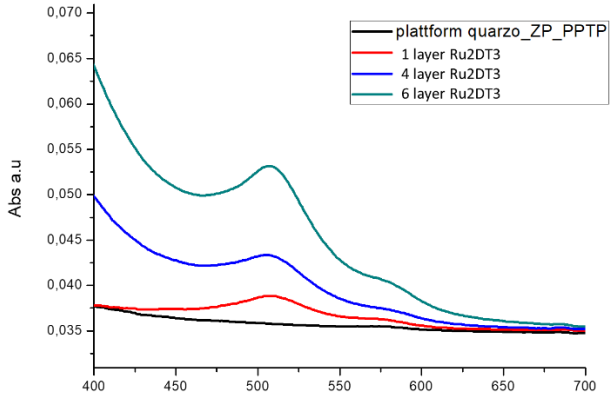

Figure 48 UV-Vis absorption spectra of molecular wires of different length (1layer, 4 layer,6 layer of Ru2 assembled units) grown on quartz substrate

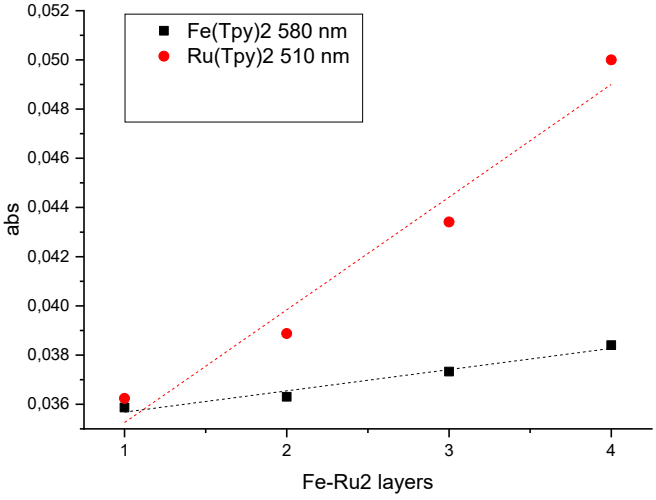

Figure 49 linear correlation observed between intensity of the MLCT bands and the number of deposited layers of Ru2 linked via Fe^{2+} on quartz substrate

Finally, some preliminary experiments have been carried out on the growth of functional molecules by using the Ru3 system on ZP primed indium tin oxide (ITO) substrate. Such experiments indicate that the ZP functionalization methodology and subsequent wire growth can be successfully used also in the case of such systems. Figure 50 shows the UV-Vis spectrum of a sample on which 10 layers have been grown, corresponding to a molecular wire with a length of about 40 nm. It should be noted that, although in this case the growth kinetics was not monitored, in the final system the ratio between the intensity of the bands at ~ 500 nm and ~ 580 nm is equal to 3: 1 in agreement with the predicted growth stoichiometry.

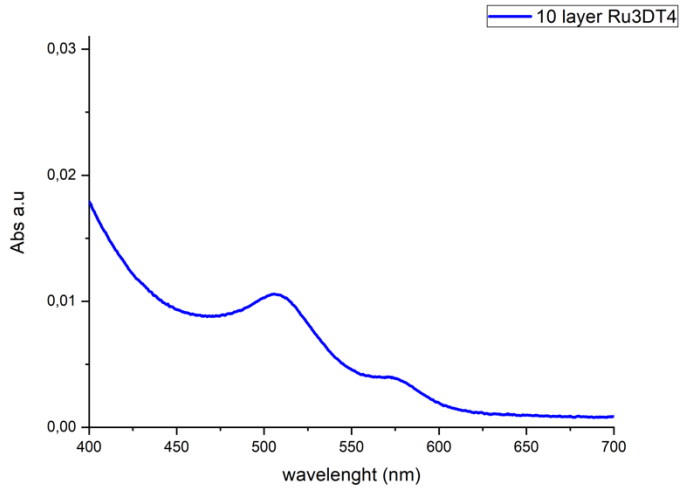

Figure 50 UV-Vis absorption spectra of molecular wires (10 layer of Ru3 assembled units) grown on quartz substrate

3.2.4 ToF-SIMS characterization of anchored molecular wires

ToF-SIMS characterization was carried out on molecular wires assebled by using the three building blocks Ru1, Ru2 and Ru3. The self assembling process has been applied on silicon substrates with their native oxide, which is known to form a uniform layer with a thickness of 1-2 nm[125]. As in the other cases, the silicon substrates were exposed to the standard ZP priming process and functionalization with PPTP, followed by the growth of metal-terpyridine complexes. The use of ultrathin silicon oxide on silicon substrates avoids the surface charge compensation issues that occur on highly insulating substrates, such as quartz, during SIMS measurements.

Figure 51 shows ToF-SIMS spectra of Ru1, Ru2, Ru3 monolayers. A signal at m/z 640, assigned to $C_{36}H_{24}N_6Ru^+$ (Ru-DT) ion, is clearly visible in all the three analyzed samples, confirming the presence of the building block on the surface.

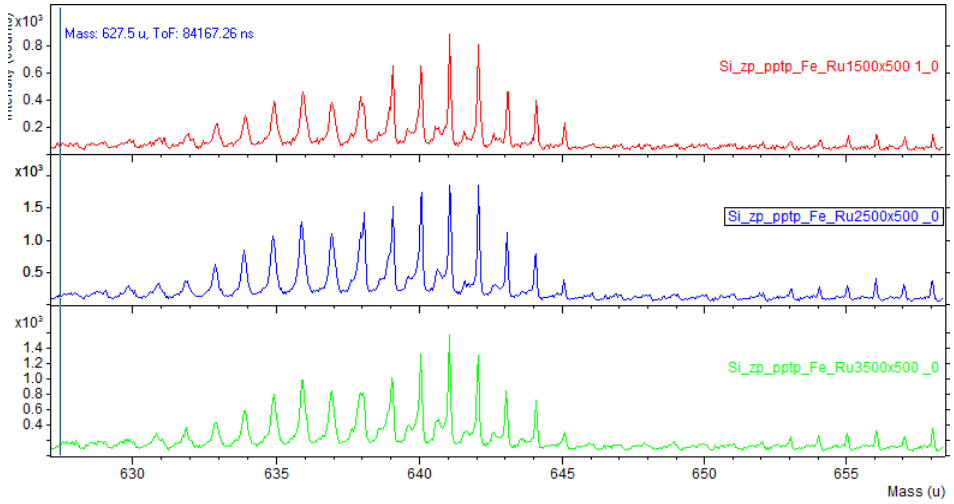

Figure 51 $C_{36}H_{24}N_6Ru+$ (Ru-DT) isotopic mass distribution recorded by means of ToF-SIMS static measurement from monolayers assembled with Ru1 (red line), Ru2 (blue line) and Ru3 (green line). Each of them is anchored on ZP-PPTP primed SiO_2.

Comparing the spectrum region ranging from m/z 1100 u to m/z 1400 u, (Figure 52) it can be observed that, the signal attributable to the Ru2-DT_2 fragment ($[(C_{36}H_{24}N_6)_2(Ru)_2]^+$ at 1280 u) is detected in the samples based on Ru2 and Ru3 units, while it is not present in the Ru1 sample. As already observed in paragraph 3.2.2, this can be explained by the fact that the structure corresponding to the ion at ~ 1280 u is not present in the Ru1 block, while in the case of Ru2 and Ru3 it comes from the fragmentation of the block.

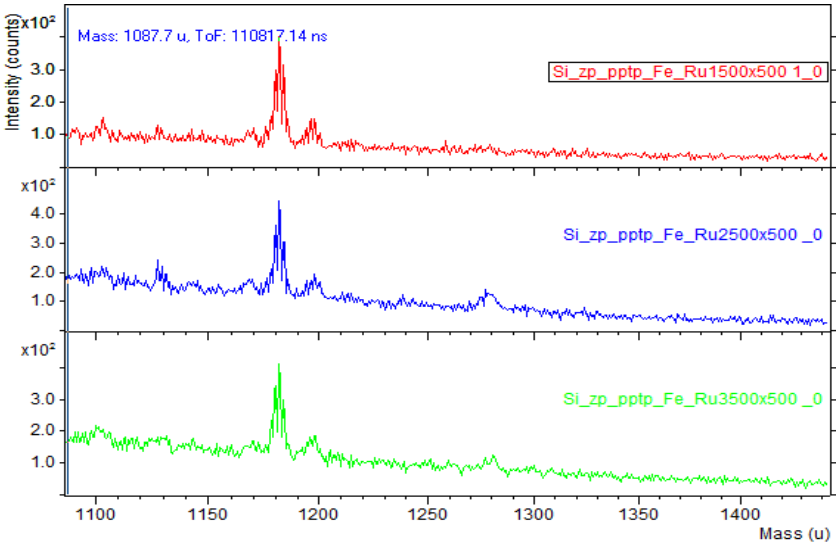

Figure 52 High masses portion of ToF-SIMS static spectra recoded from monolayers assembled with Ru1 (red line), Ru2 (blu line), Ru3 (green line) each of them anchored on ZP-PPTP primed SiO_2 substrates. The isotopic mass distributions of Ru_2-DT_2 ($[(C_{36}H_{24}N_6)_2(Ru)_2]$)$^+$ at ~1280 u is detectable only in Ru2 and Ru3 based monolayers.

Longer molecular wires, with different numbers of building blocks, were prepared and analyzed by means of ToF-SIMS. From a qualitative point of view, the spectra obtained from long wires are very similar to those acquired from the monolayers. This is due to the small sampling depth of the ToF-SIMS technique, which is sensitive to the uppermost surface atomic layers. As a typical example, in Figure 53 ir reported the ToF-SIMS spectrum of a 10-layer system assembled by using Ru2 as building block. The spectra of the 2-, and 7-layer systems are virtually identical.

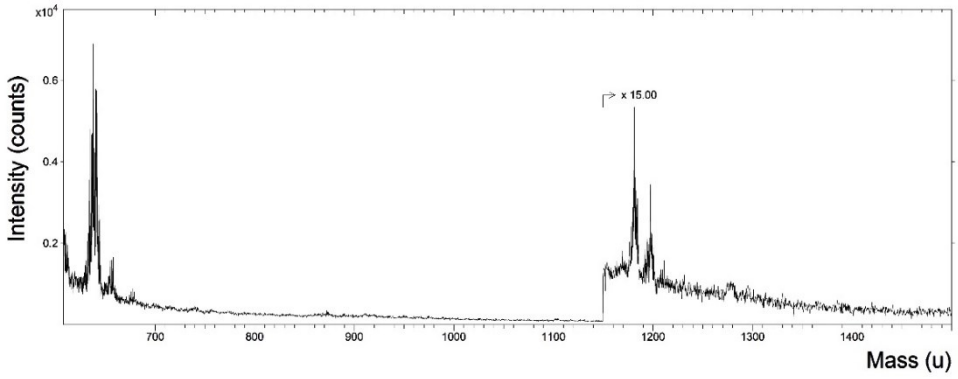

Figure 53 ToF-SIMS spectra overview related to 10 nominal layer of system assembled on silicon substrate by using Ru2

8.3 Conclusions

In the context of the general theme concerning the build-up of systems suitable for molecular electronics and optoelectronics, the integration of molecular and supramolecular systems on solid surfaces such as transparent oxides, including transparent conductive oxides (TCO), of ultra-thin films composed by assemblies of "molecular wire" based on mixed Fe(II) and Ru(II) polyterpiridine complexes have been carried out. Self-assembling technique allowed us to obtain ultrathin molecular layers of increasing thickness as the number of metal centers in the wire increases. From a different point of view, which also recalls the stepwise assembly preparation methodology adopted, these films can be considered as multilayers in which organic units (a terpyridine-based ditopic binder) and divalent metal centers (iron and ruthenium) alternate. In particular, we built up molecular wires in which one, two or three consecutive Ru(II) centers alternate to an Fe(II) center. This was possible by adopting an assembly strategy that uses preformed building blocks containing the Ru^{++} centers by connecting them together, with reactions carried out directly at the solid surface, with formation of an iron bisterpyridine complex. The molecular wires were assembled on the surfaces of different oxides (SiO_2, ITO, FTO), previously functionalized in such a way as to form a binding "platform" which exposes free terpyridine functions to the surface.

The systems thus prepared were studied by UV-Vis spectroscopy and secondary ion mass spectrometry. The data obtained from these techniques confirm the formation and growth of the molecular wires on the surfaces of the considered oxides. One of the important aims of the project is to characterize the electron transport properties of the wires, possibly under exposure to light, considering the presence of photoactive ruthenium centers, that candidate these systems as components of

optoelectronic devices. This requires the development of experimental methodologies that will be described in a following chapter, and some results will be presented in the case of systems in which the iron and ruthenium centers alternate with a 1: 1 sequence. Since this kind of measurements are best performed on wires of relatively short length, it is also important to follow the early stage of growth of the wires, in a range where it cannot be followed, with enough sensitivity, by measuring the absorbance of the wire. This is one of the reasons that prompted us to study, in parallel with the studies on oxide substrates, the anchoring of the mixed molecular wires on ultrathin gold substrates that, among others, allow the measurement of the initial growth of the wires by measuring the shift of gold surface plasmon absorbtion[124].

8.4 Physico-Chemical properties of molecular wires based on ruthenium and iron assembled on nanostructured gold surfaces

UV-Vis spectroscopy was used as a functional technique for evaluating the ability of the stepwise procedure to bind the two different molecular units that constitute the molecular wire on semitransparent gold surfaces and on oxide surfaces. The semi-transparent gold surfaces were made by depositing 20 nm of gold on quartz surfaces via sputter deposition process, then exposed to a UV-ozone treatment to remove any organic contaminants from the previous sputter process. The nanometric gold surface was functionalized with a SAM using a mix of MB / MPTP thiols known to have a high affinity and a high self-organization capability on gold surfaces. To obtain this molecular monolayer the experimental procedure involves the immersion for 24 hours of the surfaces of the semi-transparent substrates in 50 ml of an equimolar alcoholic solution of MB / MPTP 10^{-4} M.

In this phase, UV-Vis spectroscopic investigations were carried out in transmission modality using a Varian 750 instrument to identify the wavelength of the plasmonic peak of the functionalized nanometric gold surfaces. MWs's grow stepwise procedures were iterated on these substrates using in one case the bisterpyridine functional unit with the two ruthenium-based metal centers Ru_2DT_3 and in another case the bis-terpyridine unit DT functional to the growth of molecular wire based exclusively on Fe(II) metal centers.

Specifically, the substrates of semi-transparent nanometric gold after the preliminary step of functionalization by mixture of thiols MB/MPTP, are immersed in a solution of iron sulphate heptahydrate 10^{-4} M alcohol / water 1:1, in this step the coordination reaction of Fe (II) with the free terpyridine functionalities take place on the gold surface. Subsequently the substrates are moved into a solution of DT 10^{-4}M / chloroform in case it is desired to proceed with the assembly of MWs based on Fe(II) metal centers or, symmetrically in the case of growth of MWs based on ruthenium(II) metal centers, substrates will be immersed in a 10^{-4} M solution of pre-assembled Ru_2DT_3 units.

These assembly cycles were repeated 2, 4, or 6 times on two different sets each composed of three semi-transparent nanometer gold substrates on quartz functionalized with the SAM mix (QZ_Au_MB/MPTP). One of the two sets was used to iterate 2, 4, 6 times the growth steps of Fe/Ru_2DT_3-based MWs, the other set was instead used to iterate 2, 4, 6 times the growth steps of Fe-DT wires.

UV-Vis measurement was performed on each sample in order to measure the shift of the plasmonic peak of each MW after an increasing number of growth iteration

cycles. The results are summarized in Figure 54 for Fe/Ru_2DT_3 system and in Figure 55 for FeDT ones.

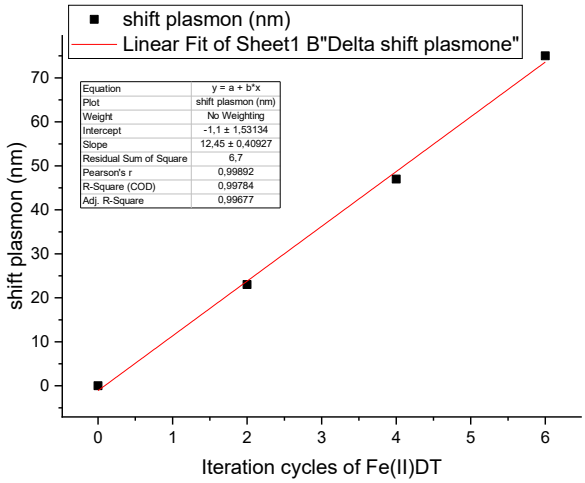

Figure 54 UV-Vis measurements: shift of the plasmonic peak of the Fe/Ru2DT3 system as function of the number of growth cycles.

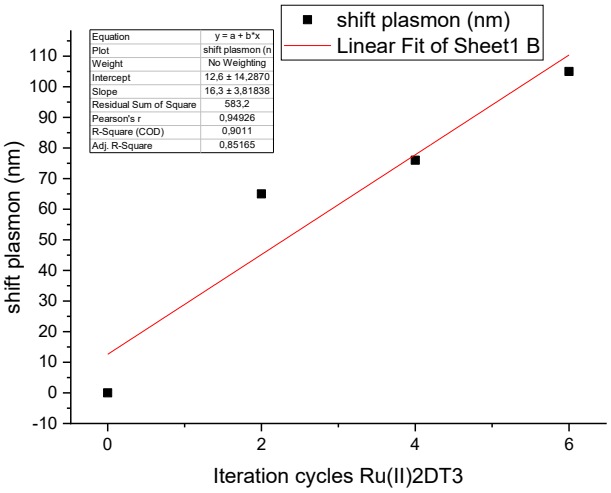

Figure 55 UV-Vis measurements: shift of the plasmonic peak of the FeDT system as a function of the number of growth iteration cycles.

The measurements show a linear variation of shift the Au plasmon position as a function of the nominal length of the wires, at least in the explored length range.

The evaluation of assembly process of the two different types of MWs was also performed on transparent oxide substrates. To achieve this, the experimental preparation procedure is the same as that previously described for gold surfaces but with the crucial difference of the priming procedure of the substrate's surface, which is the one based on ZP priming already described.

Hence, instead of thiols mixture, (2,2': 6' 2'' terpyridine 4yl) benzenephosphonic acid (PPTP) was used because it binds to the surface Zr through the phosphonic function, and exposes the terpyridine functionality to the coordination with iron ions. Molecular wires of increasing length based on FeDT only (3, 6, 9 growth cycles) and Ru_2DT_3 (3, 6, 9 growth cycles) on quartz substrates functionalized with ZP-PPTP procedure, were monitored by transmittance-mode UV-Vis spectroscopy focusing the attention to the peak of the metal-to-ligand charge transfer (MLCT) characteristic transition (Figure 56 and Figure 57).

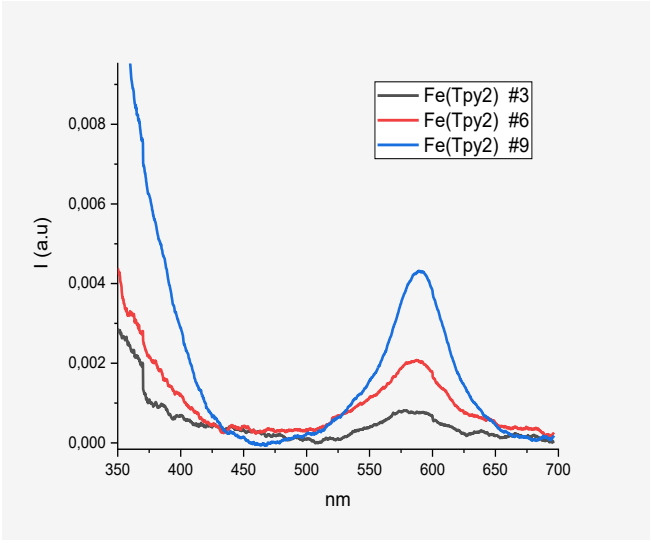

Figure 56 UV-Vis absorption spectra of molecular wires of different length (3layer, 6 layer,9 layer of FeDT assembled units) grown on semitransparent gold surface

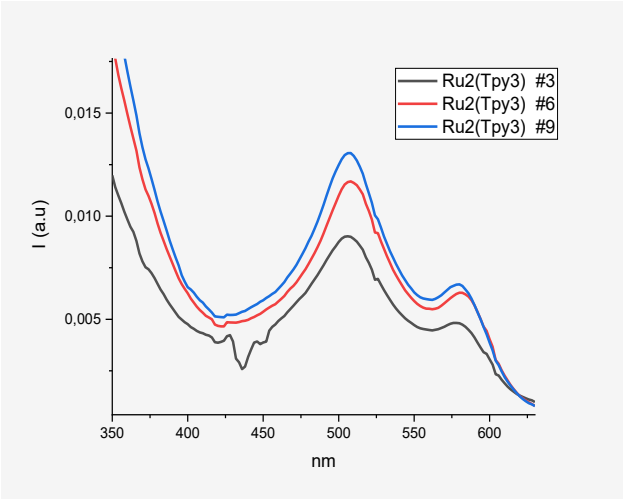

Figure 57 UV-Vis absorption spectra of molecular wires of different length (3-, 6- and 9- layers of Ru2 assembled units) grown on semitransparent gold surface

Time-of-Flight Secondary Ion Mass Spectrometry characterization

Time-of-flight secondary ion mass spectrometry in static and 2-D mode was used to validate the functionalization's of the various surfaces in the different assembly steps of the molecular wire.

The spectra were acquired in a TOFSIMS IV (ION-TOFGmbH, Münster, Germany) instrument. Spectra were acquired using 25 keV Bi^+ primary ions (~ 0.5 pA), rastered over 150 µm x150 µm. Static conditions (Bi^+ primary ion fluence < 10^{12} ions·cm^{-2}) were used in order to preserve the molecular information from the surface. The 2-D images were acquired in the same condition above described unless the size of the raster that has been set to 500 µm x 500 µm.

Figure 58 reports the spectrum of the MB/MPTP SAM used as platform for the growth of the wire. Several peaks, diagnostic of the formation of the SAM on gold, are observed, such as $[C_{21}H_{14}N_3AuH]^+$ (506 u) and $[C_{21}H_{14}N_3AuSH]+$ (538 u) which are quasimolecular ions of MPTP.

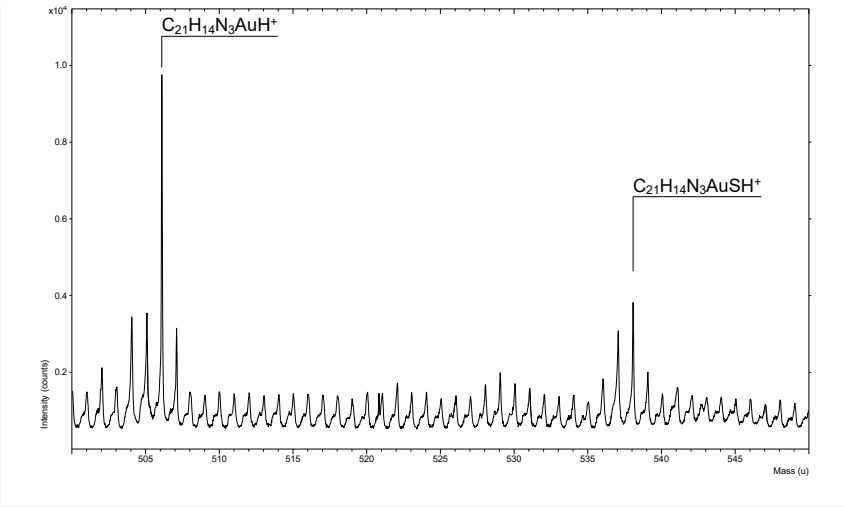

Figure 58 ToF-SIMS mass spectrum of the MB/MPTP SAM used as platform for the growth of the wire. Several peaks, diagnostic of the formation of the SAM on gold, are observed, such as $[C_{21}H_{14}N_3AuH]+$ (506 u) and $[C_{21}H_{14}N_3AuSH]+$ (538 u) *which are quasimolecular ions of MPTP.*

In the following the spectra of six-units-long molecular wires on gold are reported, either based on FeDT or on Ru_2DT_3.

Figure 59 shows a portion of the spectrum of the FeDT-based system, where it is shown the isotopic distribution associated with a fragment of the molecular wire, namely the repeating unit plus the counterion, $[C_{36}H_{24}N_6FeCl]^+$ (631.1 u); in addition Figure 60 shows an higher mass portion of the same ToF-SIMS spectrum, where it is possible to identify peaks associated to iron ion linked with two bisterpyridine molecular units $[C_{72}H_{48}N_{12}Fe]+$ (1136.3 u).

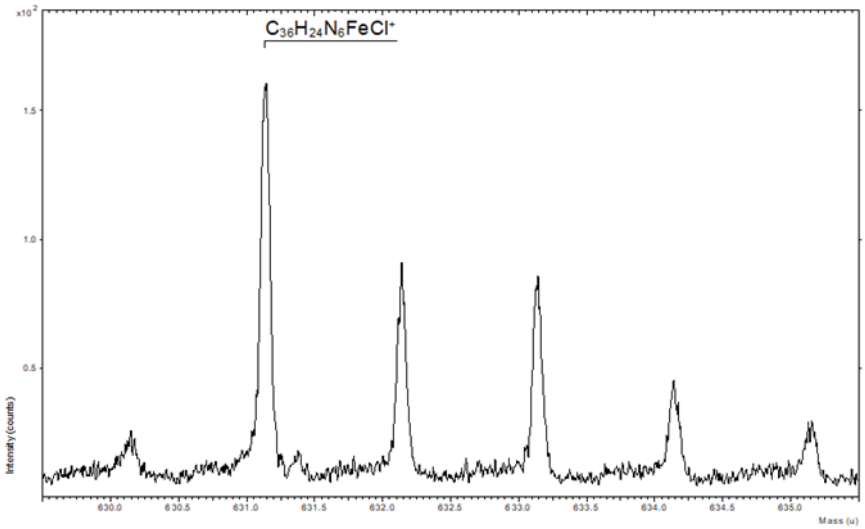

Figure 59 Part of the ToF-SIMS spectrum of the FeDT-based system, showing the isotopic distribution of a fragment of the molecular wire, namely the repeating unit plus the counterion, [$C_{36}H_{24}N_6FeCl$]+ (631.1 u)

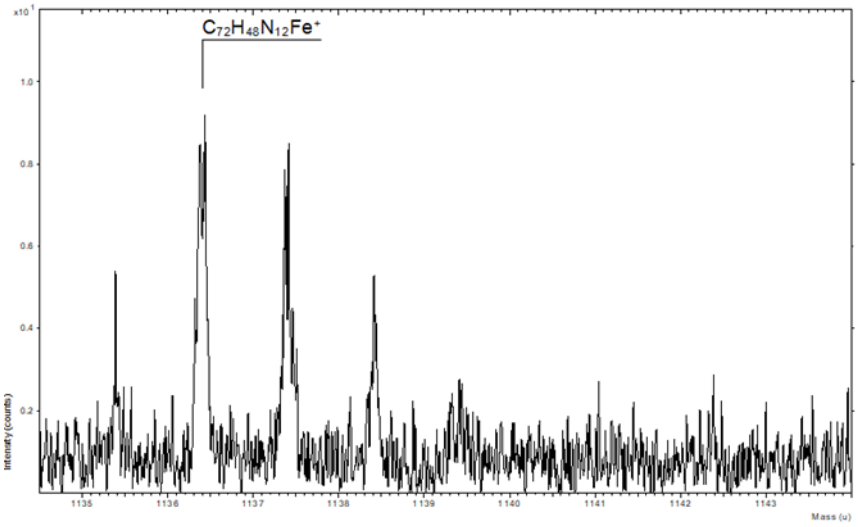

Figure 60 Part of the ToF-SIMS spectrum of the FeDT-based system, showing the isotopic distribution of [$C_{72}H_{48}N_{12}Fe$]+ (1136.3 u)

Analogously, peak distributions, diagnostic of the formation of the MWs based on Ru_2DT_2 units can be observed in Figure 61, where is possible identify the distributions related to: RuDT $[C_{36}H_{24}N_6Ru]^+$ (~ 640 u), RuDT-O $[C_{36}H_{25}N_6Ru]^+$ (~ 659 u) and RuDT-Cl $[C_{36}H_{25}N_6RuCl]^+$ (~ 678 u).

In the higher mass portion of the spectrum, shown in Figure 62, heavier ion fragment, related to the molecular wire are detected, such as $RuDT_2$ $[C_{72}H_{48}N_{12}Ru]^+$ (~ 1180 u), $RuDT_2O$ $[CH_{48}N_{12}RuO]+$ (~ 1196 u) and Ru_2DT_2 $[C_{72}H_{46}N_{12}Ru_2]+$ (~ 1280 u).

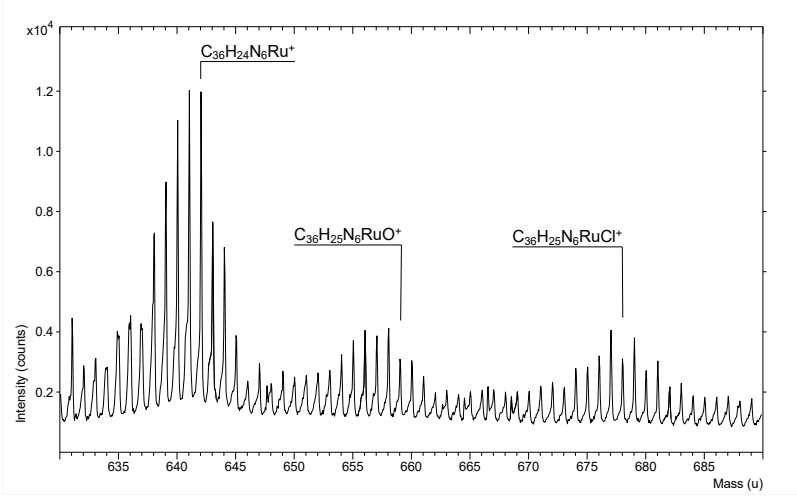

Figure 61 Part of the ToF-SIMS spectrum of the Ru2-based system, showing the isotopic distribution of RuDT [C36H24N6Ru]+ (~ 640 u), RuDT-O [C36H25N6Ru]+ (~ 659 u) and RuDT-Cl [C36H25N6RuCl]+ (~ 678 u)

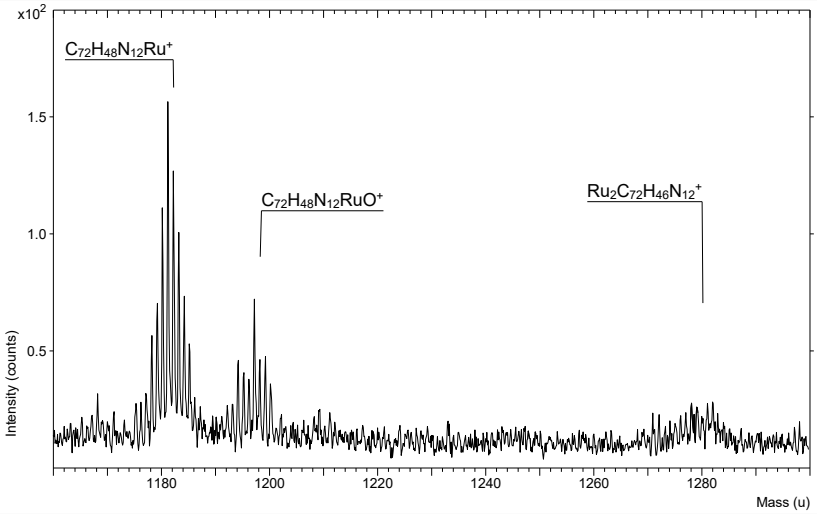

Figure 62 Part of the ToF-SIMS spectrum of the Ru2-based system, where it is shown the isotopic distribution associated to RuDT2 [C72H48N12Ru]+ (~ 1180 u), RuDT2O [C72H48N12RuO]+ (~1196 u) and Ru2DT2 [C72H46N12Ru2]+ (~ 1280 u).

8.5 Conclusion

In this section, studies have been carried out on the anchoring properties of molecular wires based on terpyridine complexes with iron and ruthenium, assembled on quartz, and semi-transparent gold on quartz substrates. The UV-Vis spectroscopy characterization on quartz substrates allowed to follow the linear increase of the number of photoactive centers when the number of iterative assembly cycles is increased.

The growth procedure on of the semitransparent nanostructured gold substrates allowed the evaluation of the plasmon shifts associated with the growth of the wires, and showed that it depends linearly on the wire chemisorption process.

ToF-SIMS measurements confirmed the formation of the coordination complexes at the surface and allowed monitoring of the growth steps of both the iron-based and iron-ruthenium-based complexes.

9 TOF-SIMS IMAGING AND UV-Vis CHARACTERIZATION OF NANO-ENGINEERED SURFACES

The following experimental task was focused on the development of experimental strategies in order to obtain spatially resolved areas functionalized by molecular wire systems, to be involved in surface engineering of different types of solid substrates that can be interesting for the design of innovative devices in the field of nanoscience and nanotechnologies.

9.1 Spatially resolved functionalization of surfaces with metalorganic three-dimensional architectures

The main purpose of this task was to build up a patterned self assembled layer of molecular wires-based systems exploitable in the field of molecular electronics to carry out some information related to the morphological characteristics. To this aim, a photo-pattering approach on functionalized surfaces was explored on the following substrates:

- Silicon: the substrate was previously covered by a self-assembled monolayer of octadecylphosphonic acid (ODPA), and the molecular wires was assembled in a pre-formed pattern obtained removing the ODPA layer by a patterned photodegradation process.

- Quartz: this substrate was used to monitor the growth of the supramolecular wire, to estimate their growth rate by means of UV-Vis spectroscopy.

The first step of this experimental task has involved the fabrication of a self-assembled monolayer of alkylphosphonate organic molecule. A silicon substrate was exposed to ZP-priming procedure to produce, as showed in the schematic in Figure 63, a self-assembled monolayer of octadecylphosphonic acid.

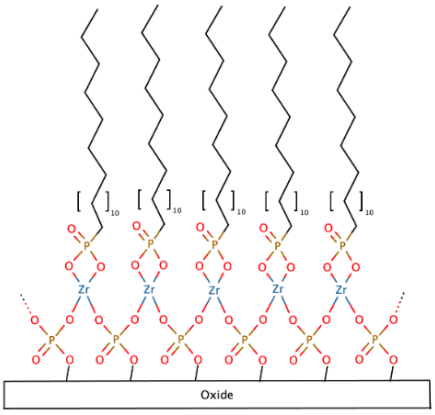

Figure 63 Schematization of self-assembled monolayer of octadecylphosphonic acid onto a ZP-primed oxide surfaces.

Subsequently a photolithographic hard mask was put over the ODPA functionalized silicon surface. The ODPA layer was selectively removed through the hard mask open regions by exposition to to UV-O_3 for 10 minutes. Therefore, the areas free from phosphonic acid (were exploited to bind and grow up supramolecular wires. The synthesis strategy for the formation of the wire is based on the use of complexes composed of the Fe (II) ion and the ligand 4′,4′′′′-(1,4-phenylene) -bis (2,2 ′: 6 ′, 2′′terpyridine), refer to with the acronym DT. Fig. 64a shows the structure of the $Fe(DT)_2$ complex. In figure. 64b, it is possible to see an example of assembly of the molecular wire strictly anchored in the areas exposed to the UV-O_3 treatment.

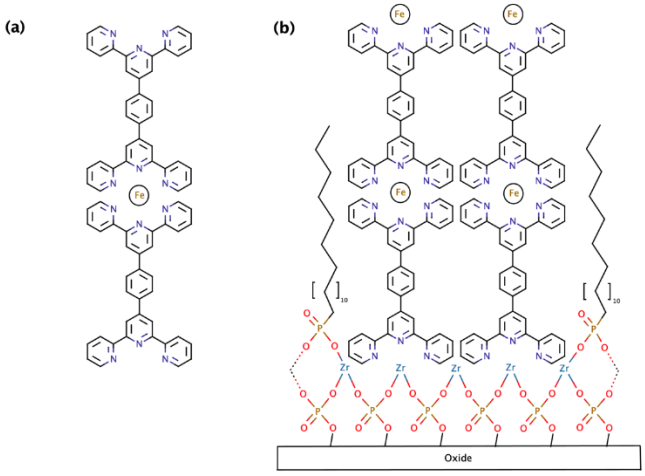

Figure 64(a-b) 64a: Structural representation of $FeDT_2$ complex; 64b self-assembled monolayer of octadecylphosphonic acid and $FeDT_2$ complex onto a ZP-primed oxide surfaces

As previously introduced the wire based on complexes of the type M(II) $(DT)_2$, were anchored onto the ZP-priming layer by using phosphonic acid named 4 (2,2 ′: 6′-2 ′ ′ - terpyridine-4-yl) benzenephosphonic acid (PPTP), shown in figure 65, which has a terpyridine as terminal group, where the divalent metal can be complexed. The phosphonic group, on the other hand, react with the exposed zirconium ions, forming a very stable base for molecular wire anchoring. This synthetic strategy was developed by Spampinato et al[36].

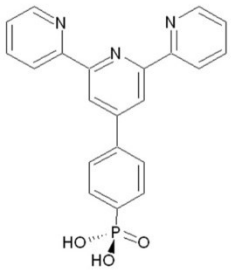

Figure 65 Chemical structure of PPTP 4(2,2':6'-2''-terpyridine-4-yl) benzenephosphonic acid

To further simplify the anchoring procedure of these supramolecular wires on the surface, the anchoring has been here conducted by directly bind the DT ligand with

the apical zirconium of the ZP-primed surface. This approach via Zr (IV) has already been studied in the literature both in liquid and solid phases[126]

Materials and Methods

The substrates were rinsed in boiling chloroform and dry in N_2 flow. Before surface functionalization steps, they have been treated by UV-O_3 or O_2 RF plasma and rinsed by MilliQ™ water.

ZP-priming procedure

The experimental steps used to prepare oxide surface by using ZP-priming procedure are shown Fig. 66.

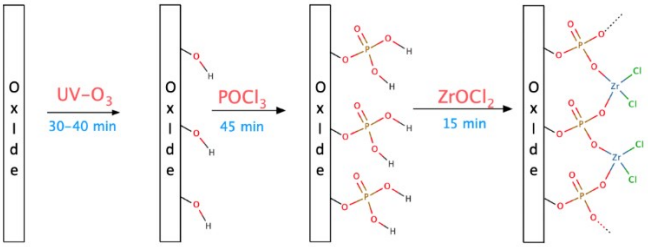

Figure 66 Reaction scheme for the ZP-priming procedure on oxide surface.

After drying the substrate, UV-O_3 treatment is carried out to allow the surface to generate -OH functionalities. This hydroxylic group is used to bind the phosphate groups after immersion of 45 min in pure $POCl_3$. Lastly, after several immersion

water, substrate is immersed into 10^{-4} M zirconyl chloride solution. By following the prementioned steps a monolayer of Zr (IV) dichlorophosphate is obtained.

9.2 Patterning via UV-O_3

For this step of the experiment, it was necessary to fix an optimal reference system, in order to find the areas exposed to UV-O_3 during the characterization phase at ToF-SIMS and the profilometer. To this aim, the mask alignment position on the substrate was marked by screeching the areas exposed to UV-O_3. Fig. 67 shows the mask used:

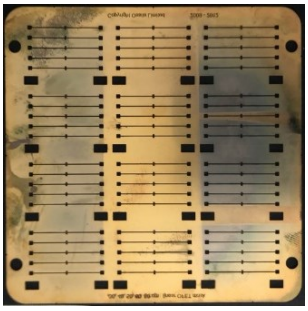

Figure 67 Photolithographic mask

After 7 minutes under UV-O_3 exposition, the sample is washed first in chloroform and immediately after in ethanol, to remove the oxidized fragments produced during the photodegradation treatment. To prove this even when the sample is exposed to air, after being rinsed in chloroform, a variation in wettability is noted, for a few moments before the solvent evaporation, between the oxidized areas and the areas covered by the mask (Figure 68).

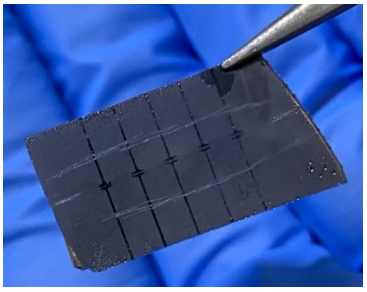

Figure 68 Picture obtained after the photolithographic process performed on Si-ZP primed substrate functionalized with a self-assembled monolayer of octadecylphosphonic acid (ODPA).

9.3 Assembly of the supramolecular wire

As already mentioned, the construction of molecular wire in the past was carried out in a slightly different way from the methodology used in this experimental section. One of the main differences is related to the elimination of two steps performed after the ZP-priming procedure: the exposition of substrate to Zn-$(PPTP)_2$ solution and the step of protonation-disassembling of Zn-$(PPTP)_2$ complexes, Figure 69:

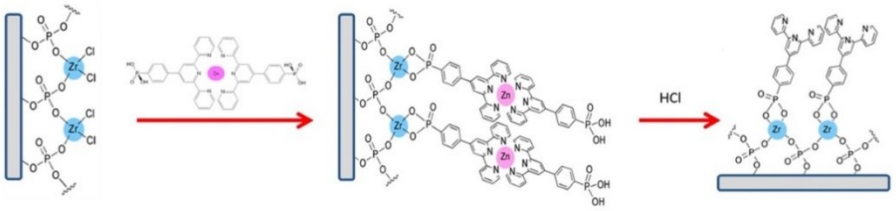

Figure 69

Instead, it was decided to directly anchor the DT to the Zr ion via the (Fig. 70) chemical platform formed by ZP priming procedure steps, by dipping the substrate on which the photo patterning has already perfomed, in a chloroform solution of DT in 10-5 M for five hours, in order to avoid a " possible replacement of the ODPA with the DT".

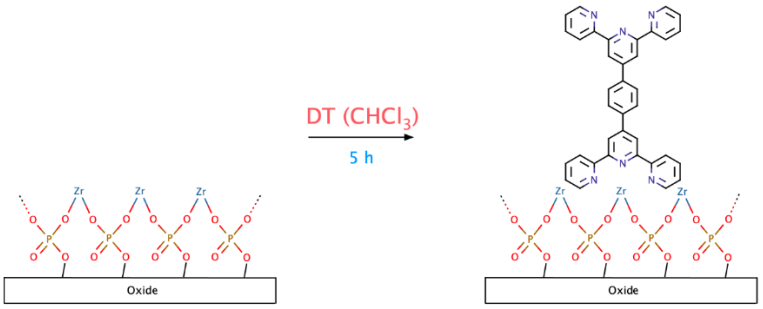

Figure 70 Scheme of the anchoring between a ZP-Primed oxide surface and DT ligand.

9.4 UV-Vis analysis

UV-Vis spectroscopy is one of techniques that can be used to monitor the growth of the supramolecular wire because in each cycle of growth, photoactive metal centers are iteratively anchored at the substrate's surface. Indeed, a linear increasing absorbance signal is recorded at increase of each cycle of assembling procedure

based on FeDT units . The signals that will be monitored are the 593 nm band relating to the transition (MLCT) of the $FeDT_2$ complex and the 290 nm band of terpyridine.

Quartz samples were prepared, on which molecular wire having an increasing number of metal centers were assembled. As can be seen from the spectra in Figure 71, the increase in absorbance follows the increasing trend of the number of layers present in each sample, and this trend is confirmed both for the terpyridine band and for the MLCT band of the complex.

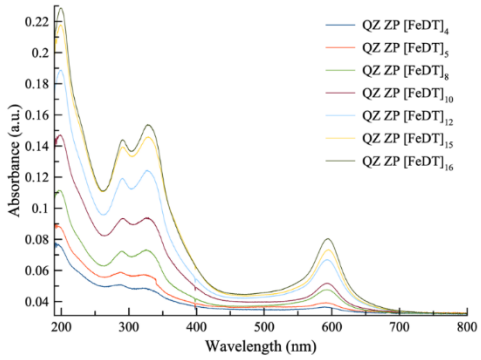

Figure 71: UV-Vis absorbtion spectra of assemblies of molecular wires of different nominal lenght

In Fig. 72 and 73 linear best-fits are shown, in which respectively the MLCT band of the complex and the π-π* terpyridine band are reported as a function of the nominal number of layers assembled.

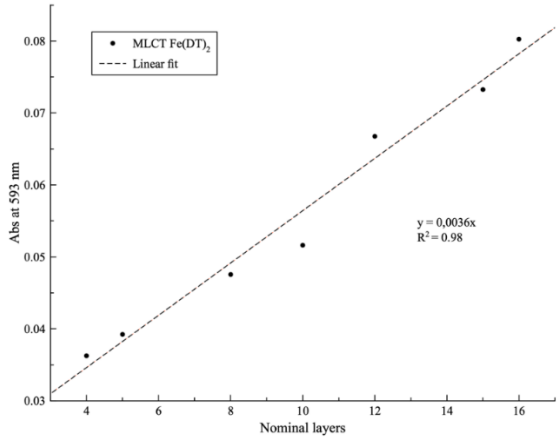

Figure 72: Intensity of the MLCT peak of the molecular wires, as a function of the nominal wire length (number of growth cycles)

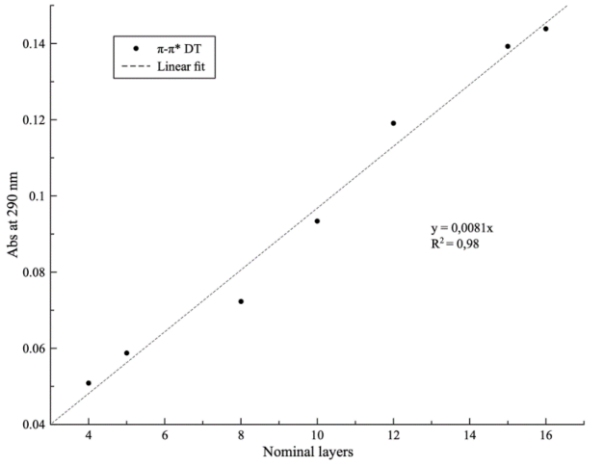

Figure 73: Intensity of the ligand-related band alt 260 nm, as a function of the nominal length (number of growth cycles)of the molecular wire

Considering that in both best fits the linear correlation coefficient value (R^2) is 0,98, we can state that the anchoring experimental procedure shows a linear based function correlation between growth cycles and UV-Vis absorption spectra parameters. This behavior it is potentially used to predict the optical feature of functionalized samples.

Finally, it worth to be noted that the ratio between the angular coefficients of π-π* terpyridine band fit and MLCT band reflects the 1:2 stoichiometry ratio between the

metal centers and DT lignads in Fe(DT)2 molecule. (Slope A) / (Slope B) = 0.0081 / 0.0036 = 2.25

9.5 ToF-SIMS analysis

The stepwise approach with which the samples were made, starting from the formation of the ODPA SAM, up to the assembly of the supramolecular wire of (FeDT) n on the area treated with UV-O_3, was monitored step by step by means of ToF-SIMS.

To this aim, the ability of ToF-SIMS to provide spatial resolved detailed molecular information on the uppermost layer of a surface was exploited to detect its SAM of ODPA functionalization and the growth of $FeDT_n$ based systems in the areas exposed to UV-O_3.

The measurements were carried out using a 25 keV $Bi3^+$ primary ion source, with a 0.5 pA of primary ion current, rastered on a 500x500 µm area. The primary ion fluence was kept under 10^{12} ions cm^{-2}, assuring the so-called "static conditions".

The first analyzed step was the ZP priming; Figure 74 and Figure 75 show the areas of the positive ion spectrum of where some characteristic peaks of the zirconium phosphate layer: Zr + (90 u), ZrO + (106 u), ZrO_2 + (122 u), $ZrPO_3$ + (169 u), $ZrPO_4H_2$ + (187 u) and $ZrPO_5H_2$ + (203 u) were detected, confirming the formation of zirconium phosphonate on the surface.

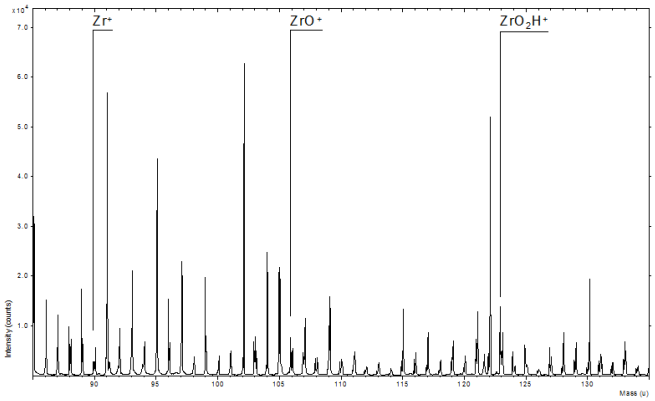

Figure 74

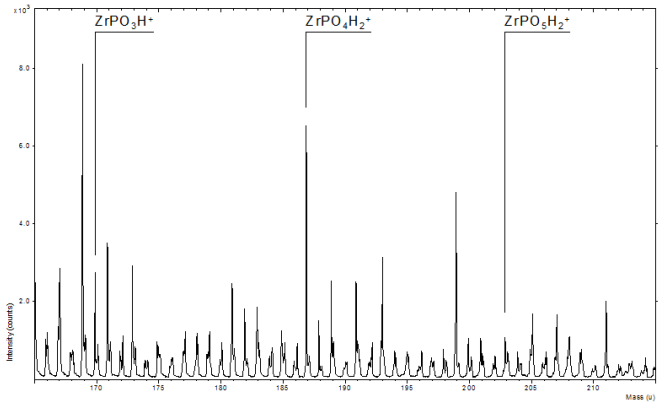

Figure 75

A new ToF-SIMS analysis was performed after the anchoring of the ODPA to the zirconium phosphate primer layer. The molecular peak and some characteristic fragments were identified in the spectrum (figure 76): $C_{18}H_{39}O_3PH$ + (335 uma), together with other characteristic peaks: (Fig. 77) C_3H_7 + (43 uma), (Fig. 78): C_5H_{11} + (71 uma), (Fig. 79): C_6H_{13} + (85 uma).

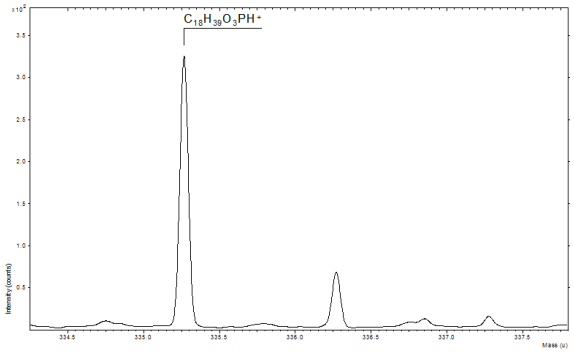

Figure 76

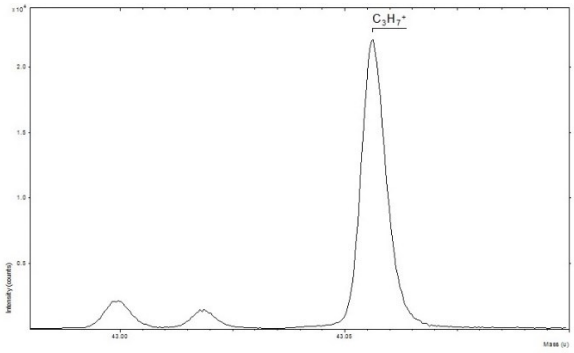

Figure 77

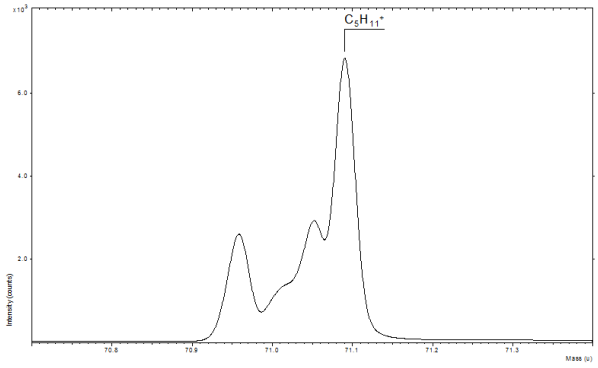

Figure 78

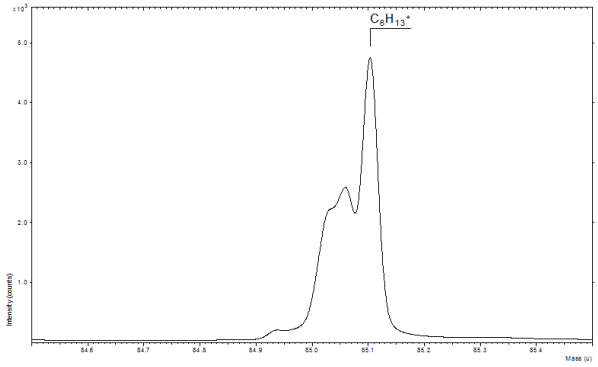

Figure 79

In order to check the ODPA removal from exposed areas, ToF-SIMS chemical images have been acquired. To obtain an ion image, the focused Bi3+ primary ion beam scans the sample surface pixel by pixel. A mass spectrum is then acquired for each pixel. By recording the positions of the beam while scanning, a color map of

the signal intensity for each ion can be constructed across the scanned area, providing a so-called ion image. These ion images show the distribution of the ions on the surface. All the images shown below were acquired in static conditions, using the Bi3 + as analysis beam and acquiring 100 scans of an 500 µm x500 µm area.

Figure 80 shows the $^{30}Si^{+}$ ion image, in which the signal is distributed evenly over the entire sampled area; in Fig. 81and Fig. 82 instead it can be seen how the central section, corresponding to the pattern of the mask used for the treatment with UV-O_3, presents a more intense signal for the fragments of ZrO^{+} and $ZrPO_5H_2^{+}$ due to a greater ionization yield due to the oxidation, or because they are more present in this section.

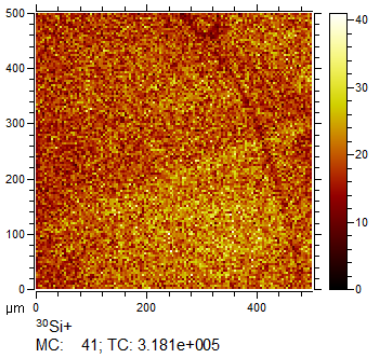

Figure 80: $^{30}Si^{+}$ ion image of the patterned ODPA SAM

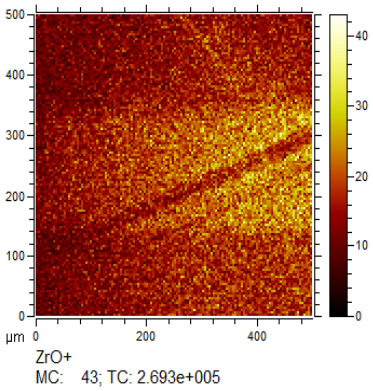

Figure 81: ZrO^{+} intensity distribution after patterning of the ODPA SAM

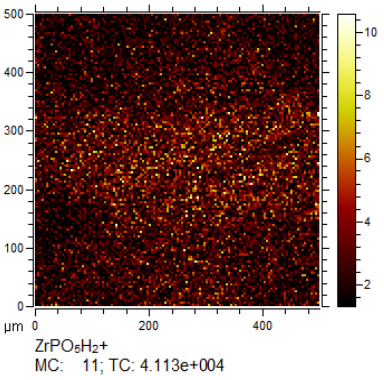

Figure 82 $ZrPO_5H_2^{+}$ intensity distribution after patterning of the ODPA SAM

Figures 83-84 show the ToF-SIMS maps of two hydrocarbon fragments related to ODPA and figure 85 the map of the ODPA molecular ion. These maps suggest a spatially selective photo assisted removal of ODPA.

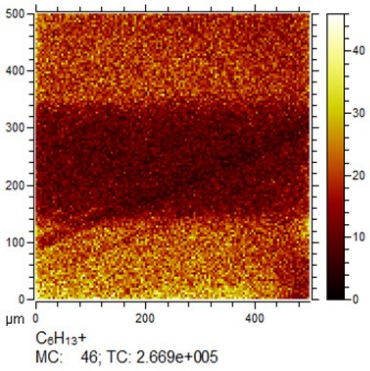

Figure 83: intensity distribution of the $C_6H_{13}^+$ peak on the patterned ODPA SAM

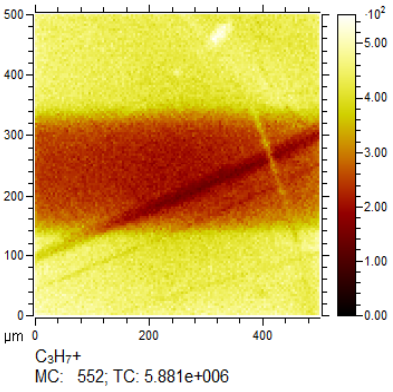

Figure 84: intensity distribution of the $C_3H_7^+$ peak on the patterned ODPA SAM

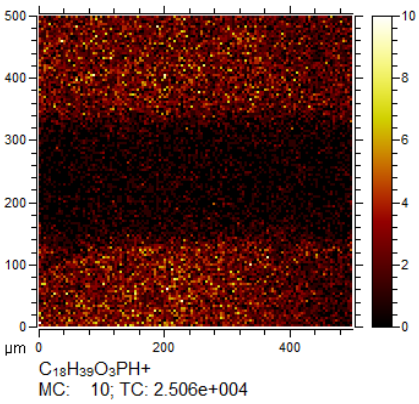

Figure 85: map of the ODPA molecular ion on the patterned ODPA SAM

.

After the spatially resolved photo assisted remotion of the ODPA self assembled monolayer the sample was employed in grow iterative procedure based on Fe-DT units.

After 5 growth cycles of the wires, the sample was characterized again by using ToF-SIMS imaging.

The intensity distributions (chemical images) of secondary ions characteristic of the assembled Fe-DT_2 -based molecular wires are shown in figures (86-89). We note that all the wire-related peaks, including a pyridine fragment (C_5H_4N +), Fe(II), and larger ios coming from the FeDT complex, are concentrated within the areas were the ODPA was removed.

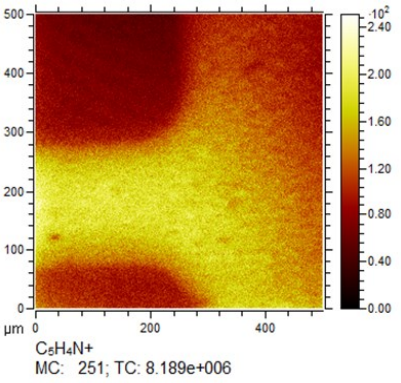

Figure 86: map of $C_5H_4N^+$ signal on the patterned ODPA SAM after growth of the wires

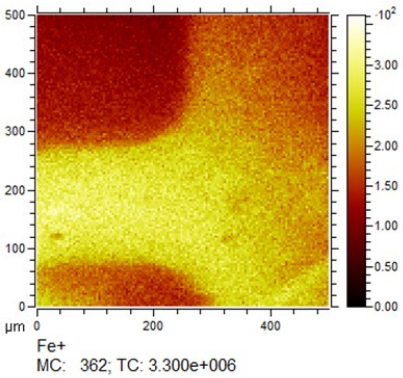

Figure 87: map of Fe^+ signal after growth of the wires on the patterned ODPA SAM

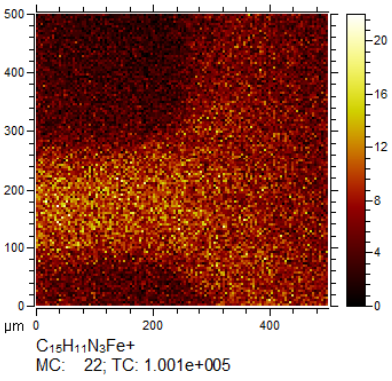

Figure 88: map of $C_{15}H_{11}N_3Fe^+$ signal after growth of the wires on the patterned ODPA SAM

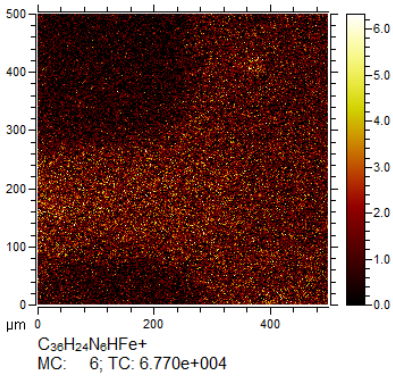

Figure 89: map of $C_{36}H_{25}N_6Fe^+$ signal after growth of the wires on the patterned ODPA SAM

At the same time, the maps reported in Figures 90-93 show that the signals of $ZrPO_3H^+$ and $ZrPO_4H_2^+$, $C_3H_7^+$, $C_5H_{11}^+$ are still present outside the areas treated with UV-O3 where, instead, the wires were able to grow.

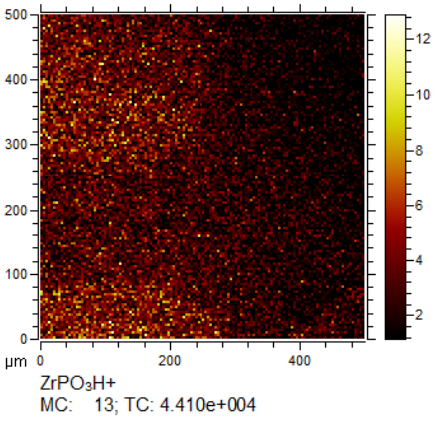

Figure 90: Chemical map of $ZrPO_3H^+$ signal after growth of the wires on the patterned ODPA SAM.

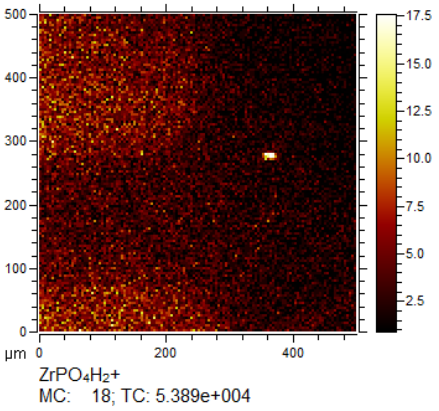

Figure 91: Chemical map of $ZrPO_4H_2^+$ signal after growth of the wires on the patterned ODPA SAM.

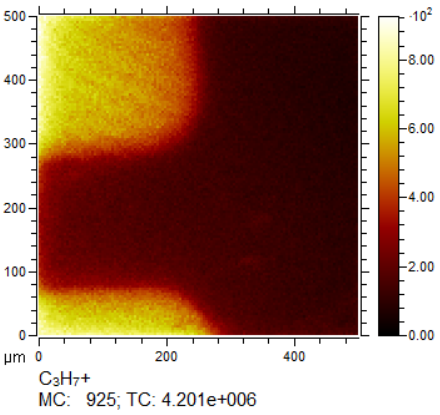

Figure 92; Chemical map of $C_3H_7^+$ fragment after growth of the wires on the patterned ODPA SAM.

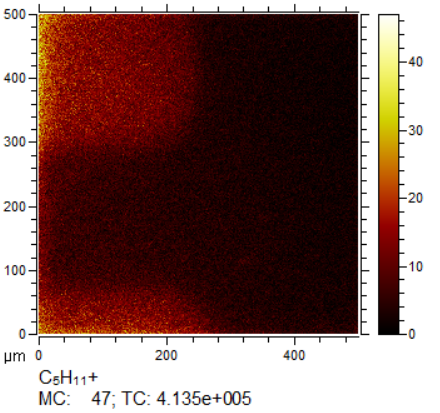

Figure 93: Chemical map of $C_5H_{11}^+$ fragment after growth of the wires on the patterned ODPA SAM. Note that the distribution is superimposable with those of figures 90-92 and complementary with those of figures 86-89

Finally, Figure 94 and Figure 95 shown two 3D maps (Carpet plot) of intensity respectively of complementary signals: $C_3H_7^+$ and $C_{36}H_{24}N_6FeCl^+$ thaken from a region of the sample containing the pattern:

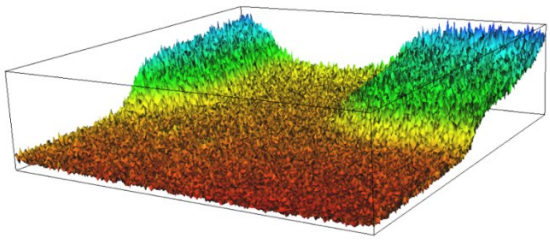

Figure 94 3D maps (Carpet plot) of intensity respectively of C3H7 + signal

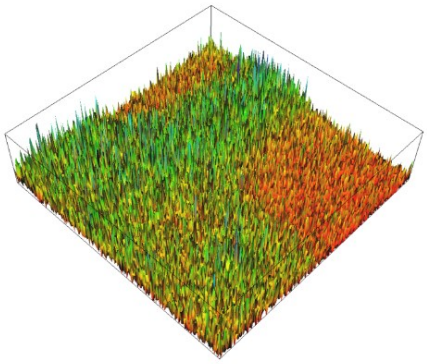

Figure 95 3D maps (Carpet plot) of intensity respectively of C36H24N6FeCl + signal

9.6 Stylus profilometer analysis

By exploiting the reference system created on the sample to find the areas of the pattern during the characterization phase, it was possible to obtain height data for a series of samples having a nominal number of layers equal to 6, 10, 15, 20. For each sample about ten measurements were made, and an average was obtained from these. Fig. 96 shows a typical profile of a sample of $(FeDT)_{10}$, in a specific area where it is noted that the pattern has a height of about 10 nm.

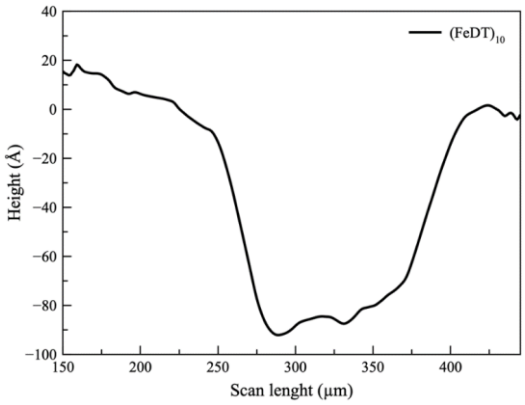

Figure 96: height profile of a patterned sample with a 10-units-long FeDT wire. The lower region is that where the ODPA was not removed, while the two higher regions are those with the wire assembly.

Fig. 97 shows a linear best-fit relating to the averaged height data obtained with the profilometer from samples having an increasing number of layers.

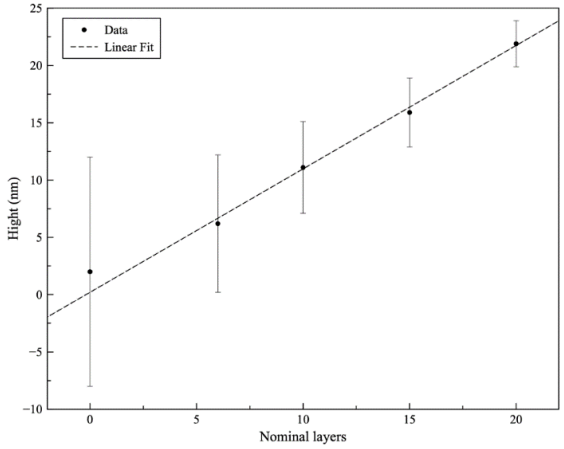

Figure 97: step height or the wire pattern as a function of the nominal number of FeDT units in the wire.

Knowing that the length of a DT, obtained from density functional theory (DFT) data by Dr. von Wrochem in structures identical to those created in this thesis but anchored on Au with thiols, is around 15.5 Å [35] and knowing the heights of each sample, it is possible to estimate the angle of inclination at which the molecular wire are located. The slopes of these graphs correspond to the average height along the z direction of a Fe-DT-Fe coordination step; in their case this slope turns out to be

around 1.08 nm [35], while in our case it is 1.10 ± 0.04. Considering each set of samples, the hypothetical average angle of inclination of the wire was theoretically estimated.

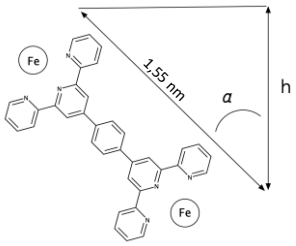

Figure 98

Using a trigonometric formula applied to the right triangle shown in (figure 98), we obtain:

$$cos\alpha = \frac{h\,(nm)}{1{,}55\ nm}\ ;$$

$$\alpha = \ 44{,}7 \pm 1{,}8°$$

9.7 Conclusions

During this task of PhD activity, we contributed to the realization of a patterning of supramolecular wires of polypyridine complexes of transition metals on oxides. The methodology used involves a pre-treatment of the surface to constitute the anchoring platform of both the wires and the SAM of the phosphonic acid used, the ODPA. This platform can be made with a priming method based on the chemistry of zirconium phosphates/phosphonates. Following the formation of the phosphonic acid self-assembled monolayer, we proceeded with the UV-O_3 treatment in the presence of a mask and then with the assembly of the supramolecular wire in the treated areas. Through UV-Vis and ToF-SIMS characterization it was possible to confirm the anchoring and growth of the molecular wire. The characterization with Profilometer made it possible to calculate the heights of the structures obtained.

10 PHOTOCONDUCTIVE PROPERTIES OF MOLECULAR WIRES BASED ON Ru(II) AND Fe(II) BISTERPYRIDINC COMPLEX STUDIED VIA PATTERNING APPROACH.

The photoconductive properties of the molecular wires based on Ru (II) 2DT3 units and based on Fe(II)DT2 units were measured by means of a patterned substrate designed ad hoc designed, fabricated and assembled in house.

Four gold stripes (500micron wide, 10mm long, around 90 nm high and mutually distant 1 mm) were deposited by sputter deposition via hard-mask patterning approach on a 900nm silicon thermal oxide substrate. The assembled chip was then subjected to an oxygen plasma treatment to remove any organic contaminants. After this cleaning step, the chips were subjected to the molecular wire assembly procedure already described in the case of gold semitransparent surfaces.

One of these chip series was functionalized with the molecular wires based on the $Ru(II)_2DT_3$ system, while another chip with the $Fe(II)DT_2$ system.

In order to create a set-up for measuring the electrical properties of the assembled supramolecular systems, it was necessary to develop an experimental patterning procedure. By exploiting a "lift off" approach with positive photoresist, micrometric conductive Au tracks were generated on an insulating substrate of thermal silicon oxide.

Reagents used:

- SiO_2 (thermal oxide on silicon)

- Polymethylmethacrylate (PMMA) 2% solution

- Photolithography mask (Ossila)

- Chloroform $CHCl_3$

- Isopropanol $(CH_3)_2CHOH$

- Dimethylformamide (DMF)

- MB / MPTP solution in 10^{-4} M ethanol

- Iron (II) salt: 3mg $FeSO_4$ 7H2O in 40mL of H_2O

- DT solution in chloroform 10^{-4} M

- PEDOT:H_2O (Merck)

All chemicals and materials listed above, where the origin is not specified, have been purchased from Merck | Italy - Sigma-Aldrich and used as received.

It is possible to outline the experimental procedure as follows:

- PMMA deposit on the substrate through POLOS200 SPIN COATER

- Application of hard mask; 60 min of UV light exposure. In this step, the PMMA not covered by the mask is photodegraded.

- Development via isopropanol; ultrasonication for 2 min.

In this step the pattern is already optically visible. It is precisely noted that in the portions of the surface in which the PMMA has not been exposed, the polymer remains stuck to the surface of the thermal silicon oxide. On the other hand, in the areas exposed to UV-O_3 treatment, no traces of the polymeric film are observed.

- N_2 flow to dry the sample

- Sputter Au 60 seconds, current of 50 mA with Q150R ES sputter coater

- Immersion in 2:1 $CHCl_3$ / DMF solution to remove excess PMMA and Au; 1 min ultrasonication to remove mechanically what has not been chemically removed and facilitate the development process; 15 min UV-O_3 to remove any organic contaminants from the surface. At this point, gold tracks adhere to the silicon oxide substrate remain on the areas exposed to UV light, while the gold deposited on PMMA is removed simultaneously with the dissolution of the underlying PMMA ("lift-off" process [127]).

- 24 h incubation in MB/MPTP equimolar solution, to form the SAM on the gold tracks.

- Assembly on a series of patterned Au-SiO_2 chip, 10 cycles of Fe-DT using the assembly procedure previously described, instead on another series of patterned Au-SiO_2 chip, 10 cycles of $Ru(II)_2$-DT_3.

- Partial coverage of the sample with an aqueous solution of PEDOT: H_2O.

The latter is a conductive polymer that acts as a second soft electrode for conductivity measurements

The procedure just described is schematically summarized in Figure 99, instead the finished prototype it is showed in Figure 100.

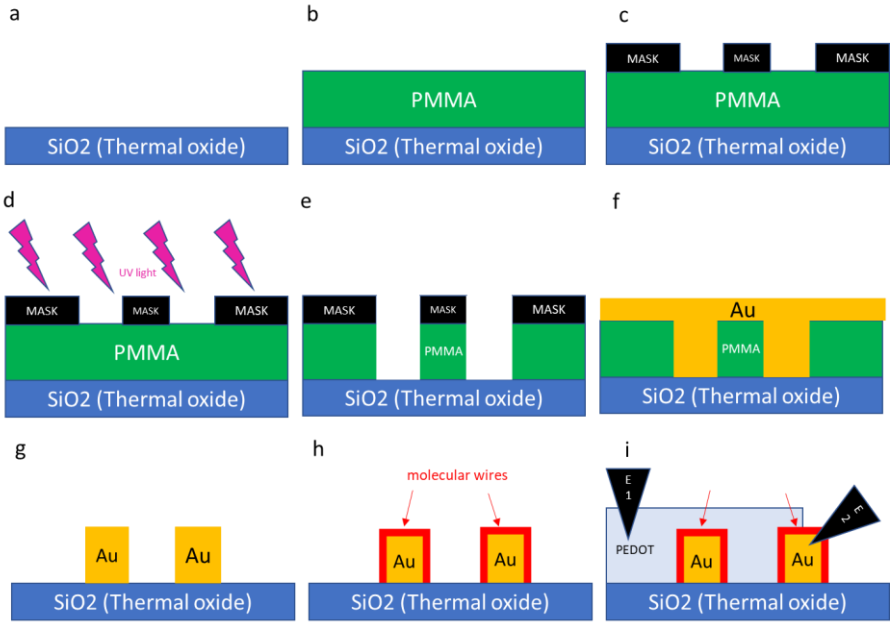

Figure 99 Steps involved in Au-SiO_2 patterned chip fabrication: a) thermal silicon oxide is cleaned by UVO_3 treatment, b) PMMA film is spincoated, c)hard mask is aligned on substrate, d)UV exposition to degradation the polymer exposed, e) develop with isopropanol, f Au coating via sputter deposition, g) lift off of polymer via chloroform, h growth of molecular wire, I partially PEDOT covering and electrodes application

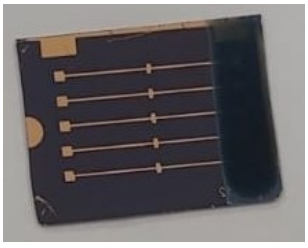

Figure 100 photo of the complete patterned system. The dark blu stripe on the right is the PEDOT electrode.

10.1 Characterization: ToF-SIMS imaging and profilometer

Figure 101 shows the mass resolved ToF-SIMS images (chemical maps) obtained after the development step after UV irradiation (step e of figure 100). In images, lighter colors represent higher intensity and darker colors represent minor intensity. In particular, the intensity distributions of characteristic PMMA and silicon signals

as well as their overlap are reported. These maps confirm the success of the photolithographic process.

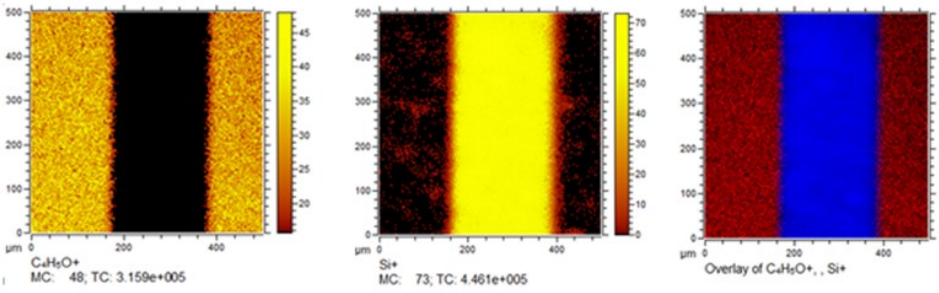

Figure 101 From left to right ToF-SIMS images of secondary ions related to PMMA used as photoresist , Silicon used as substrate, overlay of these respectively in red and blue false colors.

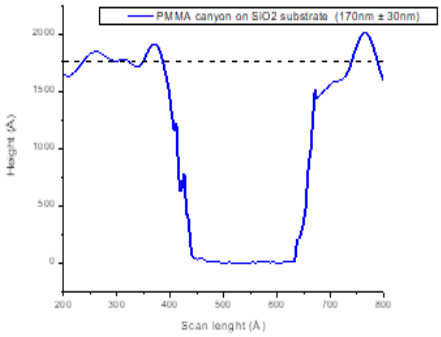

Figure 102 profilometer 2D scan of PMMA channel produced after step d

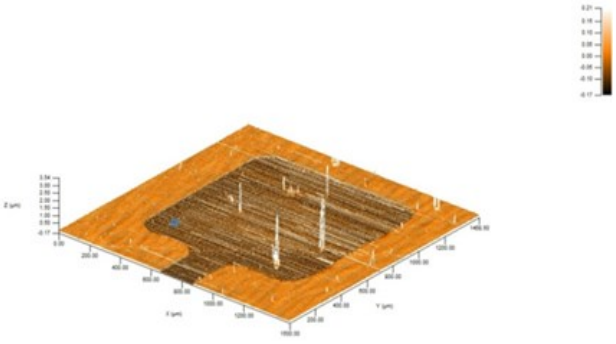

Figure 103 profilometer 3D scan of PMMA "hole" produced after step d

Figures 102 and 103 concern profilometry measurements obtained using a KLA-Tencor profilometer. In particular, Figure 101 represents the vertical section of the structure, which shows that the groove in the PMMA is 170 nm deep created by UV irradation and photoresist development. Figure 102 shows a three-dimensional reconstruction of the structure in the area where the contact with the gold will be made.

In Figure 104 it is showed the chemical maps of Au, Si and their overlays performed after the lift-off step (step g figure 99). They confirm the formation of the gold structures (on which the SAM will be assembled) on the Si substrate.

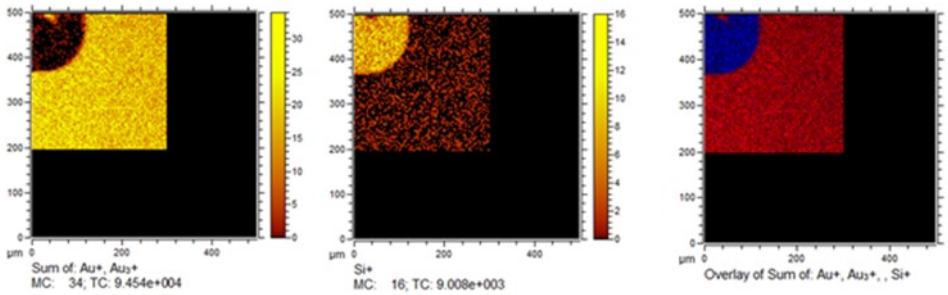

Figure 104: Au+ and Si ToF-SIMS chemical maps

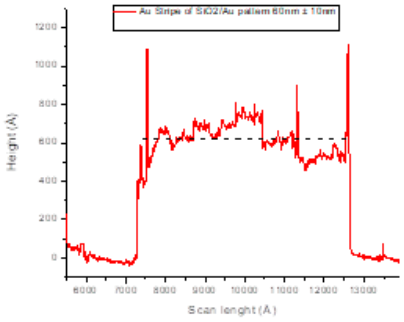

Figure 1045: Profilometer single scan recorded perpendicularly to a gold strip on SiO_2 substrate

Figure 105 represents a track recorded by using profilometer across the thickness of the gold stripe left on the thermal silicon oxide insulating substrate after the step g illustrated in Figure 99. The measured thickness is about 60nm.

Figures 106 and 107 respectively show the ToF-SIMS top view images about different signals relating to two portions large 500umX 500um of gold strips, one subjected to 10 iterations of the assembly procedure based on the Fe (II) DT2 system, while the other subjected to ten iterations of the assembly procedure based on the Ru (II) 2DT3 system.

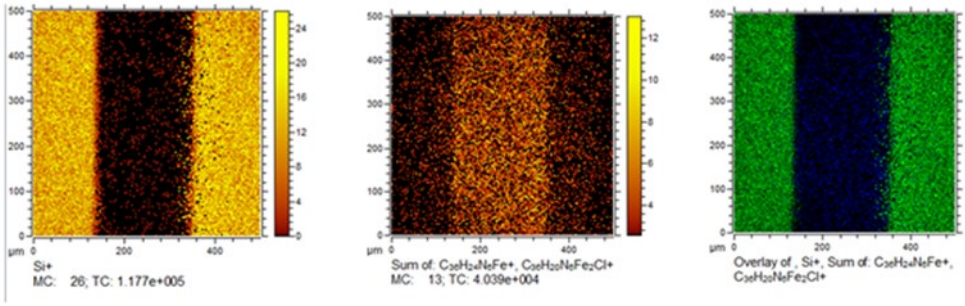

Figure 106 2D ToF-SIMS characterization: chemical maps of signals related to Fe(II)DT2 assembled on gold patterned stripe and related to the silicon oxide substrate.

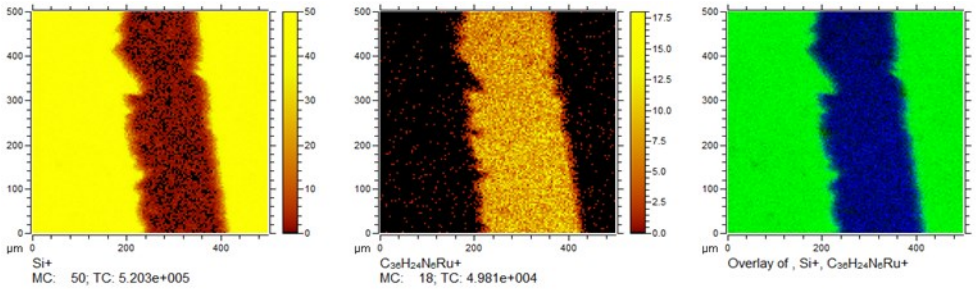

Figure 1057 2D ToF-SIMS characterization: chemical maps of signals related to Ru(II)2DT3 assembled on gold patterned stripe and related to the silicon oxide substrate.

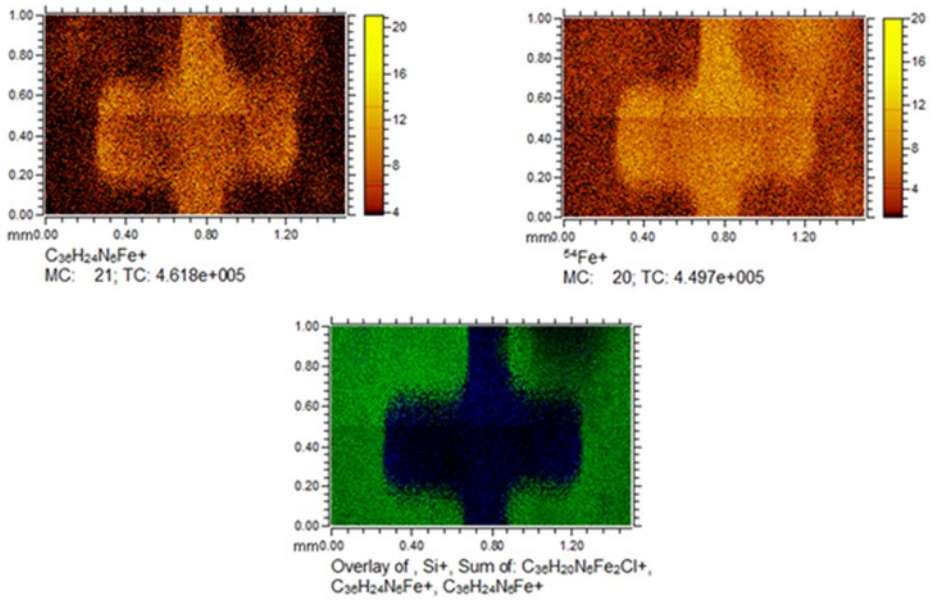

Figure 1068: large area ToF-SIMS images (macroraster) from a region with molecular wires grown on patterned gold substrate. Top left:distribution of a characteristic ion from the wire; Top right: distribution of Fe^+; bottom:overlay of wire-related ions (blue) and silicon substrate signal (green).

Figure 108 shows a ToF-SIMS image obtained from a collage of different images according to the technique referred to as macro raster. In fact, a portion, 2 mm wide and 1 mm high, is represented of a gold sample patterned on silicon oxide on which the growth procedure of the molecular wires based on the Fe-DT units has been iterated 10 times. Also in this case it is possible to note how the intensity of the signals associated with the ionic fragments of the assembled structures appears to be present only on the gold stripes of the pattern. An RGB overlay is therefore shown between the signals relative to the substrate (Si^+) and the sum of signals associated with molecular wire based on Fe-DT units.

10.2 Conclusion.

In this development task of the doctoral project further goals related to the ability to pattern supramolecular systems on surfaces patterned at the micrometric level have been achieved. A strategy based on the production of chips by photolithography made it possible to construct patterned substrates consisting of strips of gold on thermal silicon oxide. The gold strips were selectively functionalized, through thiols and subsequently through the accretion procedures of the supramolecular

assemblies. The functionalization of these was performed by exploiting both the Fe-DT units and the Ru_2-DT_3 units. ToF-SIMS mass spectrometry together with stylus profilometry were two essential tools to follow the different steps involved in the fabrication and functionalization process of the gold-silicon thermal oxide patterned system.

10.3Photocurrent measurement

The experimental prototype adopted to conduct the measurements relating to the photo-conduction properties of the molecular wires is based on a hetero junction. In this hetero junction the self-assembled molecular wires film under examination is interposed between the gold tracks surfaces of the ad hoc designed chip and a transparent micrometric layer of PEDOT, that by softly contacting the MWs allows to generate a manageable contact by using micromanipulator and his electrodes. The photo stimulation of the molecular junction was carried out using two sources: one characterized by an almost continuous visible emission spectrum, the other characterized by emissions in the range of the UV radiations. A sketch of the experimental system used to study molecular heterojunction is shown in Figure 109.

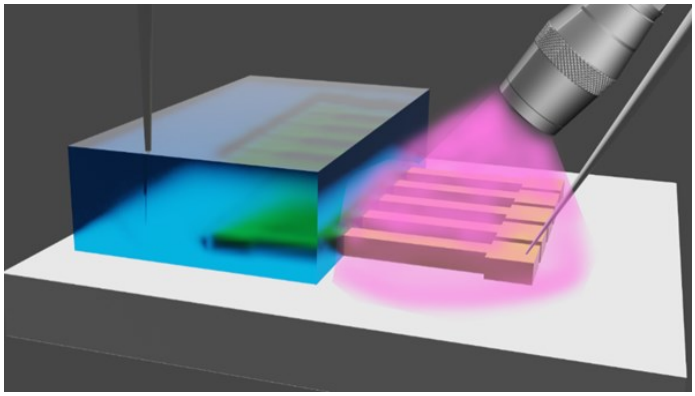

Figure 10709. Sketch of the experimental prototype: The thermal silicon oxide substrate is represented in white, the gold tracks on which the molecular wires are assembled are represented in yellow, in blue it is represented. the micrometric transparent layer of PEDOT, the terminal part of the optical fiber and the electrodes of the micromanipulator are easily identifiable.

In this sequence of materials, evaluating the high relative electrical conductivities of gold and PEDOT, the molecular layer is the one that, having a very high theoretical resistance, modulates the electrical characteristics of the entire measurement set-up adopted.

Figure 110 reports the I-V behavior – both in dark and under illumination - of the chip system, fabricated as previously described, containing molecular wires with 10 $Ru(II)_2DT_3$ units, corresponding to 30 metal centers in total (10 couples of Ru centers plus 10 interconnecting Fe centers). The figure reports, in sequence, ten I-V characteristics obtained by varying the potential from 0 V to 1 V and back to 0 V in steps of 1mV per microsecond and repeating the cycle ten times. A single cycle is represented by 100 data points (row number) in the x-axis of Figure 110.

Measurements were performed by using a Keysight B2981BTM femtoamperometer. The black curve was obtained in absence of illumination (dark conditions) while the red one was measured under photo-stimulation with a continuous spectrum light source.

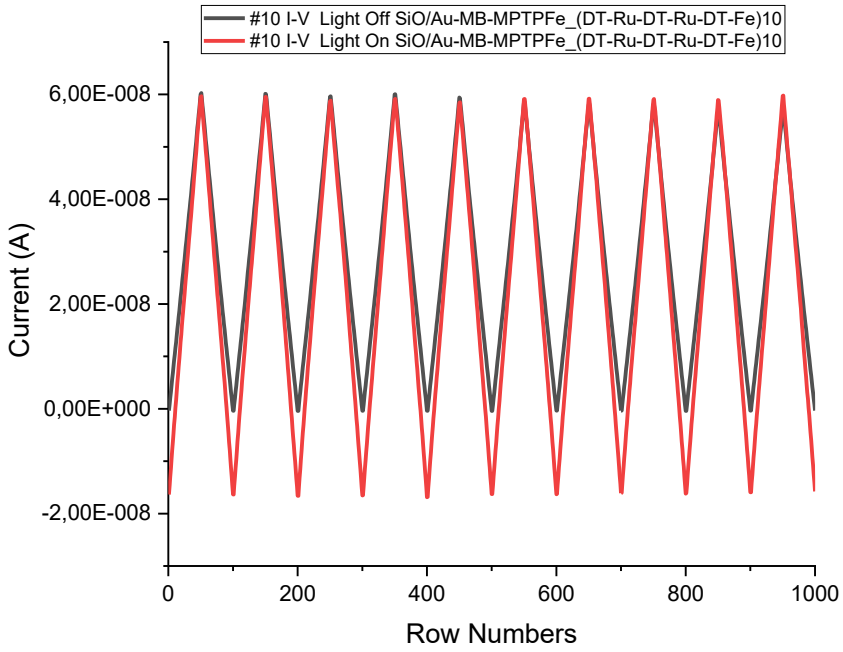

Figure 10810 Sequences of ten I-V characteristics of the heterojunction assembled with 10 Ru(II)$_2$DT$_3$ units. 100 row numbers in the x-axis represent a voltage sweep from 0V to +1V and back to 0V. The curves were acquired under illumination (red line) or in dark condition (black line).

The figure shows that the system behaves in a different way in the low voltage range, corresponding, in the plot, to the minima of both curves. In particular, we observe that under illumination there is a measurable current even at zero applied voltage (not osbserved in dark).

In order to gain a further insight on the origin of the observed photocurrent, we prepared two chip assemblies with two different kinds of molecular wires, one of the same type of that discussed above and another containing iron centers only. The two molecular wires were chosen with the same number of metal centres (15), in order to assure similar wire length. The wires were obtained, respectively, by assembling

five $Ru(II)_2DT_3$ units (alternated with 5 Fe(II)DT units) or fifteen Fe(II)DT units.The choice of shorter wires, compared to those of figure 111, was done in order to increase the measured current values, that are known to decay with wire length, at least in dark conditions.

The electrical behavior of these systems was investigated under different illumination conditions, namely in dark conditions and under photo-stimulation either in the visible or in the UV regions. To such purpose two different light sources were used, namely a continuous spectrum visible light source (commercial RGB led) and a UV source (365nm)

Figure 111 reports the results obtained by applying a constant 0,1V potential to the electrodes and measuring the current while cycling the three external photo-stimulation conditions (dark, visible and UV light).

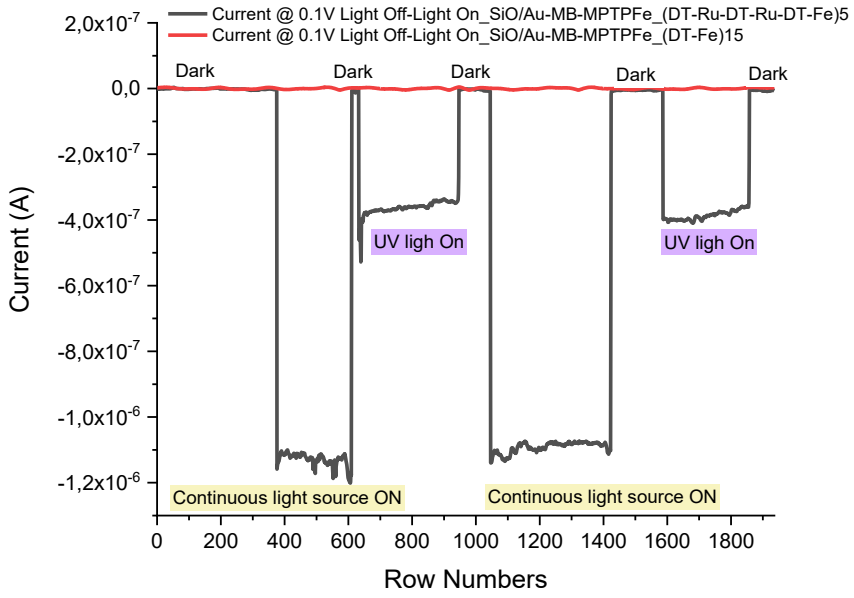

Figure 10911 Current measured at constant applied potential (0.1 V) under different illumination condition for two different 15-metal-centre molecular wires: ruthenium based (black line) and fully iron-based (red line).

In figure 111 it is possible to observe how the electronic properties of the hetero junction obtained by assembling molecular wire based on Fe(II) DT remain unaltered

when the external light stimuli are generated via UV or continuous spectrum light sources.

On the other hand, the effect of the aforementioned sources on the conduction properties of the heterojunction assembled with $Ru(II)_2DT_3$ units is evident.

Indeed, both the two different types of light stimuli generate a current of different magnitude. In both cases this current flows in a direction opposite to the electrodes configuration used to apply the potential.

The activation of the recorded current can be explained according to a conduction mechanism that is focused on the population of the electronic levels of the excited states of the molecular wire based on units of $Ru(II)_2DT_3$. More precisely, it is possible to expect an electron injection phenomenon from the excited states of the organometallic complexes centers present in the structure of the molecular wires based into conduction band of PEDOT. Starting from the above assumption it is therefore possible to speculate on the different magnitude of the photocurrent measured with the different light stimuli.

In the case of the $Ru(II)_2DT_3$ based molecular heterojunction exposed to UV source, the electronic levels mainly associated to ligand portion of the complex are excited and could be moderately involved in a hypothetical photo-redox mechanism attributable to the metal center of the complex. Instead, if the light stimulus is generated by exploiting a continuous spectrum source, the junction is also exposed to radiations of the same energy order of the MLCT typical transitions.

All these phenomena could be involved in the electronic levels matching of the different interfaced materials allowing the charges flow across the heterojunction based on Ru2 molecular wire.

Instead, the "blind" behavior of the Fe(II)DT -based molecular heterojunction and the very responsive behavior of molecular heterojunction based on $Ru(II)_2DT_3$ units can be attributed to kinetic aspect of MLCT electronic transition.

Indeed, it is known that the radiative relaxation times of the MLCT electronic transitions associated to iron-based metal centers are shorter than relaxation times typically associated to complexes based on ruthenium metal centers.

This can be also viewed as competition process between the performance of electrons promotion from the fundamental electronic state of the molecular wire to the excited electronic levels versus the electron injection performance from the excited electronic levels of the molecular wire to electrodes.

In the specific case of heterojunction assembled using molecular wire based on $Ru(II)_2DT_3$ units, the excitation and charge injection processes have an overall better performance than the system based on Fe(II)DT.

10.4 Conclusion

In this development task of the PhD project, further goals were achieved relating to the ability to develop an experimental set up capable of testing the electrical conduction properties of molecular wire arrays assembled using Fe-DT and Ru2-DT3 based units in condition of. Specifically, it was possible to create a hetero junction in which a two-dimensional array of molecular wire is sandwiched between two highly conductive materials. These junctions were electrically characterized in three exposure conditions: exposure to continuous spectrum light source, exposure to UV light source and dark condition. The junction based on the assembly of a Ru2DT3 unit showed, both in the case of characterization IV and in the case of the constant culture "light cycles", the tendency to lower the measured current intensity. Completely unrelated to the experimental conditions (continuous source and / or UV source), the junction based on the assembly of molecular wire made up of Fe-DT units appeared.

11 ToF-SIMS DEPTH PROFILING CHARACTERIZATION OF NANO-HYBRID SYSTEMS

11.1 ToF-SIMS depth profiling of supramolecular structure based on terpyridine-iron and terpyridine-ruthenium metallorganic complexes.

In this part of the PhD project, I dealt with the characterization by ToF-SIMS depth profiling of supramolecular systems assembled on silicon oxide using ruthenium and iron based polytherpyridine complexes. This task was developed within the scientific collaboration between IMEC (Leuven-Belgium) and the University of Catania. At the IMEC facilities, thanks to the use of ToF-SIMS (ION-TOF V) tool, it was possible to explore the limit conditions in terms of energy indicated as shallow depth profiling.

Specifically, two different types of supramolecular structures were characterized: one is made of Fe(II)-bis-terpyridine ligands, the second is a bimetallic 3D-assembly made of Fe(II) and Ru(II) bis-terpyridine ligands. Actually, the Ru-based building block was made of 3 Ru(II) centers whole coordinated by the DT(indicated as Ru3).

If the DT system is used, the resulting sequence of ions is based exclusively on iron ions, while in the case of the system indicated as Ru3 the nominal assembly sequence provides for the periodic alternation of 3 ruthenium ions and one iron ion. In both systems the basic functional units, that is the ligand that coordinates either iron or ruthenium, is always the bis terpyridine system indicated as DT.

In order to evaluate the three-dimensional characteristics of the supramolecular structures indicated as molecular wires, samples having a nominal number of different ion sequences were prepared.

In this specific section of the thesis work it is important to understand what is meant by layer. Layer's number is identified by the number of metal centers forming the molecular wires.

The preparation of the samples is similar to the experimental procedure described extensively in the previous chapters. Briefly, a series of silicon substrates were activated by ZP priming procedure, subsequently they were functionalized with a PPTP (phosponic acid with free terpyridine functionalities) SAM, and subsequently the molecular wire growth procedure was integrated using Fe and DT or Fe and Ru3 according to step wise methodology.

Two series of samples with equivalent number of layers were prepared using the two different build blocks. As regards the Fe-DT system, 3 samples were prepared on which the assembly procedure was iterated 10, 20 and 30 times respectively. In the case of the assembled molecular wire film using the bisterpyridine ligand with coordination of the iron ion, 10, 20, 30 growth iterations correspond to the development of 10, 20, 30 nominal layers.

Differently happens in the case in which the assembly is carried out by assembling the building block indicated as Ru2. Three samples have been prepared on which the assembly procedure has been iterated respectively 3, 6 and 9 times which correspond in this case to a nominal assembly respectively of 9, 18 and 27 layers.

ToF-SIMS depth profiling was used for the characterization of supramolecular systems based on ruthenium and iron based polyterpyridine complexes anchored on silicon substrates.

The experimental conditions used to carry out ToF SIMS all the depth profile reported below are: primary ion Bi3 15 KeV, ~0.4 pA, analysis area 400 um X 400 um, PIID ~1.24E + 13 ions/cm^2, sputter ion Cs, 0.5 KeV ~3 nA, sputter area 800um X800 um, SpIID ~2.7E + 14 ions/cm^2.

Figure 112 shows the ToF-SIMS depth profile of a sample of silicon oxide on the surface of which, through ZP priming, SAM of PPTP, 20 layers of molecular wire have been assembled using the bis-terpyridine ligand indicated with DT as building block and as the coordinating ion the iron ion.

Into figure 112 the signals identified representative of the 20 layer system assembled with iron ions and bis terpyridine ligand are shown (Fe-DT). It is possible to notice how the signals attributable to the fragmentation of the assembled molecular structure (Fe^+ , $FeSO_4^+$, $C_{36}H_{24}N_6FeCl^+$, $C_{36}H_{25}N_6FeO^+$, $C_{36}H_{25}N_6Fe^+$) all decrease (with different slopes depending on their chemical nature) as the signals attributable to the substrate interface such as (Zr^+, P^+, Si^+).

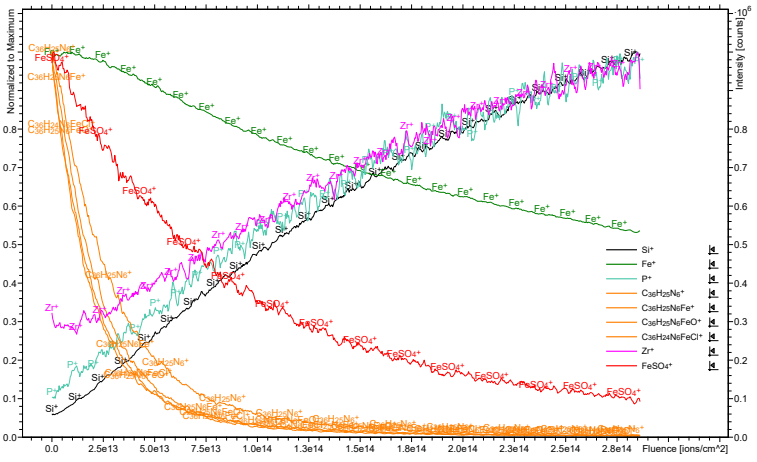

Figure 1102 ToF-SIMS depth profile of supramolecular structure based on Fe-DT complexes

Figure 113 shows a comparison of the portions of spectra recorded under the same experimental ToF-SIMS static modality on three different samples, respectively a sample on which 10 nominal layers of Fe-DT have been assembled, another sample on which 20 have been assembled and another one assembled with 30 nominal layers. It is possible to notice how the intensity of the peak associated with the fragmentation of the molecular wire based on Fe-DT (normalized to the TIC) has a higher intensity in the spectrum recorded by the sample on which they were assembled 30 nominal layers than the spectrum recorded by the sample on which the molecular wire growth procedure was performed 20 and 10 times respectively.

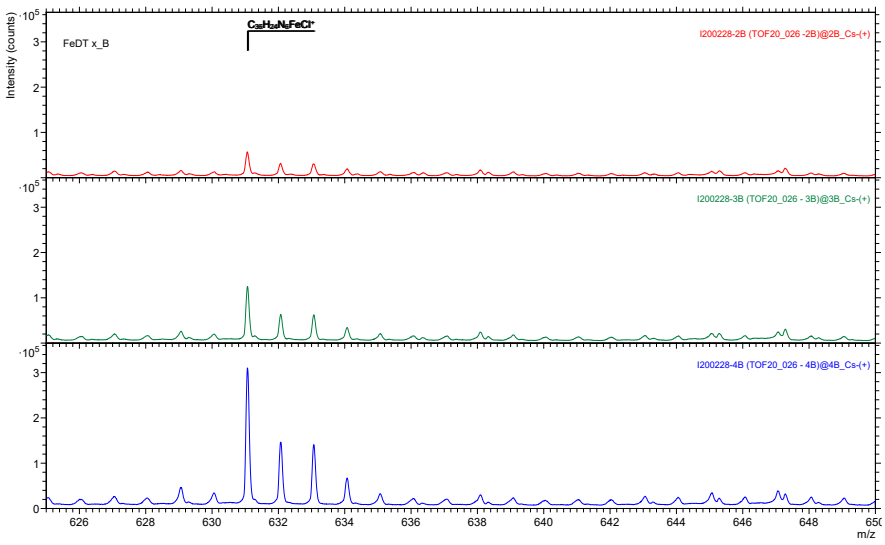

Figure 1113 Comparison of ToF-SIMS static mode mass spectrum portions acquired from 3 different ZP primed silicon samples on which 10 (red line spectra), 20 (green line spectra) and 30 layers of Fe-DT (blue line spectra) have been assembled

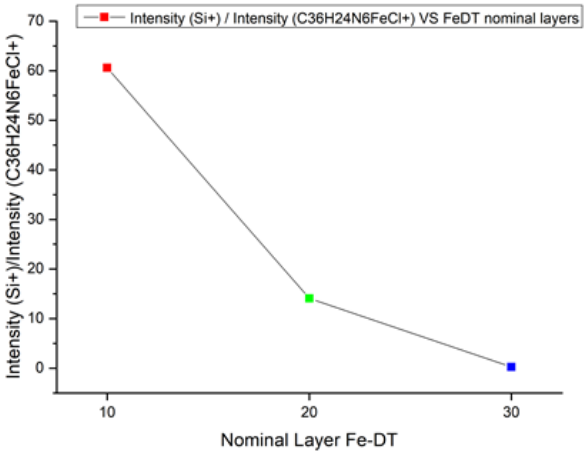

Figure 114

Figure 114 shows the analysis of the signals attributed to molecular Fe-DT structures assembled on silicon ZP primed substrates, iterating 10, 20 and 30 growth procedures. Focusing the attention on the ratio value between areas of mass peaks associated with the Fe-DT structures and areas of mass peaks associated to substrate

(silicon) in each sample, it is possible to notice how this ratio value varies with the number of assembly iteration cycles, respectively (10, 20, 30), with a decreasing trend. This means that the ability to detect substrate-associated ions decreases as the assembly cycles of the Fe-DT system increase.

This behavior can be attributed to the sampling depth of ToF-SIMS static modality technique[110].

Figure 115 shows the ToF-SIMS depth profile of a sample of silicon oxide on the surface of which, via ZP priming, SAM of PPTP, 27 nominal layers of molecular wire have been assembled using Ru2 as building block and as the coordinating ion the iron ion.

Into figure 115 the signals identified representative of the 27 layer system assembled with Ru2 building block and iron ions. It is possible to notice how the signals attributable to the fragmentation of the assembled molecular structure (Ru^+, $CsFe^+$, $C_{36}H_{24}N_6Ru^+$) all decrease (with different slopes depending on their chemical nature) as the signals attributable to the substrate interface such as (Zr^+, P^+, Si^+).

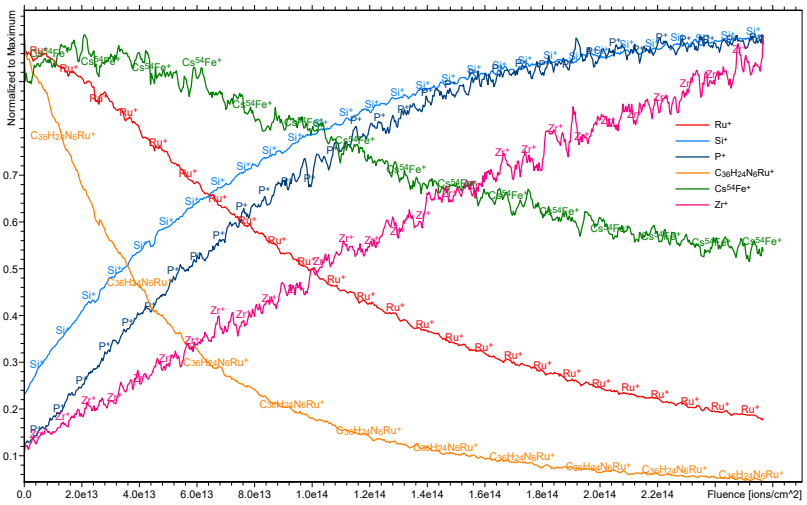

Figure 1125 ToF-SIMS depth profile of supramolecular structure based on Ru_2-DT_3 complexes

The depth of the crater generated by the sputtering process caused by the ToF- SIMS analysis in dynamic mode on silicon substrate functionalization with 27 nominal layers based on Ru2 building block was measured by AFM. Figure 116 shows the AFM trace recorded transversely to the crater in gray, while the related post data treatment used to quantify the dimensions of the crater as best as possible is shown in red.

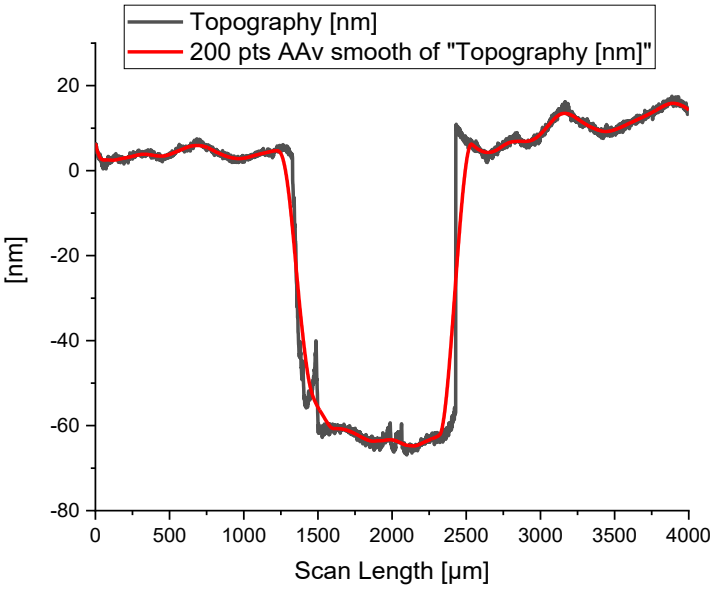

Figure 1136 AFM track recorded transversely to the crater created by the sputter beam during the depth profiling measurement of 27 nominal layer of supramolecular structure assembled by using Ru_2-DT_3 unit.

Some characteristic signals of the samples were therefore studied with more attention to understand if the different nominal number of layers could be correlated to a quantifiable parameter.

For this purpose, the signals related to the substrate of the samples analyzed by ToF-SIMS dept profiling have been studied with greater attention.

Figure 117 shows in overlay view mode the characteristic signals of the substrate (Si^+) acquired from three different samples on which 9 layers (black line), 18 layers

(red line) and 27 layers (blu line) were assembled by using the building block Ru2 respectively. It is possible to note that the fit curve of the experimental data is overlayed on each signal shown in the figure 117.

An exponential fit function (equation 12) was used to fit the experimental signal:

Equation 12

$$y = a - b\left(1 - e^{\frac{-x}{c}}\right)$$

$$f'(x) = \frac{b}{c}\left(e^{\frac{-x}{c}}\right)$$

$$f'(0) = \frac{b}{c}$$

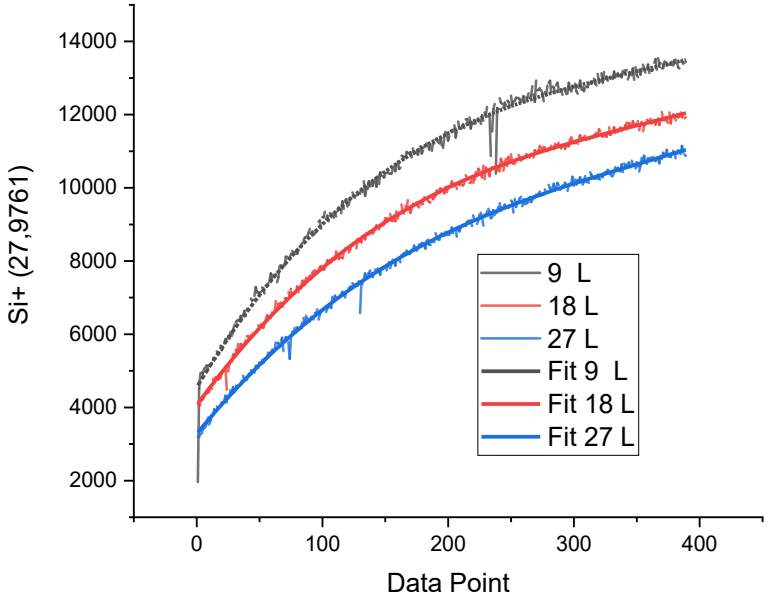

Figure 1147 Signals related to substrate (Si^+) acquired from three different samples on which 9 layers (black line), 18 layers (red line) and 27 layers (blu line) were assembled on silicon substrate.

Figure 118 shows the analysis of the parameters present in the equation used for the fit of the experimental signals acquired via ToF-SIMS depth profile. Specifically,

the values associated with the derivative in 0 (b/c) plotted as a function of the number of nominal layers assembled with the use of Ru2 as building block on silicon. From the trend of these values correlated to the growth rate of the signal relative to the silicon interface, it is possible to note that the sample with fewer nominal layers 9 has a higher slope value than those samples in which 18 and 27 nominal layers have been assembled respectively.

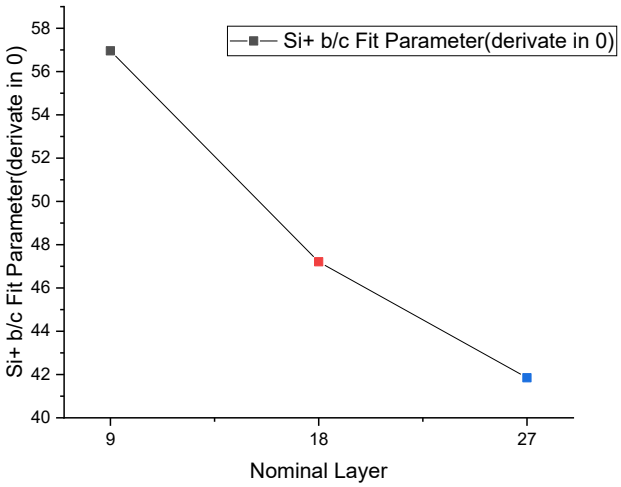

Figure 1158 fit parameter in f'(0)

Figure 119 shows in overlay view mode the characteristic signals of the Cs^+ signal (coming from the ion implantation during the sputtering process by Cs^+ ion beam) acquired from three different samples on which 9 layers (black line) , 18 layers (red line) and 27 layers (blu line) were assembled with the use of the building block Ru2 respectively. It is possible to note a clear exponential trend. Overlay of experimental original data acquired on 18 nominal layers assembled by using Ru2 with fit function it is shown in figure 120.

In this instance, greater attention was paid to the exponential parameter relating to the three fittings performed on the signals relating to the Cs^+ ion.

Indeed, figure 121 shows the parameter of the equation of fit (c) as a function of the nominal number of layers assembled on silicon by using the Ru2 system. the trend of the values of the fit parameter c indicates how the reaching of the value of saturation Cs (steady state condition) This limit condition of sputter process is reached more rapidly on the sample made by 9 layers than to the samples with 18 and 27 nominal layers assembled with Ru2 as building block.

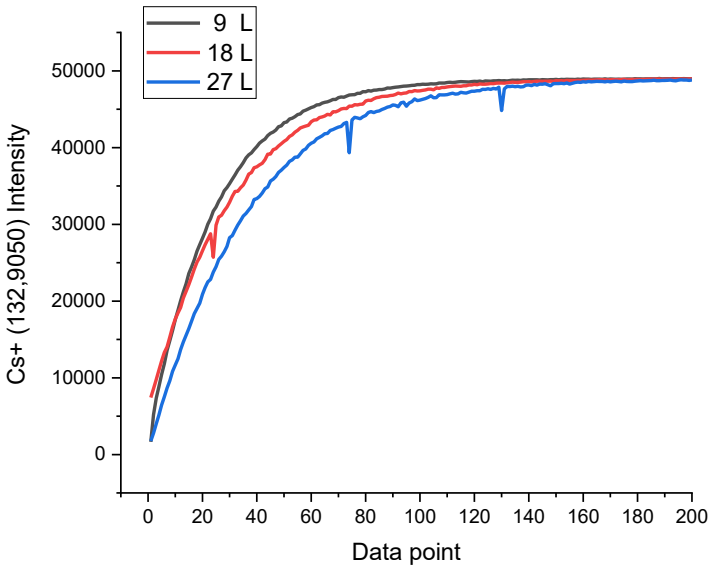

Figure 1169

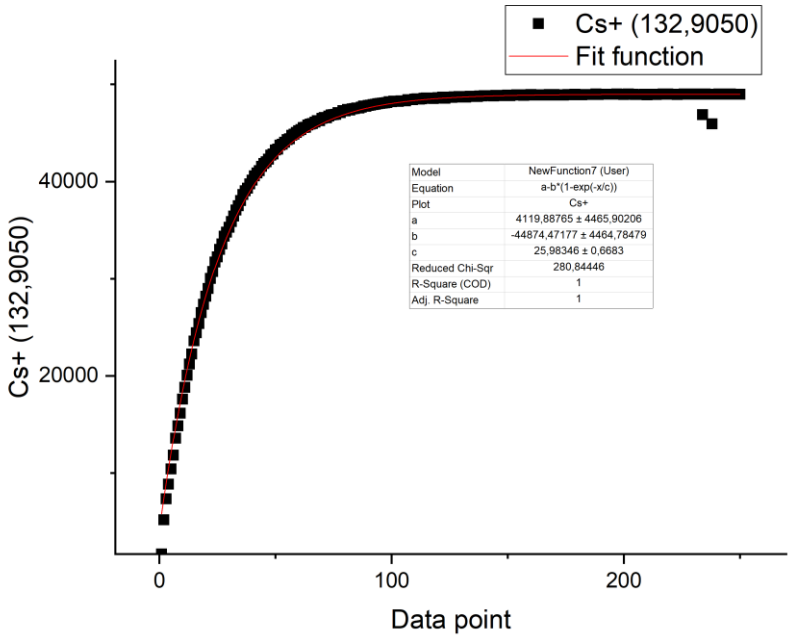

Figure 11720 Overlay of Cs+ experimental signal with exponential fit curve.

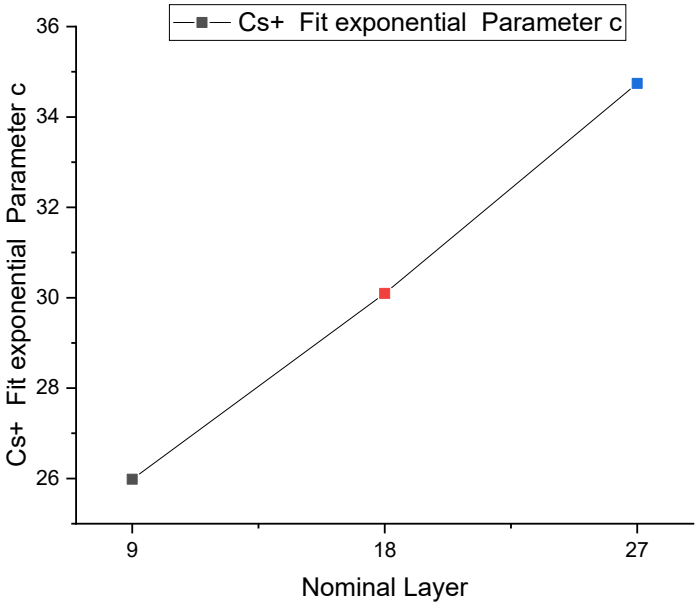

Figure 11821 Exponential parameter (c) of fit curve of Cs^+ experimental data versus nominal layer assembled by using Ru2 as building block.

11.2 Conclusions

The dynamic ToF-SIMS investigation technique has confirmed to be a very useful technique in providing information attributable to the dimensional characteristics of molecular wires based on iron and ruthenium-based polyterpyridine complexes assembled onto inorganic substrates.

ToF-SIMS depth profiling revealed the chemical components characteristic of the supramolecular systems assembled in both cases: i) with ruthenium-based building blocks and in the other case with terpyridine units linked each other exclusively by iron ions. The limit experimental conditions necessary of the technique to investigate the fragmentation properties of these supramolecular structures have once again demonstrated how the use of cesium as a sputter beam can, under the appropriate experimental conditions, be a distinctive tool for the investigation of ultra-thin systems of hybrid nature.

12 ToF-SIMS DEPTH PROFILING OF NANOSTRUCTURED TIO_2 FILMS FUNCTIONALIZED WITH RUTHENIUM METALLORGANIC COMPLEX FOR ECL APPLICATIONS.

12.1 Fabrication of partially functionalized mesoporous TiO_2 electrodes for ECL

In the framework of sensing devices development, the functionalization of tailored mesostructures with Ru(II) complexes can be exploited to build up a platform for the highly sensitive detection of biomolecules such as cancer cells and biomarkers.

This section of the PhD work reports on the results obtained in the manufacturing of nanoporous structure, obtained by a bottom-up approach, functionalized with Ru(II) bipyridine and terpyridine complexes. The final goal is the development of a device for sensing tumor targets by ECL. Our research team was involved in development of experimental strategies useful to fabricate mesoporous TiO_2 electrode, functionalize them by priming procedure in order to control the anchoring of ruthenium-based metal organic complexes along the thickness (z direction),

To achieve this goal, we exploited the ZP priming approach to anchor the ruthenium-based dye on the TiO_2 mesoporous layer and the ToF-SIMS dept-profiling to analyze in depth the functionalized system respectively from a compositional and morphological point of view.

The nanostructured titanium dioxide substrates were realized by doctor blade technique on FTO (fluorine tin oxide) substrates. FTO coated glass substrates were cleaned by UV-O_3 treatment, in order to remove organic contaminant. A 50 µm TiO_2 paste (Solaronix HT) film was deposited by doctor blade technique through a mask, leaving a patterned layer. The sample have been first heated at 100°C for 20 minutes in order to allow the solvent to evaporate, then annealed in air at 500°C for 1 hour in order to carbonize and burn the organic component of the TiO_2 paste, leaving a nanoporous TiO_2 film on the surface.

Figure 122 shows the profilometer single scans (KLA-tencor P7 stylus profilometer) carried out on the middle sections of the nanostructured titanium oxide spots deposited.

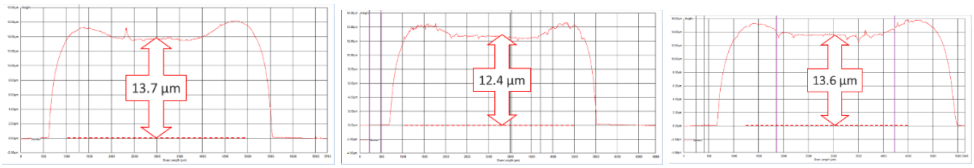

Figure 122

It can be noted that the thickness of the different systems is constant within a wide central area of the spot with a thickness of around ten microns.

The ZP priming procedure extensively described in the previous paragraphs of this thesis has been adapted to treat nanostructured titanium oxide substrates. The procedure is shown below in all its different steps.

It can be noted that the thickness of the different systems is constant within a wide central area of the spot with a thickness of around ten microns.

The ZP priming procedure already described in the previous paragraphs of this thesis has been adapted to treat nanostructured titanium oxide substrates. Figure 123 shows the optical images recorded before and after the post annealing treatment relating to the surface of the micrometric titanium oxide film.

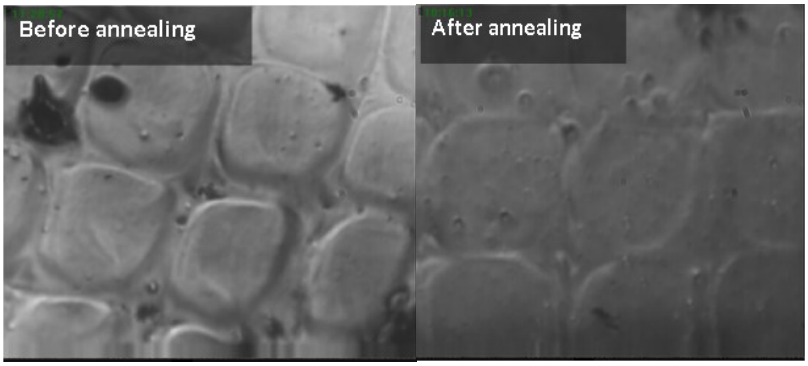

Figure 1193 optical images related to thermal annealing effect on surfaces TiO_2 micrometric film

Initially, the substrates are immersed in a beaker containing boiling ethyl alcohol and rinsed numerous times. Subsequently the samples are exposed to a UV-O_3 treatment for 2 hours. At the end of this treatment, they are immersed in Milliq TM water and dried with the support of nitrogen flow and heating on a plate. The perfectly dried

samples are then immersed for 2 hours in a beaker containing pure phosphorus oxychloride ($POCl_3$), which provides for the phosphorylation of the hydroxyl groups present in the surface of the titanium oxide nanostructures. It is then washed in water to remove traces of phosphorus oxychloride. The samples are then immersed for 1 hour in a 1:1 water:ethanol solution with a concentration equal to 10^{-4} M of zirconyl chloride.

Before the step of functionalization of the substrates via ruthenium-based complexes, the samples are primed with solvents in which the acid and the ruthenium phosphonate complex to be used is solubilized.

A phosphonate derivative of an organometallic complex was employed in the development of this part of the project. This organic system indicated in figure 124 was synthesized by the research group of the CNR of Milan which refers to Alberto Bossi as member of the PRIN 2017 project.

Initially, the substrates are exposed to a UV-O_3 treatment for 30 minutes. At the end of this treatment, they are immersed in Milliq TM water and dried with the support of nitrogen flow and heat. Then the samples were immersed in pure phosphorus oxychloride ($POCl_3$) for 2 hours, to induce the phosphorylation reaction of the hydroxyl groups present in the surface of the titanium oxide nanostructures. After the treatment with $POCl_3$, the samples were washed vigorously in water to remove traces of phosphorus oxychloride.

The samples are then kept immersed for 1 hour in a 10^{-4} M 1:1 water: ethanol solution of zirconyl chloride.

Before the step of functionalization of the substrates via ruthenium-based complexes, the samples are primed with solvents in which the acid and the ruthenium phosphonate complex to be used is solubilized, in order to promote the diffusion regime of Ru complex. Then they were kept immersed in a $5 \cdot 10^{-4}$ M solution of (ruthenium(II)bis(2,2 0 -bipyridine)([2,2 0-bipyridine]-4,4 0 -diylbis(phosphonic acid) hexafluorophosphate indicated as MP118. The MP118 Ru complex was synthetized by the CNR of Milan, in the group of Dr. Alberto Bossi. The molecular structure is depicted in figure 124

Since the final goal is to functionalize only a part of the thickness of the titanium dioxide film, several tests have been carried out at different immersion times, in order to find the conditions in which a gap of 2 to 5 microns of non-functionalized TiO_2 remains between the FTO layer and the functionalized TiO_2 layer (see figure 127).

This gap will act as a reservoir of the co-reagent for ECL experiments.

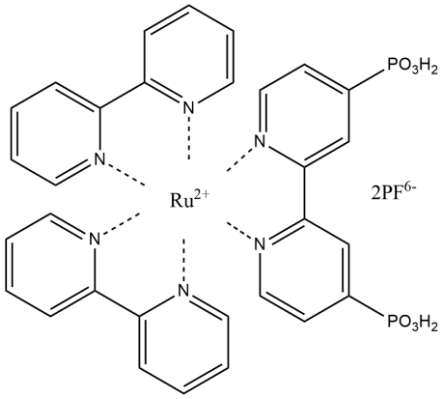

Figure 1204 molecular structure of MP118 metallorganic complex

The MP118 Ru complex TOF-SIMS spectrum was acquired on silicon surface. was characterized by ToF-SIMS in static mode. Figure 125 shows the portion of the spectrum in which the distributions of peaks relative to the ions $C_{10}H_7N_2Ru^+$ (~256.24 m/z), $C_{11}H_7N_2Ru^+$ (~268.25 m/z) and $C_{10}H_7N_2RuO^+$ (~272.24 m/z) have been assigned. Figure 126 shows a spectrum in which the signal attributed to $C_{20}H_8N_2RuO_2H_2^+$ ion was detected. These peaks are referred to the most characteristic signal of the MP118 molecule within the ToF-SIMS spectrum.

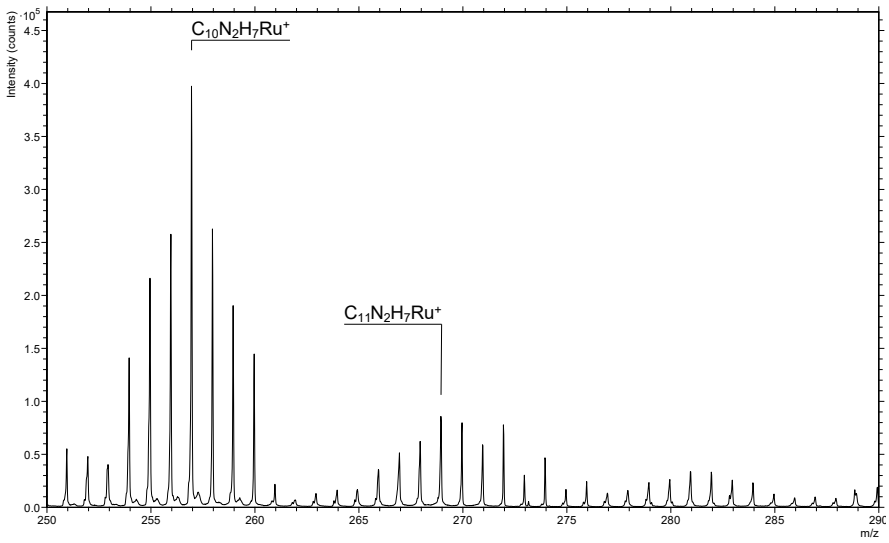

Figure 1215

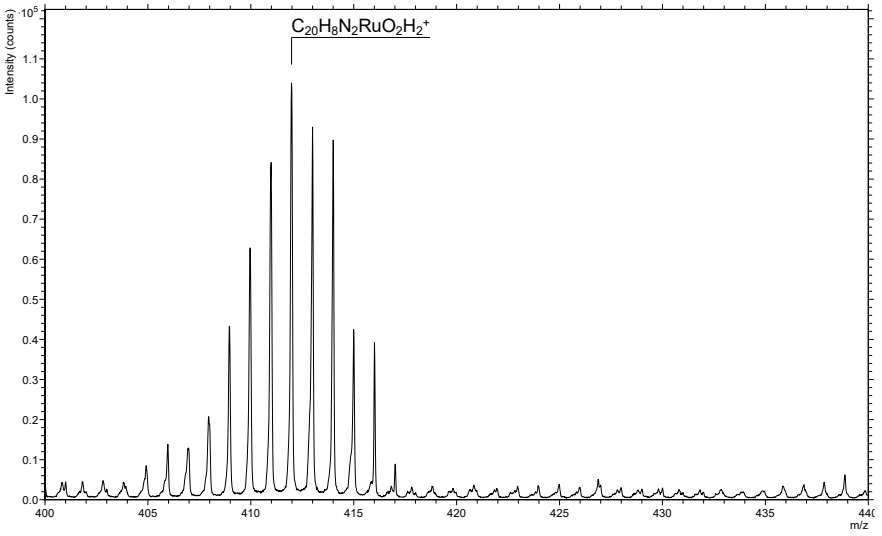

Figure 1226

ToF-SIMS depth profiles have been acquired on the MP118 partially functionalized TiO_2 films. In ToF-SIMS depth profiling analysis, a dual-beam operation performed by a sputtering and an analysis beam is typically used. The analysis beam is usually optimized for collecting high resolution mass spectra, and the sputtering beam is

optimized for high sputter rate, optimum depth resolution, and optimum ionization yield. ToF-SIMS depth profiles have been acquired in the so-called “non-interlaced mode”, in which the sputtering phases (typically, several seconds each) and the analysis phases (several seconds each) are separated, and charge compensation time slots (if necessary) are added in between.

ToF-SIMS depth profiling was performed by a ToF-SIMS IV (ION-TOF GmbH) by using a 25 keV Bi^+ primary ion beam for analysis (ion current 1.5 pA, raster size 60x60 μm^2) and a 10 keV Cs^+ ion beam for sputtering (25 nA, 80x80 μm^2). In order to remove crater edge effect due to a possible slight misalignment between the sputter beam and the analysis beam, a reconstruction of the profile have been performed by software selecting the bottom of the sputtering crater as region of interest (ROI).

The crater depths have been measured by means of a KLA-Tencor P7 stylus profilometer.

As already mentioned, the anchoring step of MP118 Ru complex is done experimentally by the immersion of the samples primed by ZP procedure in a 1 10^{-4} M solution of MP118. The immersion time was evaluated for each sample, due to de fact that the samples have a thickness inconstancy, in order to achieve a better control on the functionalization depth of the nanostructure. The need to control the functionalization along the depth of the nanostructured titanium oxide substrate derives from the fact that the ECL emission tests should give better results if the conductive layer (FTO interface) is no more than 4-5 microns away from the functionalized TiO_2 interface. In other words, the dimensional gap of non-functionalized titanium oxide must be no more than 4-5 microns large to observe the phenomenon of electro chemo luminescence. The maximum dimensions of this gap depend on the electrical and optical properties of the material since the processes underlying the ECL are charge transfers and radiative relaxations. The schematization of the prototype which was partially functionalized with Ruthenium based metalorganic complex across the micrometric nanostructured TiO_2 ZP-primed film thickness is shown in figure 127.

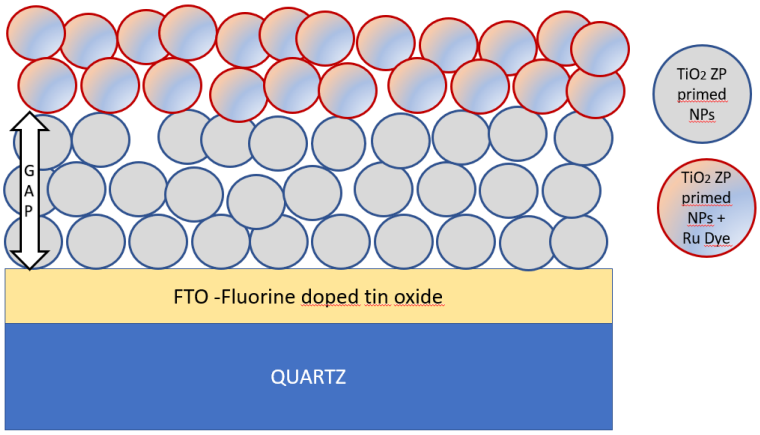

Figure 1237 Sketch of partially functionalized nanostructured electrodes of TiO_2

Figure 128 shows a ToF-SIMS depth profile of a ZP primed TiO_2 substrate. The ZrO^- signal was used to monitor Zr impregnation and SnO_2^- was used to individuate the interface TiO_2/FTO. It is clearly visible that the whole TiO_2 film has been primed with Zirconium phosphonate functional groups.

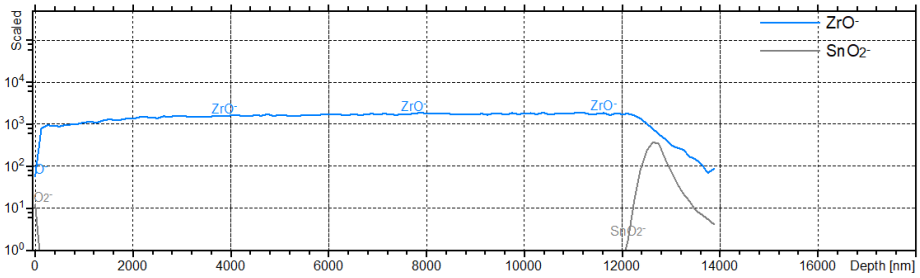

Figure 1248: ToF-SIMS depth profile acquired on ZP primed and post annealed TiO_2 nanostructured micrometric film

Figure 129 shows the ToF-SIMS depth profile of a ZP primed nanostructured TiO_2 sample subjected to a MP118 partial impregnation.

The Ru^- and CN^- signals are attributed to the MP118 molecule, the ZrO^- signal is attribute to ZP priming and PO^- is coming both from zirconium phosphonate and MP118 molecule. The signals attributable to the ruthenium-based organic metal complex (Ru-, CN-) exponentially decrease their intensity at a sampling depth of about 1,6 micron, the signals relating to the priming process (PO^- ZrO^-), together with the TiO_2 signal, exponentially decrease at the TiO_2/FTO interface, where the SnO_2F^- signal increases. The PO^- signal, common to both ZP priming and MP118 molecule, shows a slight decrease at the interface between MP118 primed TiO_2 and not primed TiO_2.

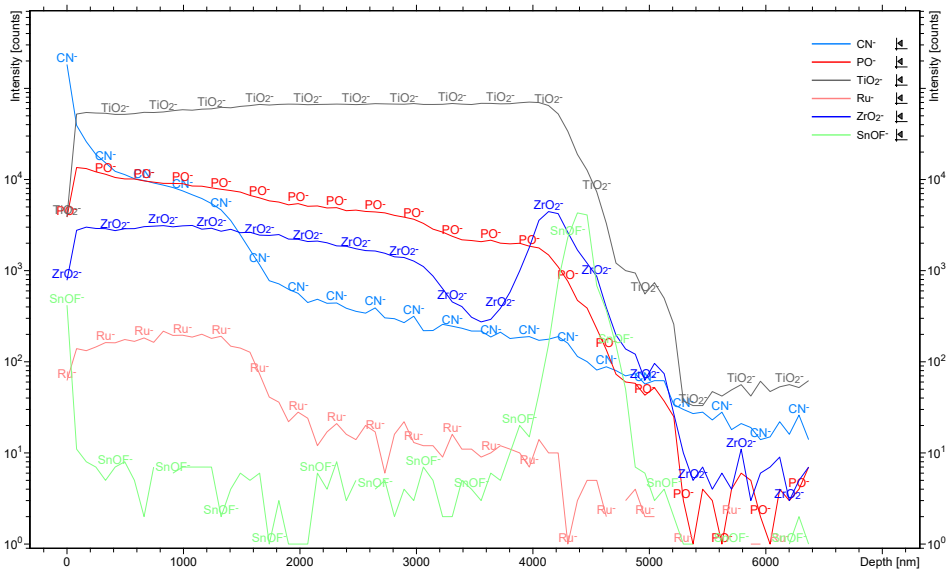

Figure 1259: ToF-SIMS depth profile of a ZP primed nanostructured TiO_2 sample, partially impregnated with MP118.

Figure 130 and Figure 131 respectively show the measurements performed using the profilometer after the ToF-SIMS analysis in dynamic mode. Specifically, a figure (131) is shown, a trace recorded transversely to the crater generated by the sputtering process. Figure 132 instead shows a three-dimensional reconstruction of the crater shape generated by the sputtering process associated with the ToF-SIMS measurement in dynamic mode.

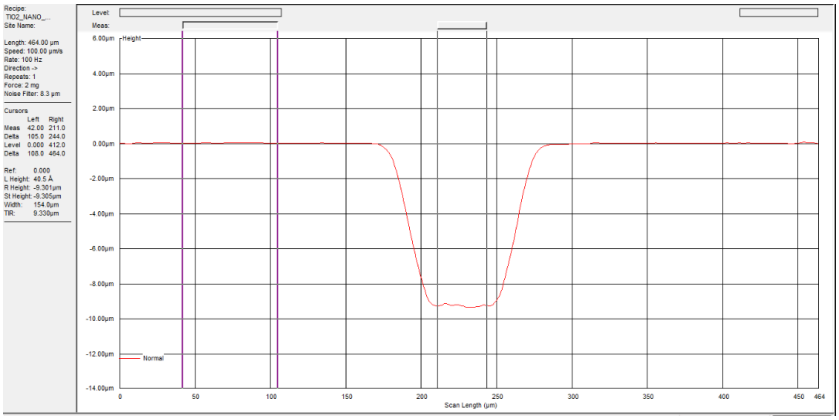

Figure 130 Profilometer evaluation of crater depth generated by sputtering process associated to dynamic ToF-SIMS measurement.

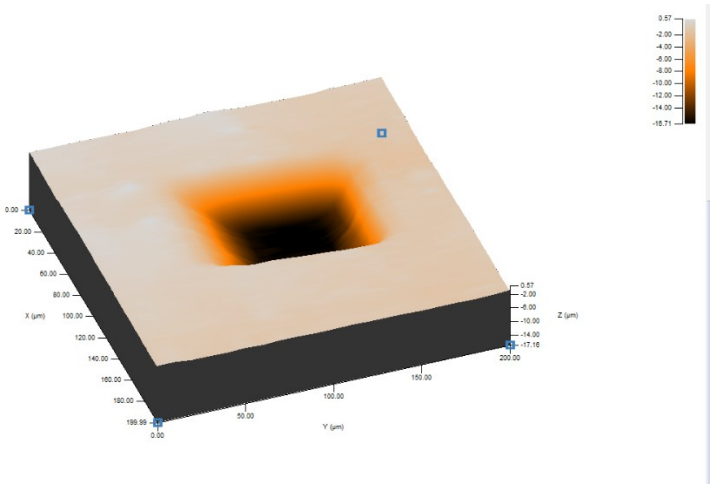

Figure 131 Profilometer 3D image reconstruction to evaluate the shape of crater depth generated by sputtering process associated to dynamic ToF-SIMS measurement

The study carried out on the MP118 impregnation processes made it possible to identify the process time scales related to priming and the time scales of the processes related to the anchoring of the organometallic system MP118. Aware of the permeation-functionalization speed of the complex within the nanostructured

system, it was therefore possible to prepare nanostructured tin oxide samples with a non-functionalized gap ranging from 5 to 3 microns functional to the ECL process.

The three images (Figures 132-134) below show three ToF SIMS depth profiles related to three different samples, on which a ZP functionalization was carried out along the entire thickness of the sample while the anchoring of the MP118 complex was timed in order to leave from 5 to 3 microns gap not functionalized. For the sake of simplicity, only Ru^- and SnO_2F^- lines have been reported.

The depth profiles shown below refer to impregnation times of 5 hours, 6.5 hours and 7 hours respectively.

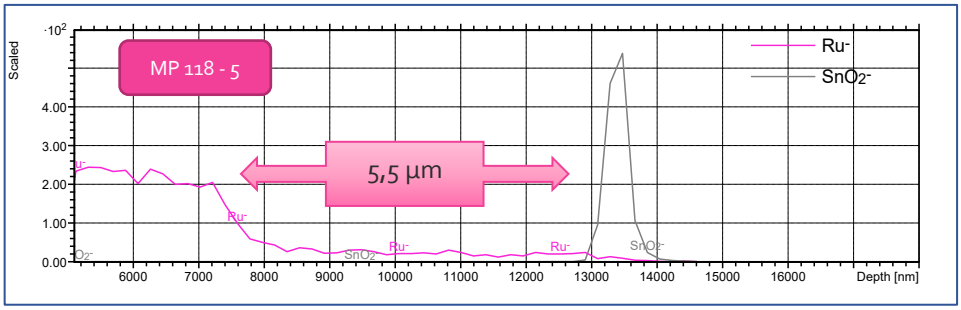

Figure 132

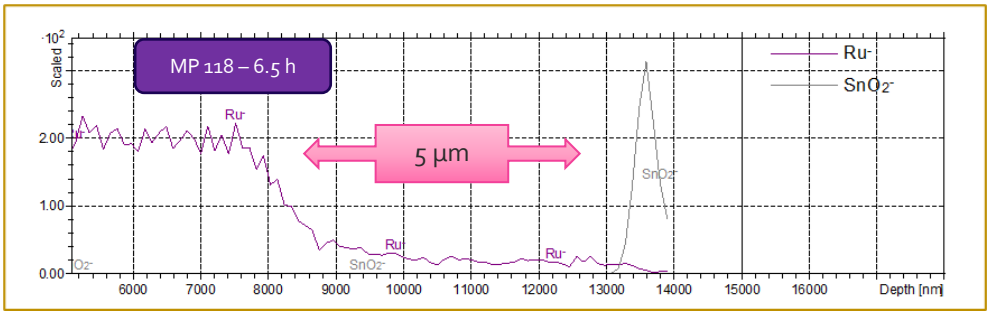

Figure 1263

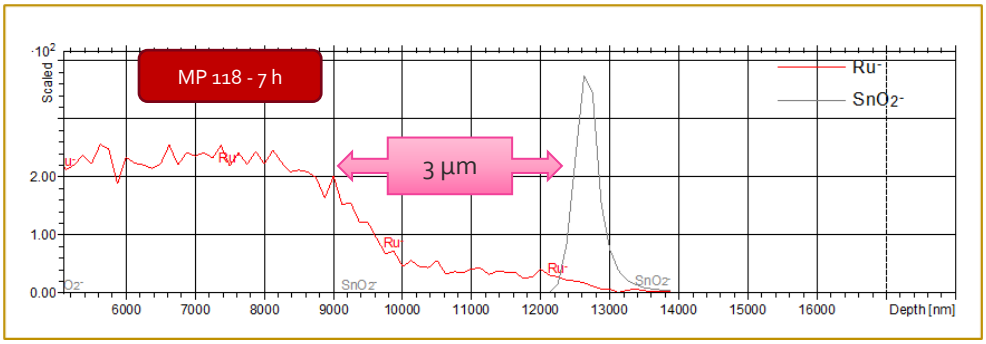

Figure 1274

13 ECL ELECTROD PROTOTYPE MEASUREMENT TEST.

Although in the last few years many ECL systems were proposed, the oxidative reduction strategy based on the tris(2,2'- bipyridine) ruthenium (II) $[Ru(bpy)_3]^{2+}$ as emitter and tripropylamine (TPrA) as sacrificial coreactant is the only one that have a real commercial application. In this case the general mechanism involves the oxidation of both emitter and coreactant as shown in Figure 135a.

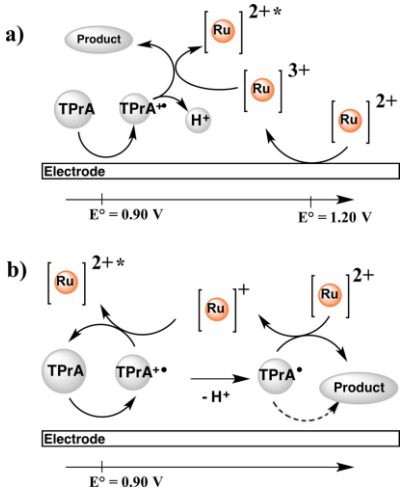

Figure 1285: ECL mechanisms for the couple $Ru(bpy)_3^{2+}$/TPrA: a) both luminophore and coreactant are oxidized in the "oxidative-reduction" mechanism; b) ECL generation obtained only by TPrA oxidation and involving the homogeneous reaction of the radical cation ($TPrAC^+$).

The luminophore in the excited state Ru2+* relaxes to the ground state and emits photon. All these systems based on the $Ru(bpy)_3^{2+}$/TPrA couple need the oxidation of both chemical species, while in the common immunoassay, the $Ru(bpy)_3^{2+}$ is not directly oxidized because it is used as an ECL label attached to the bead and therefore not free to diffuse toward the electrode. Bard and co-workers demonstrated how ECL emission could be obtained only from the oxidation of TPrA, in a mechanism involving both TPrAC and TPrAC+ (Figure 135 b). A crucial point in the efficiency of the ECL generation is the chemical and physical state and behavior of the electrode surface where the ECL process is initiated. In fact, one of the key steps for the optimization of the signal-to-noise ratio is the coreactant heterogeneous electron transfer reaction. In particular, TPrA-based ECL is driven by this reaction and thus strictly depends on the kinetics of the heterogeneous electron transfer that largely differs for different electrode materials. It is well known that the electrode surface

may change its interfacial behavior during the potential ramp used in the ECL generation and this might dramatically affect the efficiency of the emission intensity. In fact the electrode surface propriety might also affect the lifetime of $TPrAC^{+}$ and its deprotonation reaction kinetics, thus generating free radicals, TPrAC, closer to the electrode surface and increasing the contribution of the oxidative consumption. Moreover, surface modification by the adsorption of intermediates, such as radical cation or coreactant by-products, are known to poison the electrode surface. This effect might decrease the ECL intensity and modify the stability of the electrode after repeated emission cycles.

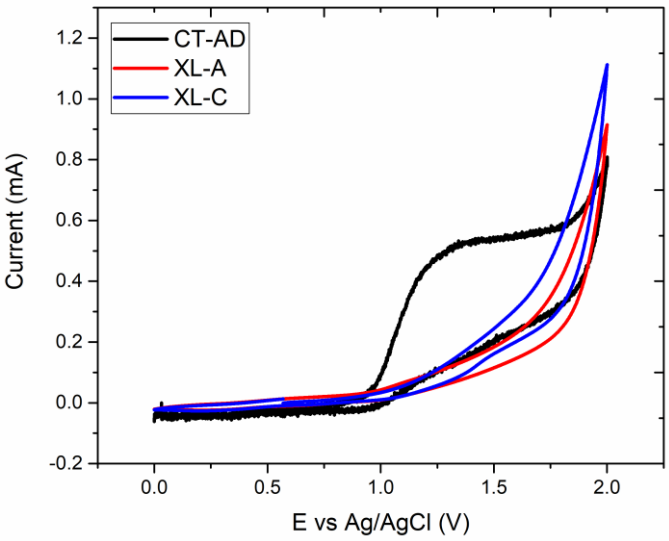

Figure 136 Electrochemical response Current vs Potential of three different working electrodes. Reference electrode: Ag/AgCl; Counter electrode: Platinum wire. In PB 0.2M/TPA 180mM, pH 6.78.

In figure 136 is presented the electrochemical response of three different electrodes with in a solution of PB 0.2M/ TPA 180mM versus a reference electrode Ag/AgCl (V) and in a scan rate of 0.1V/s. The oxidation reaction of TPA in the case of the CT-AD electrode starts around 0.85V according to the mechanism of the figure 88. Then, a sharp peak is presented of 1.2 V according to the oxidation of the immobilized ruthenium in the surface of TiO_2. These two oxidation reactions heled on simultaneously in our system. On the other hand, with the blue and red line are presented the anodic biases of XL-A and XL-C but the peak of Ru oxidation is not

presented clearly. This electrochemical behavior is presented according to the oxidation of TPA instead the ruthenium complex is immobilized in 3-5μm to the surface of the electrode.

Conclusion

It was possible to develop an experimental procedure for the production of micrometric thickness films made of nanostructured titanium oxide. The investigations carried out by profilometry in the early stages of development were essential to morphologically characterize the spot deposited on conductive substrates of FTO. A functionalization procedure (ZP-priming) was adapted to nanostructured three-dimensional inorganic systems. The temporal parameters relating to the priming steps and the chemisorption step of the terpyridine phosphonate complex were studied by ToF-SIMS investigation in dynamic modality and by profilometry measurements. It was possible to have control, in the margins of the critical issues relating to the channeling problems of the solutions within the micrometric film of titanium oxide relating to the functionalization-chemisorption steps, on the depth of penetration of the functionalization processes. In fact, micrometric films of nanostructured titanium oxide were prepared and characterized within which it was possible to keep a gap non-functionalized (from 5 to 3 microns between the last front of the functionalized film and the interface with the FTO substrate.

ECL assays were performed on some of these substrates to evaluate the characteristics of the radiative process. The results of ECL assay test suggest a correlation between the non-functionalized gap of the nanostructured titanium oxide micrometric film with two different characteristics associated mechanisms of production of the ECL radiative phenomenon.

14 REFERENCES

1. Badjic, J. D. *et al.* Operating molecular elevators. *J. Am. Chem. Soc.* (2006) doi:10.1021/ja0543954.

2. Joachim, C. & Rapenne, G. Molecule concept nanocars: Chassis, wheels, and motors? *ACS Nano* vol. 7 11–14 (2013).

3. Ma, X. & Tian, H. Stimuli-responsive supramolecular polymers in aqueous solution. *Acc. Chem. Res.* (2014) doi:10.1021/ar500033n.

4. Arole, V. M. & Munde, S. V. Fabrication of Nanomaterials By Top-Down and Bottom-Up Approaches-an Overview. *JAASTMaterial Sci. (Special Issue* **1**, 2–89 (2014).

5. Mendiratta, S., Usman, M. & Lu, K. L. Expanding the dimensions of metal–organic framework research towards dielectrics. *Coord. Chem. Rev.* **360**, 77–91 (2018).

6. Xi, N. & Li, W. J. Editorial recent development in nanoscale manipulation and assembly. *IEEE Trans. Autom. Sci. Eng.* **3**, 194–198 (2006).

7. Colton, R. J. Nanoscale measurements and manipulation. *J. Vac. Sci. Technol. B Microelectron. Nanom. Struct.* **22**, 1609 (2004).

8. Shang, Y., Hasan, K., Ahammed, G. J., Li, M. & Yin, H. Shang-2019-Applications of nanotechnology https://doi.org/10.1186/s12951-021-01176-w. *Molecules* **24**, (2019).

9. Prasad, R. D. *et al.* A Review on Concept of Nanotechnology in Veterinary Medicine. *ES Food Agrofor.* 28–60 (2021) doi:10.30919/esfaf481.

10. Abiodun Solanke, I., Ajayi, D. & Arigbede, A. Nanotechnology and its application in dentistry. *Ann. Med. Health Sci. Res.* **4**, 171 (2014).

11. Sosa-Vargas, L., Kim, E. & Attias, A. J. Beyond 'decorative' 2D supramolecular self-assembly: Strategies towards functional surfaces for nanotechnology. *Mater. Horizons* **4**, 570–583 (2017).

12. Lohr, A., Lysetska, M. & Würthner, F. Supramolecular stereomutation in kinetic and thermodynamic self-assembly of helical merocyanine dye nanorods. *Angew. Chemie - Int. Ed.* **44**, 5071–5074 (2005).

13. Ulman, A. Formation and Structure of Self-Assembled Monolayers. *Chem. Rev.* **96**, 1533–1554 (1996).

14. Zeng, X., Xu, G., Gao, Y. & An, Y. Surface wettability of (3-

Aminopropyl)triethoxysilane self-assembled Monolayers. *J. Phys. Chem. B* **115**, 450–454 (2011).

15. Chechik, B. V., Crooks, R. M. & Stirling, C. J. M. Chechik_et_al-2000 Advanced_Materials 1161–1171 (2000).

16. Fan, F. R. F. *et al.* Determination of the molecular electrical properties of self-assembled monolayers of compounds of interest in molecular electronics. *J. Am. Chem. Soc.* **123**, 2454–2455 (2001).

17. Vericat, C., Vela, M. E., Benitez, G., Carro, P. & Salvarezza, R. C. Self-assembled monolayers of thiols and dithiols on gold: new challenges for a well-known system. *Chem. Soc. Rev.* **39**, 1805–1834 (2010).

18. Rong, H. T. *et al.* On the importance of the headgroup substrate bond in thiol monolayers: A study of biphenyl-based thiols on gold and silver. *Langmuir* **17**, 1582–1593 (2001).

19. Kumar, G. *et al.* Thermodynamics of Alkanethiol Self-Assembled Monolayer Assembly on Pd Surfaces. *Langmuir* **34**, 6346–6357 (2018).

20. Delamarche, E., Michel, B., Biebuyck, H. A. & Gerber, C. Golden interfaces: The surface of self-assembled monolayers. *Adv. Mater.* **8**, 719–729 (1996).

21. Kondoh, H., Kodama, C., Sumida, H. & Nozoye, H. Molecular processes of adsorption and desorption of alkanethiol monolayers on Au(111). *J. Chem. Phys.* **111**, 1175–1184 (1999).

22. Scheres, L., Giesbers, M. & Zuilhof, H. Organic monolayers onto oxide-free silicon with improved surface coverage: Alkynes versus alkenes. *Langmuir* **26**, 4790–4795 (2010).

23. Yu, Y. *et al.* Room temperature hydrosilylation of silicon nanocrystals with bifunctional terminal alkenes. *Langmuir* **29**, 1533–1540 (2013).

24. Sieval, A. B., Vleeming, V., Zuilhof, H. & Sudhölter, E. J. R. Improved method for the preparation of organic monolayers of 1-alkenes on hydrogen-terminated silicon surfaces. *Langmuir* **15**, 8288–8291 (1999).

25. Sun, Q. Y. *et al.* Covalently attached monolayers on crystalline hydrogen-terminated silicon: Extremely mild attachment by visible light. *J. Am. Chem. Soc.* **127**, 2514–2523 (2005).

26. Wang, A., Tang, H., Cao, T., Salley, S. O. & Ng, K. Y. S. In vitro stability study of organosilane self-assemble monolayers and multilayers. *J. Colloid Interface Sci.* **291**, 438–447 (2005).

27. Hagfeldt, A., Boschloo, G., Sun, L., Kloo, L. & Pettersson, H. Dye-Sensitized Solar Cells. 6595–6663 (2010).

28. Bauer, T. *et al.* Phosphonate- and carboxylate-based self-assembled monolayers for organic devices: A theoretical study of surface binding on aluminum oxide with experimental support. *ACS Appl. Mater. Interfaces* **5**, 6073–6080 (2013).

29. Fan, X., Lin, L., L. Dalsin, J. & B. Messersmith, P. Biomimetic Anchor for Surface-Initiated Polymerization from Metal Substrates. *J. Am. Chem. Soc.* **127**, 15843–15847 (2005).

30. Rosso, M. *et al.* Covalent attachment of organic monolayers to silicon carbide surfaces. *Langmuir* **24**, 4007–4012 (2008).

31. Brodard-Severac, F. *et al.* High-field 17O MAS NMR investigation of phosphonic acid monolayers on titania. *Chem. Mater.* **20**, 5191–5196 (2008).

32. Purvis, K. L., Lu, G., Schwartz, J. & Bernasek, S. L. Surface characterization and modification of indium tin oxide in ultrahigh vacuum [4]. *J. Am. Chem. Soc.* **122**, 1808–1809 (2000).

33. Lee, H., J. Kepley, L., Gi. Hong, H. & E. Mallouk, T. Inorganic analogs of Langmuir-Blodgett films: adsorption of ordered zirconium 1,10-decanebisphosphonate multilayers on silicon surfaces. *J. Am. Chem. Soc.* **110**, 618–620 (2002).

34. Bakiamoh, S. B. & Blanchard, G. J. Demonstration of oriented multilayers through asymmetric metal coordination chemistry. *Langmuir* **15**, 6379–6385 (1999).

35. Zhang, S., Chandra, K. L. & Gorman, C. B. Self-assembled monolayers of terminal alkynes on gold. *J. Am. Chem. Soc.* **129**, 4876–4877 (2007).

36. Spampinato, V. *et al.* Functionalization of oxide surfaces by terpyridine phosphonate ligands: Surface reactions and anchoring geometry. *Langmuir* **26**, 8400–8406 (2010).

37. Kanta, A., Sedev, R. & Ralston, J. The formation and stability of self-assembled monolayers of octadecylphosphonic acid on titania. *Colloids Surfaces A Physicochem. Eng. Asp.* **291**, 51–58 (2006).

38. Chen, D. *et al.* An extremely rapid dip-coating method for self-assembly of octadecylphosphonic acid and its thermal stability on an aluminum film. *J. Mater. Chem. C* **2**, 9941–9948 (2014).

39. Gadegaard, N., Chen, X., Rutten, F. J. M. & Alexander, M. R. High-energy electron beam lithography of octadecylphosphonic acid monolayers on aluminum. *Langmuir* **24**, 2057–2063 (2008).

40. Tizazu, G., Adawi, A. M., Leggett, G. J. & Lidzey, D. G. Photopatterning, etching, and derivatization of self-assembled monolayers of phosphonic acids on the native oxide of titanium. *Langmuir* **25**, 10746–10753 (2009).

41. Paz, Y. Self-assembled monolayers and titanium dioxide: From surface patterning to potential applications. *Beilstein J. Nanotechnol.* **2**, 845–861 (2011).

42. Killian, M. S. Organic Modification of TiO_2 and other Metal Oxides with SAMs and Proteins - a Surface Analytical Investigation.Dissertation, Fau Erlangen (2013).

43. Vitale, S. *et al.* ToF-SIMS study of selective anchoring of Ru(tpy) 2 complexes on zirconium-phosphate functionalized oxide surfaces . *J. Vac. Sci. Technol. B* **38**, 032802 (2020).

44. Aviram, A. & Ratner, M. A. Molecular rectifiers. *Chem. Phys. Lett.* **29**, 277–283 (1974).

45. Glotzer, S. C., Vice, S. K., Cummings, P. T. & Head-gordon, M. I Nternational a Ssessment of R Esearch and D Evelopment in S Imulation -B Ased E Ngineering and S Cience. 1–10 (2011).

46. Yaliraki, S. N. & Ratner, M. A. Molecule-interface coupling effects on electronic transport in molecular wires. *J. Chem. Phys.* **109**, 5036–5043 (1998).

47. Simmons, J. G. Generalized Formula for the Electric Tunnel Effect between Similar Electrodes Separated by a Thin Insulating Film. *J. Appl. Phys.* **34**, 1793–1803 (1963).

48. Lee, J. W., Sim, S. J., Cho, S. M. & Lee, J. Characterization of a self-assembled monolayer of thiol on a gold surface and the fabrication of a biosensor chip based on surface plasmon resonance for detecting anti-GAD antibody. *Biosens. Bioelectron.* **20**, 1422–1427 (2005).

49. Luo, L., Choi, S. H. & Frisbie, C. D. Probing hopping conduction in conjugated molecular wires connected to metal electrodes. *Chem. Mater.* **23**, 631–645 (2011).

50. Li, X.-Q., Zhang, H. & Yan, Y. A Superexchange-Mediated Sequential Hopping Theory for Charge Transfer in DNA. *J. Phys. Chem. A* **105**, 9563–9567 (2001).

51. Hines, T. *et al.* Transition from Tunneling to Hopping in Single Molecular Junctions by Measuring Length and Temperature Dependence. *J. Am. Chem. Soc.* **132**, 11658–11664 (2010).

52. Marcus, R. A. On the Theory of Electron-Transfer Reactions. VI. Unified Treatment for Homogeneous and Electrode Reactions. *J. Chem. Phys.* **43**, 679–701 (1965).

53. Kornyshev, A. A., Kuznetsov, A. M. & Ulstrup, J. *In situ superexchange electron transfer through a single molecule: A rectifying effect*. vol. 103 www.pnas.orgcgidoi10.1073pnas.0511188103 (2006).

54. Marcus, R. A. Exchange Reactions and Electron Transfer Reactions Including. *Energy* 21–31 (1960).

55. Mujica, V. & Ratner, M. A. Current-voltage characteristics of tunneling molecular junctions for off-resonance injection. *Chem. Phys.* **264**, 365–370 (2001).

56. Fujita, M. & Ogura, K. Supramolecular Self-Assembly of Macrocycles, Catenanes, and Cages through Coordination of Pyridine-Based Ligands to Transition Metals. *Bull. Chem. Soc. Jpn.* **69**, 1471–1482 (1996).

57. Pickaert, G. & Ziessel, R. Photoactive molecular-scale wires: Synthesis of carotene/terpyridine ditopic ligands. *Tetrahedron Lett.* **39**, 3497–3500 (1998).

58. Krebs, F. C. & Biancardo, M. Dye sensitized photovoltaic cells: Attaching conjugated polymers to zwitterionic ruthenium dyes. *Sol. Energy Mater. Sol. Cells* **90**, 142–165 (2006).

59. Hu, C. W., Sato, T., Zhang, J., Moriyama, S. & Higuchi, M. Multi-colour electrochromic properties of Fe/Ru-based bimetallo- supramolecular polymers. *J. Mater. Chem. C* **1**, 3408–3413 (2013).

60. Tuccitto, N. *et al.* Controlled density patterning of tolylterpyridine-tagged oligonucleotides. *Langmuir* **27**, 8595–8599 (2011).

61. Tuccitto, N., Giamblanco, N., Licciardello, A. & Marletta, G. Patterning of lactoferrin using functional SAMs of iron complexes. *Chem. Commun.* 2621–2623 (2007) doi:10.1039/b701527e.

62. Giamblanco, N. *et al.* Chelating Surfaces for Native State Proteins Patterning: The Human Serum Albumin Case. *ACS Appl. Mater. Interfaces* **7**, 23353–23363 (2015).

63. Zhong, Y. W., Vila, N., Henderson, J. C., Flores-Torres, S. & Abruña, H. D.

Dinuclear transition-metal terpyridine complexes with a dithienylcyclopentene bridge directed toward molecular electronic applications. *Inorg. Chem.* **46**, 10470–10472 (2007).

64. Barigelletti, F. & Flamigni, L. Photoactive molecular wires based on metal complexes. *Chem. Soc. Rev.* **29**, 1–12 (2000).

65. Visco, R. E. & Chandross, E. A. Electroluminescence in Solutions of Aromatic Hydrocarbons. *J. Am. Chem. Soc.* **86**, 5350–5351 (1964).

66. Forster, R. J., Bertoncello, P. & Keyes, T. E. Electrogenerated chemiluminescence. *Annu. Rev. Anal. Chem.* **2**, 359–385 (2009).

67. Tsuneyasu, S., Ichihara, K., Nakamura, K. & Kobayashi, N. Why were alternating-current-driven electrochemiluminescence properties from Ru(bpy)32+ dramatically improved by the addition of titanium dioxide nanoparticles? *Phys. Chem. Chem. Phys.* **18**, 16317–16324 (2016).

68. Pastore, P., Badocco, D. & Zanon, F. Influence of nature, concentration and pH of buffer acid-base system on rate determining step of the electrochemiluminescence of Ru(bpy)32+ with tertiary aliphatic amines. *Electrochim. Acta* **51**, 5394–5401 (2006).

69. Liu, Z., Qi, W. & Xu, G. Recent advances in electrochemiluminescence. *Chem. Soc. Rev.* **44**, 3117–3142 (2015).

70. Liu, D. *et al.* A novel electrochemiluminescent immunosensor based on CdS-coated ZnO nanorod arrays for HepG2 cell detection. *Nanoscale* **7**, 3627–3633 (2015).

71. Zhou, M., Robertson, G. P. & Roovers, J. Comparative study of ruthenium(II) tris(bipyridine) derivatives for electrochemiluminescence application. *Inorg. Chem.* **44**, 8317–8325 (2005).

72. Rallidis, L. S. *et al.* A. Juris; V. Balzani; F. Barigelletti; S. Campagna; P. Belser; A. von Zelewsky (1988). Ru(II) polypyridine complexes: photophysics, photochemistry, eletrochemistry, and chemiluminescence. , 84(none), 85–277. doi:10.1016/0010-8545(88)80032-8. *Eur. Heart J.* **19**, 395–401 (1998).

73. Halawa, M. I., Mostafa, I. M., Wu, G. & Li, B. S. Amplified anodic electrogenerated chemiluminescence of tris(2,2′-bipyridyl)ruthenium(II) for ultrasensitive detection of bambuterol: Application to content uniformity testing. *J. Electroanal. Chem.* **880**, 114881 (2021).

74. Pan, W., Liu, Y., Huang, Y. & Yao, S. Determination of difenidol hydrochloride by capillary electrophoresis with electrochemiluminescence

detection. *J. Chromatogr. B Anal. Technol. Biomed. Life Sci.* **831**, 17–23 (2006).

75. Liu, Y., Pan, W., Liu, Q. & Yao, S. Study on the enhancement of Ru(bpy)32+ electrochemilumiscence by nanogold and its application for pentoxyverine detection. *Electrophoresis* **26**, 4468–4477 (2005).

76. Richter, M. M., Bard, A. J., Kim, W. & Schmehl, R. H. Electrogenerated Chemiluminescence. 62. Enhanced ECL in Bimetallic Assemblies with Ligands That Bridge Isolated Chromophores. *Anal. Chem.* **70**, 310–318 (1998).

77. Staffilani, M. *et al.* Multimetallic Ruthenium(II) Complexes as Electrochemiluminescent Labels. *Inorg. Chem.* **42**, 7789–7798 (2003).

78. Wei, H. & Wang, E. Electrochemiluminescence of tris(2,2′-bipyridyl)ruthenium and its applications in bioanalysis: A review. *Luminescence* **26**, 77–85 (2011).

79. Algar, W. R., Tavares, A. J. & Krull, U. J. Beyond labels: A review of the application of quantum dots as integrated components of assays, bioprobes, and biosensors utilizing optical transduction. *Anal. Chim. Acta* **673**, 1–25 (2010).

80. Chen, A. *et al.* Signal-off Electrochemiluminescence Biosensor Based on Phi29 DNA Polymerase Mediated Strand Displacement Amplification for MicroRNA Detection. *Anal. Chem.* **87**, 6328–6334 (2015).

81. Zheng, H. *et al.* Fluoro-coumarin silicon phthalocyanine sensitized integrated electrochemiluminescence bioprobe constructed on TiO2 MOFs for the sensing of deoxynivalenol. *Sensors Actuators, B Chem.* **269**, 27–35 (2018).

82. Ma, Q. *et al.* DNA-mediated au-au dimer-based surface plasmon coupling electrochemiluminescence sensor for BRCA1 gene detection. *Anal. Chem.* **93**, 3308–3314 (2021).

83. Xia, H., Li, L., Yin, Z., Hou, X. & Zhu, J.-J. Biobar-Coded Gold Nanoparticles and DNAzyme-Based Dual Signal Amplification Strategy for Ultrasensitive Detection of Protein by Electrochemiluminescence. *ACS Appl. Mater. & Interfaces* **7**, 696–703 (2014).

84. Cheng, H. M. *et al.* Bulk morphology and diameter distribution of single-walled carbon nanotubes synthesized by catalytic decomposition of hydrocarbons. *Chem. Phys. Lett.* **289**, 602–610 (1998).

85. Liew, K. M., Wong, C. H., He, X. Q. & Tan, M. J. Thermal stability of

single and multi-walled carbon nanotubes. *Phys. Rev. B - Condens. Matter Mater. Phys.* **71**, 1–6 (2005).

86. Tuccitto, N. *et al.* Carbon Quantum Dots as Fluorescence Nanochemosensors for Selective Detection of Amino Acids. *ACS Appl. Nano Mater.* **4**, 6250–6256.

87. Zhang, Y. *et al.* Toxicity and efficacy of carbon nanotubes and graphene: The utility of carbon-based nanoparticles in nanomedicine. *Drug Metab. Rev.* **46**, 232–246 (2014).

88. Tuerhong, M., XU, Y. & YIN, X. B. Review on Carbon Dots and Their Applications. *Chinese J. Anal. Chem.* **45**, 139–150 (2017).

89. Venkatanarayanan, A. *et al.* High sensitivity carbon nanotube based electrochemiluminescence sensor array. *Biosens. Bioelectron.* **31**, 233–239 (2012).

90. Valenti, G. *et al.* Transparent Carbon Nanotube Network for Efficient Electrochemiluminescence Devices. *Chem. - A Eur. J.* **21**, 12640–12645 (2015).

91. Song, C. *et al.* Quench-Type Electrochemiluminescence Immunosensor Based on Resonance Energy Transfer from Carbon Nanotubes and Au-Nanoparticles-Enhanced g-C_3N_4 to CuO@Polydopamine for Procalcitonin Detection. *ACS Appl. Mater. Interfaces* **12**, 8006–8015 (2020).

92. Qin, Y. *et al.* Oxygen Containing Functional Groups Dominate the Electrochemiluminescence of Pristine Carbon Dots. *J. Phys. Chem. C* **121**, 27546–27554 (2017).

93. Kou, X., Jiang, S., Park, S. J. & Meng, L. Y. A review: recent advances in preparations and applications of heteroatom-doped carbon quantum dots. *Dalt. Trans.* **49**, 6915–6938 (2020).

94. Zhu, S. *et al.* The photoluminescence mechanism in carbon dots (graphene quantum dots, carbon nanodots, and polymer dots): current state and future perspective. *Nano Res.* **8**, 355–381 (2015).

95. Sun, J., Sun, H. & Liang, Z. Nanomaterials in Electrochemiluminescence Sensors. *ChemElectroChem* **4**, 1651–1662 (2017).

96. Tiwari, J. N., Tiwari, R. N. & Kim, K. S. Zero-dimensional, one-dimensional, two-dimensional and three-dimensional nanostructured materials for advanced electrochemical energy devices. *Prog. Mater. Sci.* **57**, 724–803 (2012).

97. Ruiz, A. M. *et al.* Cr-doped TiO_2 gas sensor for exhaust NO_2 monitoring. *Sensors Actuators, B Chem.* **93**, 509–518 (2003).

98. Okamoto, S. *et al.* Increase in Electrochemiluminescence Intensities by Use of Nanoporous TiO_2 Electrodes. *J. Electrochem. Soc.* **152**, A1677 (2005).

99. Tsuneyasu, S., Ichihara, K., Nakamura, K. & Kobayashi, N. Why were alternating-current-driven electrochemiluminescence properties from Ru(bpy)32+ dramatically improved by the addition of titanium dioxide nanoparticles? *Phys. Chem. Chem. Phys.* **18**, 16317–16324 (2016).

100. Chen, L. *et al.* Electrogenerated chemiluminescence of anatase TiO_2 nanotubes film. *Talanta* **85**, 56–62 (2011).

101. Wang, L. *et al.* Facet-dependent electrochemiluminescence spectrum of nanostructured ZnO. *Sci. China Chem.* **56**, 86–92 (2013).

102. Cazaux, J. Secondary electron emission and fundamentals of charging mechanisms in XPS. *J. Electron Spectros. Relat. Phenomena* **178**–**179**, 357–372 (2010).

103. Iatsunskyi, I. *et al.* Atomic layer deposition of palladium coated TiO_2/Si nanopillars: ToF-SIMS, AES and XPS characterization study. *Appl. Surf. Sci.* **542**, 148603 (2021).

104. Stefaniak, E. A., Buczynska, A., Novakovic, V., Kuduk, R. & Van Grieken, R. Determination of chemical composition of individual airborne particles by SEM/EDX and micro-Raman spectrometry. *J. Phys. Conf. Ser.* **162**, (2009).

105. Reis, M. A., Chaves, P. C. & Taborda, A. Review and perspectives on energy dispersive high resolution PIXE and RYIED. *Appl. Spectrosc. Rev.* **52**, 231–248 (2017).

106. Rogowski, J. & Kubiak, A. Effects of annealing temperature on the structure and electrical properties of tungsten contacts to n-type silicon carbide. *Mater. Sci. Eng. B Solid-State Mater. Adv. Technol.* **191**, 57–65 (2015).

107. Strazzulla, G. & Brunetto, R. Particle Accelerators as Tools to Investigate Astrochemistry. *Nucl. Phys. News* **27**, 23–27 (2017).

108. Yoon, S. & Lee, T. G. Biological tissue sample preparation for time-of-flight secondary ion mass spectrometry (ToF–SIMS) imaging. *Nano Converg.* **5**, (2018).

109. Clerc, J., Fourré, C. & Fragu, P. Sims microscopy: Methodology, problems

and perspectives in mapping drugs and nuclear medicine compounds. *Cell Biol. Int.* **21**, 619–633 (1997).

110. McPhail, D. S. Applications of Secondary Ion Mass Spectrometry (SIMS) in materials science. *J. Mater. Sci.* **41**, 873–903 (2006).

111. Oechsner, H. Sputtering-a review of some recent experimental and theoretical aspects. *Appl. Phys.* **8**, 185–198 (1975).

112. Falconer, I. J . J . Thomson ' s Work on Positive Rays , 1906-1914 Author (s): Isobel Falconer Source : Historical Studies in the Physical and Biological Sciences , Vol . 18 , No . 2 (1988), pp . 265- Published by : University of California Press Stable URL : http. **18**, 265–310 (2010).

113. Vickerman, J. C. "ToF-SIMS An Overview" ToF-SIMS: surface analysis by mass spectrometry 1-40. (2016).

114. Touboul, D. *et al.* MALDI-TOF and cluster-TOF-SIMS imaging of Fabry disease biomarkers. *Int. J. Mass Spectrom.* **260**, 158–165 (2007).

115. Kim, S. H., Lee, J., Jang, Y. J., Lee, K. B. & Lee, Y. ToF-SIMs and afm characterization of brown cosmetic contact lenses: From structural analysis to the identification of pigments. *J. Anal. Methods Chem.* **2020**, (2020).

116. Lockyer, N. P. & Vickerman, J. C. Progress in cellular analysis using ToF-SIMS. *Appl. Surf. Sci.* **231**–**232**, 377–384 (2004).

117. Malmberg, P. & Nygren, H. Methods for the analysis of the composition of bone tissue, with a focus on imaging mass spectrometry (TOF-SIMS). *Proteomics* **8**, 3755–3762 (2008).

118. Tuccitto, N. *et al.* Revealing Contamination and Sequence of Overlapping Fingerprints by Unsupervised Treatment of a Hyperspectral Secondary Ion Mass Spectrometry Dataset. *Anal. Chem.* **93**, 14099–14105 (2021).

119. Noël, C. *et al.* Depth Profiling of Organic Light-Emitting Diodes by ToF-SIMS Coupled with Wavelet-Principal Component Analysis. *ACS Appl. Polym. Mater.* **1**, 1821–1828 (2019).

120. Henderson, A., Fletcher, J. S. & Vickerman, J. C. A comparison of PCA and MAF for ToF-SIMS image interpretation. *Surf. Interface Anal.* **41**, 666–674 (2009).

121. Passarelli, M. K. *et al.* The 3D OrbiSIMS - Label-free metabolic imaging with subcellular lateral resolution and high mass-resolving power. *Nat. Methods* **14**, 1175–1183 (2017).

122. Kollmer, F., Paul, W., Krehl, M. & Niehuis, E. Ultra high spatial resolution

SIMS with cluster ions - Approaching the physical limits. *Surf. Interface Anal.* **45**, 312–314 (2013).

123. Vlasea, M. & Toyserkani, E. Experimental characterization and numerical modeling of a micro-syringe deposition system for dispensing sacrificial photopolymers on particulate ceramic substrates. *J. Mater. Process. Technol.* **213**, 1970–1977 (2013).

124. Tuccitto, N. *et al.* Highly conductive ~ 40-nm-long molecular wires assembled by stepwise incorporation of metal centres. *Nat. Mater.* **8**, 41–46 (2009).

125. Licciardello, A., Puglisi, O. & Pignataro, S. Effect of organic contaminants on the oxidation kinetics of silicon at room temperature. *Appl. Phys. Lett.* **48**, 41–43 (1986).

126. Wang, M., Römelt, C., Weyhermüller, T. & Wieghardt, K. Coordination Modes, Oxidation, and Protonation Levels of 2,6-Pyridinediimine and 2,2′:6′,2′-Terpyridine Ligands in New Complexes of Cobalt, Zirconium, and Ruthenium. An Experimental and Density Functional Theory Computational Study. *Inorg. Chem.* **58**, 121–132 (2019).

127. Hatzakis, M., Canavello, B. J. & Shaw, J. M. Single-Step Optical Lift-Off Process. *IBM J. Res. Dev.* **24**, 452–460 (1980).